THE ROLE OF GALAXY FORMATION IN THE STRUCTURE AND DYNAMICS OF DARK MATTER HALOS

Thesis submitted for the degree of

Doctor Philosophiae in Astrophysics

CANDIDATE:

Chiara Tonini

SUPERVISORS:

Prof. Paolo Salucci

Dr. Andrea Lapi

Prof. Carlos S. Frenk

Trieste, 24$^{\text{th}}$ October 2007

Table of Contents

Citations to Published Works

The original material this Thesis is made of has been published in the following papers:

Chapter 2:

> "Measuring the spin of spiral galaxies"
>
> **Tonini, C.**, Lapi, A., Shankar, F. & Salucci, P. 2006, ApJL, 638, L13

Chapter 3:

> "The universal rotation curve of spiral galaxies II. The dark matter distribution out to the virial radius"
>
> Salucci, P., Lapi, A., **Tonini, C.**, Gentile, G., Yegorova, I. & Klein, U. 2007, MNRAS, 378, 41

Chapter 4:

> "ΛCDM halo density profiles: where do actual halos converge to NFW ones?"
>
> Gentile G., **Tonini, C.** & Salucci P. 2007, A&A, 467, 925

Chapter 5:

> "Angular momentum transfer in dark matter halos: erasing the cusp"
>
> **Tonini, C.**, Lapi, A., Salucci, P. 2006, ApJ, 649, 591

Chapter 6:

> "Infalling of substructures and dark matter halo evolution"
>
> **Tonini, C.** & Frenk, C.S., in preparation

Appendix A:

> "Mass modelling from rotation curves"
>
> **Tonini, C.** & Salucci, P. 2004, in *Baryons in Dark Matter Halos*, ed. R. Dettmar et al. (http://pos.sissa.it), 89

Acknowledgments

This Thesis is the result of 4 unforgettable years, and I would like to thank all the people who shared them with me, making them light and joyful and exciting. We've come a long way together, and looking back, I'm happy with what I see... What a ride!

To my Advisor Paolo Salucci, you guided me with patience and trusted me and allowed me to follow my own way, even if it was unorthodox... You taught me the job, and it was fun!

To Andrea Lapi, thank you for being a friend and a great collaborator. I learned so much from you, working with you has been exciting... yeah, we got there before everybody else!

To Carlos Frenk, you gave me a fantastic chance and taught me a lot, in many ways.

Finally, to Frank vdB, you are the funniest and most improbable role model ever!

A special place in my heart is for the Tigers, Simona, Irina and Melita, your friendship made this time and place special for me, it felt like home. Simo, we've been together from the very beginning to the very end, I have no words to say how much you mean to me.

Irins, thank you for sharing this years with me... You know what I'm talking about!

Meliz, meeting you and talking to you was a joy and a relief...

To Tana delle Tigri, thanks... no place at Sissa will ever be like that again.

Ale! Fede! Where would I be without you? You've been with me always, with the sun and the rain, you've seen the best and the worst of me... Thank you for being around.

To Fabio, you saved my life. Thank you.

To Alberto and Sara, revolution was fun! Keep on rockin' guys, see you at another stage!

Carlo and Enrica, I miss you always, everytime we meet is special, I'm ready for the next crazy adventure...

Thanks to my brothers-in-Radio Fred and Luca, it's been awesome!! And thanks to all of Phasetransition, those were days of inspiration.

To my friends forever, my crepe-sister Fede, Puppi, Giada, Guido, Alex, Schiab, Skizzo, Michele, Marghi, Paolino, Lidia, Reni, Tom, Novel, Antonio, Paolone, Beppe & Mara, Dunja, Manu, Max, Beppe M., Laura, Luca Tornatore, the Durham guys, Kristen Juan Valeria and Nick, Mauro, Elena, Adriano (we share a big big love), I love you all, so much.

To Chris and Eddie, thank you for the sunshine.

A special mention to PJ, thank you for the soundtrack.

To all the friends I won't be seeing around so often any more... Even if we'll be apart, scattered across oceans and lands, in weird places full of very weird people, all because of that crazy day when we chose this funny kind of life... You're all in me, I know we'll always be together.

See you soon, another time, another place.

Chiara

To my Family

with Love

Abstract

Galaxy formation is a complex matter. It involves physics on hugely different scales, forms of matter still unknown, and processes poorly understood. The current theory of the formation of structures in the Universe predicts the assembly of dark matter halos through hierarchical clustering of small objects into larger and larger ones under the effect of gravity. In the potential wells of halos the baryons collapse to form galaxies, and the delicate balance between gravity, dissipative processes, star formation and feedback shapes the variety of systems we see today. At the galactic scales, some fundamental theoretical predictions fails to show up in the observations, regarding the structure and dynamics of the dark matter halo.

My Thesis addresses this problem by taking an evolutionary approach. I analysed in detail the many and different observational evidences of a discrepancy between the predicted halo equilibrium state and the one inferred from the measurable observables of disk galaxies, as well as of the scaling relations existing between the angular momentum, geometry and mass distribution of the luminous and dark components, and realised that they all seem to point towards the same conclusion: the baryons hosted inside the halo, by collapsing and assembling to form the galaxy, perturbed the halo equilibrium structure and made it evolve into new configurations.

From the theoretical point of view, the behaviour of dark matter halos as collisionless systems of particles makes their equilibrium structure and mass distribution extremely sensitive to perturbations of their inner dynamics. The galaxy formation occurring inside the halos is a tremendous event, and the dynamical coupling between the baryons and the dark matter during the protogalaxy collapse represents a perturbation of the halo dynam-

ical structure large enough to trigger a halo evolution, according to the relative mass and angular momentum of the two components.

My conclusion is that the structure and dynamics of dark matter halos, as well as the origin of the connection between the halo and galaxy properties, are to be understood in in terms of a joint evolution of the baryonic and dark components, originating at the epoch of the collapse and formation of the galaxy.

Chapter 1

Introduction: hierarchical clustering in a CDM Universe

In this Chapter I introduce the theory of structure formation, outlying the background physics and providing a general framework for the original material of this Thesis. I start with a brief description of the current cosmological model and the growth of perturbations in the primordial Universe, to define the paradigm of hierarchical clustering, in its latest formulation. I then analyze the equilibrium structure of dark matter halos as collisionless systems of particles, describing their phase-space properties and the physical mechanisms that shape them. In particular, I focus on the hierarchical clustering prediction of a self-similar halo, with a characteristic phase-space structure, and describe in detail its properties and the unsolved problems it presents, both from the theoretical point of view and when compared to observations. I finally introduce the topic of the scaling relations between the dark matter and the baryonic component hosted by the halos, that represents the starting point for the models of galaxy formation and the prelude for this Thesis.

I warn the reader that the material contained in this Chapter gives a very general outline of the theoretical framework without entering in too much detail, and refer her/him to the provided references for an exhaustive portrait of the topic.

1.1 The smooth Universe

The standard cosmological model relies on the basic observational evidence that the Universe at large scales is homogeneous and isotropic [121], as stated by the *cosmological principle*, and confirmed by data from the Cosmic Microwave Background, and the distributions and correlation functions of galaxies and clusters (2dFGRS, [34]), while on smaller and smaller scales it features an increasing complexity. To understand the present-day pattern of structures we need to consider the evolution of the Universe as a whole, as a smooth expanding background, and the gravitational growth of primordial inhomogeneities in its matter components, that decouple from it and develop characteristic properties.

The Universe is not in a stationary state, it evolves with an *expansion factor* $a(t)$ that completely characterizes its dynamics. The only global evolution compatible with homogeneity and isotropy is of the kind $\dot{\mathbf{r}} = \mathbf{v}(t) = H(t)\ \mathbf{r}$, where $\mathbf{v}$ is the time-variation of the *proper distance* between two points in space, defined as $\mathbf{r} = a(t)\ \mathbf{x}$, where $\mathbf{x}$ is the so-called *comoving distance* between the two objects and is constant. The rate of expansion $H(t) = \dot{a}(t)/a(t)$ is called the *Hubble parameter*, and $v(t) = H(t)\ \mathbf{r}(t)$ is referred to as the *Hubble law*.

The dynamics of the evolving Universe is governed by the Friedmann's equations; the first one is a a continuity equation for the density and pressure of any matter-energy component present in the Universe:

$$\frac{d(\rho_i a^3)}{da} = -3a^2 p_i\ . \tag{1.1}$$

The second equation describes the link between the energy densities and the geometry of space-time:

$$\left(\frac{\dot{a}}{a}\right)^2 = \frac{8\pi G}{3}\sum_i \rho_i - \frac{k}{a^2} \tag{1.2}$$

After the equation of state $w_i = p_i/\rho_i$ has been specified for a given species, the first equation yields the evolution of the corresponding energy density:

$$\rho_i(a) = \rho_i(a_0)\ \left(\frac{a_0}{a}\right)^3\ exp\left[-3\int_{a_0}^{a}\frac{dx}{x}w_i(x)\right]\ . \tag{1.3}$$

Once the ρ_i are known, the second Friedmann's equation (1.2) determines the expansion

factor:

$$\left(\frac{\dot{a}}{a}\right)^2 = H_0^2 \sum_i \Omega_i \left(\frac{a_0}{a}\right)^{3(1+w_i)} - \frac{k}{a^2} \ , \tag{1.4}$$

where $H_0 = 100h\ km\ s^{-1}\ Mpc^{-1}$ is the Hubble parameter today, and $\Omega_i \equiv \rho_i(a_0)/\rho_c$ is the energy density in terms of the *critical density* $\rho_c \equiv 3H_0^2/8\pi G$ that yields a flat ($k = 0$) Universe: this corresponds to $\Omega \equiv \sum_i \Omega_i = 1$. As it turns out (see the most recent data from WMAP-3, [163]), our Universe yields a value of Ω compatible with flatness ($\Omega \simeq 1.02 \pm 0.02$). By evalutating Eq. (1.4) at the present epoch one obtains $k/a_0^2 = H_0^2(\Omega - 1)$, which allows to set the conventional values $a_0 = 1$ and $\dot{a}_0 = H_0$.

The evolution of the Universe is thus determined by its species' content at any given time; the simplest solutions to the Friedmann's equations are obtained whenever an energy density component dominates over the others, as often happens at different epochs; so, in general, $a(t) \propto t^{2/[3(1+w)]}$ for $w > -1$, and $a(t) \propto e^{\alpha t}$ with $\alpha = const$ for $w = -1$. Moreover, in the current models, the components present in the Universe are each characterized by a constant w_i, so that $\rho_i(a) \propto a^{-3(1+w_i)} \propto (1+z)^{3(1+w_i)}$.

The energy density of the Universe is dominated today by an exotic component called **dark energy**, discovered by observing the recession velocity of high-redshift Ia supernovae; it accounts for $\Omega_{DE} \sim 0.73$, with a negative equation of state, that causes accelerated expansion at present epochs for any value $w < -1/3$. The nature of this component is unknown; according to the equation of state, each model makes different predictions on the future evolution of the Universe; current models include a *cosmological constant* Λ with $w = -1$, a *phantom energy* with $w < -1$, or a more general *quintessence* with $-1 < w < -1/3$.

The remaining components of the energy density are dominated by matter in non-relativistic form, of an unknown nature, that we call **dark matter**; its presence was hypotized already in the '30s by Zwicky ([208],[209]), and has been confirmed ever since from observations of the dynamics of galaxies and clusters, and of gravitational lensing. In the current scenario of structure formation, it is thought to consist of particles which interact only through gravity; candidates that satisfy the requirement and are compatible with the standard cosmology are neutrinos, axions, the lightest supersymmetric particle,

"jupiters" and black holes of mass $< 100 M_{\odot}$. These fall under the common definition of **cold** dark matter; at early times these particles are non-relativistic, with mean velocities that are small relative to the mean expansion of the Universe (this requirement excludes light neutrinos with masses $< 30eV$ [199]. For both the dark matter ($\Omega_{DM} \simeq 0.23$) and the baryons ($\Omega_B \simeq 0.04$), the equation of state is $w = 0$, and the density is diluted like $\rho \propto a^{-3} \propto (1+z)^3$.

The ultra-relativistic matter, mainly in the form of **neutrinos** ($\Omega_\nu < 0.015$), and the **radiation** ($\Omega_R \simeq 5\ 10^{-5}$) are characterized by $w = 1/3$, with a dilution of $\rho \propto a^{-4} \propto (1+z)^4$. As a consequence, in an expanding Universe the energy density of radiation decreases more quickly than the volume expansion.

The relevant component in the present discussion is the dark matter (DM); in the standard cosmogony, the cosmic structures we see today had their origin in the early Universe from quantum-generated DM energy density perturbations, grown by gravitational instability ([121],[122]). In the next Section, I will briefly review the theory of the linear growth of the primordal perturbations in the case of non-relativistic dark matter, and the subsequent non-linear evolution leading to hierarchical clustering. [1]

1.1.1 Ripples in the pond

While the Universe as a whole can be described as homogeneous and isotropic at large scales, on smaller scales it becomes progressively more inhomogeneous and clumpy. If the primordial Universe had indeed been totally uniform, it would have never developed any of the structures seen today; on the contrary, even the slightest inhomogeneity would have been dramatically amplified by gravitational instability. Consider Eq. (1.2), after defining $\rho = (\rho_0 a_0^3)/a^3$ and differentiating with respect to t:

$$\ddot{a} = -\frac{4\pi G \rho_0}{3a^2} = -\left(\frac{2}{9t_0^2}\right)\frac{1}{a^2} \tag{1.5}$$

If we perturb $a(t)$ slightly and have $a(t) + \delta a(t)$, such that the corresponding fractional density perturbation relative to the smooth background $\bar{\rho}$ is $\delta \equiv (\rho - \bar{\rho})/\bar{\rho} = -3(\delta a/a)$, we

[1] A complete description of these processes has to be done in the General Relativity formalism, even for non-relativistic matter, to account for the initial stages when perturbations are super-horizon. However, for the purpose of introducing the formation of dark matter halos, it is sufficient to follow the evolution of the DM perturbations after they enter the horizon, when the Newtonian approximation can be safely used.

find that δa satisfies the equation

$$\frac{d^2}{dt^2}\delta a = \left(\frac{4}{9t_0^2}\right)\frac{\delta a}{a^3} = \frac{4}{9}\frac{\delta a}{t^2} \ . \tag{1.6}$$

The growing solution to this equation is $\delta a \propto t^{4/3} \propto a^2$. Hence the density perturbation, parameterized by its *density contrast* δ, grows as $\delta \propto a$.

1.2 The hierarchical clustering

The current paradigm for structure formation finds its roots in the pioneering work by Peebles ([123],[125],[126],[127],[129]), who established the **hierarchical clustering** or **isothermal** theory. In this scenario, structure builds up through the aggregation of nonlinear objects into larger and larger units. The original formulation of the model predates the Cold Dark Matter (CDM) version; it describes the clustering of baryonic structures, but encounters a number of difficulties and is soon abandoned. In the CDM model ([130],[13],[44],[5]) the build-up of structures is governed by the dark dissipationless component, that evolves under gravity from an initially gaussian distribution of primordial perturbations; small fluctuations first, and then larger and larger ones, become nonlinear and collapse when self-gravity dominates their dynamics, to form virialised, gravitationally bound systems. As larger perturbations collapse, the smaller objects embedded in them cluster to form more complex patterns. In the meanwhile, the dark matter provides the potential wells within which the gas cools and forms galaxies under dissipative collapse [121].

The success of the CDM model stems from a variety of sources. First of all, most of the mass in the Universe does appear to be in the DM form; second, if this matter has interacted only through gravity since early times, it is possible to reconcile the very small observed amplitude of fluctuations in the Cosmic Microwave Background with the massive nonlinear structures in the present Universe. Moreover, the large-scale distribution of galaxies is consistent with the patterns resulting from gravitational amplification of gaussian density fluctuations. This is a simple and natural condition in CDM models, where the galaxies are indeed expected to trace the DM distribution on large scales [200].

In a radiation-dominated Universe, there are two independent perturbation modes of the coupled radiation-gas mixture for which the density contrast is non-decreasing in

time. The isothermal mode describes fluctuations in the photon-to-baryon rate, while the radiation temperature is almost uniform. The other mode, called adiabatic, describes fluctuations in the radiation temperature, with a constant photon-to-baryon rate (and was championed by Zel'dovich and collaborators [199]).

If the models are refined to accomodate dark matter, the two modes lead to very different scenarios. The adiabatic mode is the one that grows faster, and it leads to the formation of bigger structures compared to the isothermal; in this scenario, cluster-size objects form first, and galaxies are originated from fragmentation of such structures. This is inconsistent with the observational evidence that galaxies are older than larger-scale objects [198]. Moreover, the natural dark matter candidate for such a scenario is hot, in the form of neutrinos. Numerical simulations showed that this kind of dark matter is unable to reproduce the observed distribution of galaxies and clusters [199]. In the isothermal scenario objects of galactic scale form by aggregation and merging, while large-scale structures are essentially random and have little influence on galaxy properties.

The CDM model, although taking its first steps from the isothermal picture, features a power spectrum of the fluctuations significantly redder than white noise (the power density at galactic scales is well below that on cluster scales); as a result, collapse on galactic scales occurs more recently in the CDM than in the old isothermal picture. Compared with the old scenario, the CDM cosmogony is much less clearly hierarchical, with the interesting consequence that the galaxy formation inside a dark matter halo is not really an independent event with respect to the formation of the halo itself, and of bigger and smaller structures. Protogalactic collapse is neither the falling together of a single smooth perturbation nor the merging of a set of well equilibrated precursor objects, but lies somewhere between the two. In addition, while in general galaxies form before the larger structures in which they are embedded (like clusters), the temporal separation of the two processes is not enough for them to be independent. As a result, **biases** arise in the galaxy population, meaning that the properties of galaxies strongly depend on the large-scale environment surrounding them [199].

The most convenient way to describe the growth of structures is to use the Fourier transform $\delta_{\mathbf{k}}(t)$ of the density contrast, treated as a realisation of a random process. The

power spectrum of the fluctuations at a given wavenumber k is $P(k,t) \equiv \langle|\delta_{\mathbf{k}}(t)|^2\rangle$, defined as a statistical quantity averaged over an ensemble of possibilities; the isotropy of the Universe implies that the power spectrum depends only on the magnitude $|\mathbf{k}|$ of the wavenumber [121].

At early times, the DM density fluctuation field is represented as a superposition of plane waves $\delta(x) = \int \delta_k e^{i(\vec{k}\cdot\vec{x})} d^3k$; the Fourier modes are independent, with phases randomly distributed on $(0, 2\pi]$. The distribution of $\delta(x)$ at any arbitrary set of positions $(x_1, x_2, ...)$ is a multivariate gaussian. Such fields are known as *gaussian random fields* and are predicted by a wide class of theories for the origin of structure in the Universe [199]. In this picture, $P(k,t)$ gives the complete statistical description of the initial conditions and the subsequent evolution of the density field, down to nonlinearity.

The power per logarithmic band in k is given by

$$\Delta_k^2(t) = \frac{k^3|\delta_k(t)|^2}{2\pi^2} = \frac{k^3 P(k,t)}{2\pi^2} \ . \tag{1.7}$$

Observations show the power spectrum to be fairly smooth [121], and hence it can be approximated by a power law in k locally at any given time. Of interest for the ΛCDM model, the CMB data at very large scales are well fitted with a simple power-law like

$$P(k) = P(K_0)\left(\frac{k}{k_0}\right)^{n_s-1} \tag{1.8}$$

with spectral index $n_s \approx 0.95$, indicating an almost scale-free power spectrum. However, inflationary models favour a running spectral index, $n_s = n_s(k) = d\ln P/d\ln k$, so that

$$P(k) = P(K_0)\left(\frac{k}{k_0}\right)^{n_s(k_0)+ln(k/k_0)dn_s/dln(k)} \ ; \tag{1.9}$$

the debate is still open about the best-fit to the newest data ([162],[163]). Notice that the requirement of hierarchical clustering, that small objects form first, is ensured if $P(k,t)$ is a decreasing function of mass, or correspondingly, an increasing function of the spatial wavenumber k.

The amplitude of the fluctuations at a given scale M is related to the mean square fluctuation σ, defined as

$$\sigma_M^2 = \left(\frac{\delta M}{M}\right)^2 = \frac{1}{2\pi^2}\int_0^{k_{max}=1/R} k^2 P(k) dk \ , \tag{1.10}$$

where the mass scale M is associated to the linear scale R by $M = (4\pi/3)\bar{\rho}(t_0)R^3$. Notice that

$$\sigma_M^2 = \left(\frac{\delta M}{M}\right)^2 = \frac{1}{2\pi^2}\int_0^{k_{max}=1/R} k^3 P(k) d\ln k = \int_0^{k_{max}} \Delta_k^2 d\ln k \ , \tag{1.11}$$

so that the power at scale k, $\Delta_k^2(t)$, can be viewed as the contribution to the mean square fluctuation in the logarithmic band k, or at the scale $R \approx k^{-1}$:

$$\Delta_k^2(t) = \left(\frac{\delta\rho}{\rho}\right)^2_{R\simeq k^{-1}} = \left(\frac{\delta M}{M}\right)^2_{R\simeq k^{-1}} \cong \sigma^2(R,t) \ . \tag{1.12}$$

Given the power spectrum defined above, the mean square fluctuation is related to the linear scale R by

$$\sigma_R^2 \propto k^{3+n_s-1} \propto R^{-(3+n_s-1)} \ . \tag{1.13}$$

The normalization of the power spectrum is usually obtained through the value of $\sigma_8 \equiv \sigma(8\ Mpc\ h^{-1})$; in this work, I take $\sigma_8 = 0.8$, an average value between the first- and third-year WMAP data ([162],[163]).

At any given time, the power spectrum $P(k,t)$ completely characterizes the pattern of density fluctuations. The gravitational potential generated by a perturbation δ in a region of size R is $\phi \propto \delta M/R \propto \bar{\rho}\delta R^2$. In an expanding Universe $\bar{\rho} \propto a^{-3}$ and $R \propto a$, while the perturbation grows as $\delta \propto a$, making ϕ constant in time. This implies that the perturbations that were present in the Universe at the time when radiation decoupled from matter would have left their imprint on the radiation field. Photons climbing out of a potential well lose energy and are redshifted by an amount $\Delta\nu/\nu \approx \phi/c^2$, hence we expect to see a temperature fluctuation in the microwave radiation corresponding to $\Delta T/T \approx \Delta\nu/\nu \approx \phi/c^2$. The largest potential wells would have left their imprint on the CMB at the time of decoupling; galaxy clusters constitute the deepest wells in the Universe, with escape velocities of the order $v_{esc} \approx \sqrt{GM/R} \approx 10^3 km/s$, that leads to $\Delta T/T \approx (v_{esc}/c)^2 \approx 10^{-5}$. The proof that the theory was sound was indeed found in the microwave background radiation, when such temperature fluctuations were observed (COBE [102], [121]).

When the self-gravity of the growing perturbation dominates over the expansion, the density contrast reaches some critical value $\delta(R,t) \to \delta_c \approx 1$ and the evolution goes nonlinear; matter collapses to form a bound structure on the scale $R = R_{nl}$, that at any

time t obeys the relation

$$R_{nl}(t) \propto a(t)^{2/(n+3)} = R_{nl}(t_0)(1+z)^{-2/(n+3)} \ ; \tag{1.14}$$

in other words, structure of mass $M \propto R_{nl}^3$ form at a redshift z where

$$M_{nl}(z) = M_{nl}(t_0)(1+z)^{-6/(n+3)} \ . \tag{1.15}$$

Once formed and virialised, such gravitationally bound structures remain frozen at a mean density defined as

$$\rho_{halo} \simeq \Omega \rho_c \Delta_{vir} (1+z)^3 \ , \tag{1.16}$$

where Δ_{vir} is the density contrast at the redshift z of formation, and $\rho_{back}(z) = \rho_c \Omega (1+z)^3$ is the background density of the Universe at z, in terms of the critical density $\rho_c = 2.8 \times 10^{11}\, h^2\, M_\odot\, \mathrm{Mpc}^{-3}$. Given a halo of mass M_{vir}, the virial radius is determined as

$$R_{vir} = [3\, M_{vir}\, \Omega_M^z / 4\pi\, \rho_c\, \Omega_M\, (1+z)^3\, \Delta_{vir}]^{1/3} \ ; \tag{1.17}$$

at any given redshift z, the density parameter is $\Omega_M^z = \Omega_M\, (1+z)^3 / [(1-\Omega_M) + \Omega_M\, (1+z)^3]$ in terms of today's value Ω_M, and the density contrast is $\Delta_{vir} = 18\,\pi^2 + 82\,(\Omega_M^z - 1) - 39\,(\Omega_M^z - 1)^2$. The cosmological parameters adopted throughout this work are consistent with WMAP-3 [163]; in particular, I consider a flat ($k = 0$) Universe with Hubble parameter $h = H_0/100$ km s^{-1} Mpc^{-1} $= 0.71$, matter density $\Omega_M \approx 0.27$ and $\Delta_{vir} \approx 100$ at $z = 0$.

After defining the circular velocity associated with the mass M_{vir} as

$$v_c^2 \equiv \frac{G M_{vir}}{r} \equiv \frac{4\pi G}{3} \rho_{halo} r^2 \ , \tag{1.18}$$

the redshift of formation of the halo can be written as

$$(1+z) \simeq 5.8 \left(\frac{200}{\Omega \Delta_{vir}} \right)^{1/3} \frac{(v_c/200\ km/s)^{2/3}}{(r/h^{-1}\ Mpc)^{2/3}} \ . \tag{1.19}$$

Notice the manifestation of the hierarchical clustering; smaller scales are the first to go nonlinear and virialise, forming objects of higher mean density; while larger perturbations grow and collapse, the small fluctuations on top of them cluster and merge, building up the hierarchy.

1.3 The equilibrium structure of dark matter halos

The virialised dark matter objects originated from the gravitational growth of perturbations and the subsequent evolution through hierarchical clustering are called **halos**. In the state-of-the-art version of the theory, they are collisionless systems of particles; the particles move under the influence of the *mean* potential generated by the whole mass distribution, while the two-body encounters are negligible.

A system made of a large number of particles moving under the influence of a smooth potential is fully described in phase-space, at any time t, by specifying the number of particles $f(\mathbf{x}, \mathbf{v}, t) d^3\mathbf{x} d^3\mathbf{v}$ having positions in the volume $d^3\mathbf{x}$ centered on $\mathbf{x}$ and velocities in the volume $d^3\mathbf{v}$ centered on $\mathbf{v}$. The quantity $f(\mathbf{x}, \mathbf{v}, t)$ is a probability density, called **phase-space distribution function** (DF) and is always $f \geq 0$ for physical systems [10]. Given the particles' initial coordinates and velocities, their phase-space trajectories are determined by Newton's law; in other words, if $f(\mathbf{x}, \mathbf{v}, t_0)$ is known at some time t_0, the information it contains is sufficient to evaluate $f(\mathbf{x}, \mathbf{v}, t)$ at any later time t. The DF thus fully specifies the evolution of the system.

Consider a system of particles moving along their orbits under a gravitational potential Φ, giving rise to a flow of points in phase space; if we write the phase-space coordinates as

$$(\mathbf{x}, \mathbf{v}) \equiv \mathbf{w} \equiv (w_1, ..., w_6) \ , \tag{1.20}$$

then the velocity of the flow is

$$\dot{\mathbf{w}} = (\dot{\mathbf{x}}, \dot{\mathbf{v}}) = (\mathbf{v}, -\nabla\Phi) \ . \tag{1.21}$$

The 6-dimensional vector $\dot{\mathbf{w}}$ is a generalised velocity that bears the same relationship to $\mathbf{w}$ as the 3-dimensional velocity $\mathbf{u} = \dot{\mathbf{x}}$ does to $\mathbf{x}$.

The flow described by Eq. (1.21) conserves the particles; in the absence of collisions, particles do not jump from one point of phase-space to another, but follow smooth trajectories. Hence, $f(\mathbf{w}, t)$ satisfies a continuity equation, like the matter density of an

ordinary fluid [10]:

$$\frac{\partial f}{\partial t} + \sum_{\alpha=1}^{6} \frac{\partial (f \dot{w}_\alpha)}{\partial w_\alpha} = 0 \ . \tag{1.22}$$

If integrated over volume, this equation shows that there is a balance between the rate at which particles enter and exit a given phase-space volume.

It is easy to see that the flow described by $\dot{\mathbf{w}}$ has the special property that

$$\sum_{\alpha=1}^{6} \frac{\partial \dot{w}_\alpha}{\partial w_\alpha} = \sum_{i=1}^{3} \left(\frac{\partial v_i}{\partial x_i} + \frac{\partial \dot{v}_i}{\partial v} \right) = \sum_{i=1}^{3} -\frac{\partial}{\partial v_i} \left(\frac{\partial \Phi}{\partial x_i} \right) = 0 \ ; \tag{1.23}$$

notice that $(\partial v_i / \partial x_i) = 0$ between independent coordinates in phase space, and the last equality comes from the fact that $\nabla \Phi$ does not depend on the velocities. Combining (1.22) and (1.23) leads to the **collisionless Boltzmann equation**:

$$\frac{\partial f}{\partial t} + \sum_{\alpha=1}^{6} \dot{w}_\alpha \frac{\partial f}{\partial w_\alpha} = \frac{\partial f}{\partial t} + \sum_{i=1}^{3} \left(v_i \frac{\partial f}{\partial x_i} - \frac{\partial \Phi}{\partial x_i} \frac{\partial f}{\partial v_i} \right) = 0 \ , \tag{1.24}$$

equivalently written as

$$\frac{\partial f}{\partial t} + \mathbf{v} \cdot \nabla f - \nabla \Phi \cdot \frac{\partial f}{\partial \mathbf{v}} = 0 \ , \tag{1.25}$$

or simply

$$\frac{\mathrm{d} f}{\mathrm{d} t} = 0 \ . \tag{1.26}$$

This is the fundamental equation governing the dynamics of a collisionless system, and states that the flow of points in phase space is incompressible; the DF around the phase point of any given particle moving through phase space is constant. This does not hold if encounters are not negligible [10].

The DF is conserved in the motion through phase-space, therefore it represents a steady-state solution of the Boltzmann equation. This allows to introduce the concept of **integral of motion** in the potential $\Phi(\mathbf{x})$. By definition, a function of the phase-space coordinates $\mathbf{I}(\mathbf{x}, \mathbf{v})$ is an integral if and only if

$$\frac{d}{dt} I([\mathbf{x}(t), \mathbf{v}(t)] = 0 \tag{1.27}$$

along all orbits. With the equations of motion this becomes

$$\frac{dI}{dt} = \nabla I \cdot \frac{d\mathbf{x}}{dt} + \frac{\partial I}{\partial \mathbf{v}} \cdot \frac{d\mathbf{v}}{dt} = 0 \ , \quad \text{or} \quad \mathbf{v} \cdot \nabla I - \nabla \Phi \cdot \frac{\partial I}{\partial \mathbf{v}} = 0 \ . \tag{1.28}$$

But this is exactly Equation (1.25), and this leads to the formulation of the **Jeans theorem**: *any steady-state solution of the collisionless Boltzmann equation depends on the phase-space coordinates only through integrals of motion in the potential Φ, and any function of the integrals yields a steady state solution of the collisionless Boltzmann equation.* A proof of the theorem can be found in [10]. For systems of interest in the present work, the potential is regular (see the same reference); in this case, the **Strong Jeans theorem** holds: *the DF of a steady-state system in which almost all orbits are regular with incommensurable frequencies may be presumed to be a function only of three independent isolating integrals.*

The Jeans theorem assures that the DF of a system can always be expressed in terms of the integrals of motions; as will be clear in Chapter 5, this is particularly useful because, by this property, the DF determines the symmetry of the system. Consider a steady-state spherical system; a simple extension of the strong Jeans theorem [100] states that the integrals of motion that describe it are the energy E, the modulus of the total angular momentum L^2 and its z-component L_z [10]. If the system is nonrotating, the DF will be a constant in L_z, so that the explicit dependence on L_z will disappear; if the system is also symmetric in the components of the velocity dispersion, the explicit dependence on L^2 will also disappear. In this sense, the DF gives information about the symmetries governing the system's evolution. Any perturbation acting from outside, that causes a symmetry breaking in the velocity dispersion tensor, alters the system's evolution and transforms the DF describing its equilibrium.

The quantity f is unfortunately not accessible to direct measurement in real systems. In fact, one can count the particles in any given volume $d^3\mathbf{x}\, d^3\mathbf{v}$, but as the latter shrinks and contains only a few particles, the result will radically depend on the particular volume chosen, with wild fluctuations that invalidate the reliability of the result. Only by treating f as a probability density, it correctly describes the properties of the system; in analogy with the wave function in a quantum dynamics system, it is not measurable in itself, but the physical information is contained in the expectation values of some phase-space functions $Q(\mathbf{x}, \mathbf{v})$ obtained through f. As an example, given a dark matter halo

characterised by some $f(r,v)$, the spatial density profile (in real space) is given by:

$$\rho(r) = \int_0^\infty f(r,v) d^3v \ , \tag{1.29}$$

and the mean velocity of the particles in the given volume is:

$$\overline{v}_i \equiv \frac{1}{\rho} \int f v_i d^3v \ ; \tag{1.30}$$

in general, all the macroscopic observables of the system will be average quantities over the DF:

$$\langle O \rangle = \frac{\int O \ f(r,v) d^3v}{\int f(r,v) d^3v} \ . \tag{1.31}$$

If one wants to estimate the DF in some point (**x**,**v**), the best approximation to the actual one is the average of f over a small volume centered on the point. This quantity is called the **coarse-grained** distribution function $\bar{f}$, and is complicated and tricky to use, because it does not satisfy the Boltzmann equation. However, it can be measured in numerical simulations, and as I will explain later on, it can be related to the entropy of the system.

In general, the Boltzmann equation itself is of little practical use since, given the high number of variables of f, the complete solution is difficult to obtain. However, valuable information on the system is contained in the equation's moments. By integrating Eq. (1.24) over the velocity, one obtains a continuity equation,

$$\frac{\partial \rho}{\partial t} + \frac{\partial (\rho \overline{v}_i)}{\partial x_i} = 0 \ , \tag{1.32}$$

after considering that x_i, v_i, t are independent variables, that $f(x,v) = 0$ for sufficiently large velocities, and after applying the divergence theorem. By multiplying Eq. (1.24) by v_j and integrating over velocity again, one obtains

$$\frac{\partial (\rho \overline{v}_j)}{\partial t} + \frac{\partial (\rho \overline{v_i v_j})}{\partial x_i} + \rho \frac{\partial \Phi}{\partial x_j} = 0 \ , \tag{1.33}$$

where

$$\overline{v_i v_j} \equiv \frac{1}{\rho} \int v_i v_j f d^3v \ . \tag{1.34}$$

The mean value of $v_i v_j$ can be decomposed in a contribution from the streaming motions $\overline{v}_i \overline{v}_j$ and one from the velocity dispersion:

$$\sigma_{ij}^2 \equiv \overline{(v_i - \overline{v}_i)(v_j - \overline{v}_j)} = \overline{v_i v_j} - \overline{v}_i \overline{v}_j \ ; \tag{1.35}$$

by subtracting v_j times Eq. (1.32) from Eq. (1.33), and making use of Eq. (1.35), we obtain the analog of Euler's equation of the flow of a fluid, for our system of collisionless particles:

$$\rho\frac{\partial\overline{v}_j}{\partial t}+\rho\overline{v}_i\frac{\partial\overline{v}_j}{\partial x_i}=-\rho\frac{\partial\Phi}{\partial x_j}-\frac{\partial(\rho\sigma_{ij}^2)}{\partial x_i}\ . \tag{1.36}$$

The last term of the r.h.s. acts like a pressure force $-\nabla p$, where $-\rho\sigma_{ij}^2$ is a stress tensor that describes a generic anisotropic pressure. The set of equations (1.32, 1.33, 1.36) are known as the **Jeans equations**. The valuability of these equations (and in particular of Eq. 1.36) is in their relating observationally accessible quantities that satisfy the Boltzmann equation, like the system's streaming velocity, velocity dispersion, density profile, without actually solving the Boltzmann equation itself. As an example, given a system with known density profile, the Jeans' equations yield the velocity dispersion profile compatible with equilibrium. Notice that this process in general allows for more than one solution, since we lack the analogous of the equation of state of a fluid, that would link the components of the tensor σ^2 to the density; in practice, we overcome the difficulty by making some assumption about the symmetry of σ^2, which is a valid semplification if the assumption itself is physically sound [10].

A particularly useful application of the Jeans's equations in the present work is the study of spherically symmetric systems in steady states; after defining the spherical coordinates $(\mathbf{x},\mathbf{v})\equiv(r,\theta,\phi,v_r,v_\theta,v_\phi)$, we have that $\overline{v}_r=\overline{v}_\theta=\overline{v}_\phi=0$; in this case, $\overline{v_i^2}=\sigma_i^2$, and

$$\frac{d(\rho\sigma_r^2)}{dr}+\frac{\rho}{r}\left[2\sigma_r^2-\left(\sigma_\theta^2+\sigma_\phi^2\right)\right]=-\rho\frac{d\Phi}{dr}\ . \tag{1.37}$$

Consider a dark matter halo, such that both the density and the velocity structure are invariant under rotations about the center of mass; hence, the halo itself does not rotate, and

$$\sigma_\theta^2=\sigma_\phi^2\ . \tag{1.38}$$

It follows that the velocity ellipsoids are spheroids with their symmetry axes pointing to the center of the system. The **anisotropy parameter** is defined as

$$\beta\equiv 1-\frac{\sigma_\theta^2}{\sigma_r^2} \tag{1.39}$$

and describes the degree of anisotropy of the velocity distribution at each point. With these assumtpions, Eq. (1.37) becomes

$$\frac{1}{\rho}\frac{d(\rho\sigma_r^2)}{dr} + 2\frac{\beta\sigma_r^2}{r} = -\frac{d\Phi}{dr} \ . \tag{1.40}$$

If we can measure the quantities ρ, β and σ_r^2 as functions of radius, then Eq. (1.40) allows to determine the mass profile and the circular velocity of the system, through

$$v_c^2 = \frac{GM(r)}{r} = -\sigma_r^2 \left(\frac{d\ ln\rho}{d\ ln\ r} + \frac{d\ ln\sigma_r^2}{d\ ln\ r} + 2\beta \right) \ . \tag{1.41}$$

1.3.1 The NFW: entropy stratification and self-similarity

A real theoretical understanding of the equilibrium structure of dark matter halos, or of the processes that lead to it, is still lacking in the general picture of structure formation [198]. However, in the Seventies numerical simulations were developed and used to understand the mechanisms of gravitational clustering, and the evolving quality of the codes, together with the increasing resolution and computational power, made them the preferred tool to study the formation of Cold Dark Matter (CDM) halos. The success of numerical simulations in reproducing the observed dynamical properties of galaxies and larger systems depends on the scale investigated, and there is no agreement about the actual shape of DM halos and the mass distribution of substructures, due to inconsistencies between the results of simulations and observations (this topic will be extensively addressed in the next Chapters); however, simulations indeed reproduce well the mechanism of hierarchical clustering, and the latter enjoys a much broader consensus in being the actual process responsible for structure formation. [2] Having given simulations the credit they deserve, it is worth to investigate some features of the simulated halos that may seem quite surprising.

The most evident property of halos born through hierarchical clustering is the self-similarity: no matter the mass scale, they all belong to a one-parameter family of curves, known as the Navarro, Frenk & White (NFW, [113],[114]) profile

$$\rho(x) = \frac{M_{vir}}{4\pi R_{vir}^3} \frac{c^2\, g(c)}{x\,(1+cx)^2} \ ; \tag{1.42}$$

[2] There is still, however, much debate regarding this issue, and models describing other scenarios, such as the monolithic collapse of structures, are not ruled out yet.

here M_{vir} and R_{vir} are the virial mass and radius, x is the normalized radial coordinate $x \equiv r/R_{vir}$, c is called the *concentration parameter*, and $g(c) \equiv [\ln(1+c) - c/(1+c)]^{-1}$. The NFW is the spherically averaged fit to the density profiles obtained in simulations, and it is interesting to see that it holds for any Einstein-de Sitter Universe [32], rather than being characteristic of the particular cosmology of the ΛCDM model. Fig. (1.1) is taken from [114] and shows the NFW fits to halos of different masses in different cosmologies (Standard CDM and ΛCDM, with different density parameters and spectral indexes), highlighting the NFW flexibility in reproducing simulated systems in different universes.

Although in principle the NFW is a two-parameters family of curves (namely M_{vir} and c), from statistical analysis of the simulated halos it turns out that there is a mild anticorrelation between the concentration and the halo mass, that was originally parameterized by [114] (see also [25],[108]); I obtained the relation

$$c = 9.5 \left(\frac{M_{vir}}{10^{12} M_{\odot}} \right)^{-0.13} \tag{1.43}$$

at $z = 0$, after re-evaluating it with the cosmological parameters used in this work (see for comparison [79] and [58]). As it turns out, the concentration c increases with the redshift of formation while decreasing with the halo mass, thus fulfilling the hierarchical clustering requirements.

Regarding the velocity distribution structure, although it can vary from particular simulation to simulation, there is general agreement now that the NFW σ profile is isotropic in the centre of the halo, and becomes radially anisotropic moving outwards, mirroring the hierarchical mass accretion ([32],[174],[84]).

The NFW result has been confirmed by a number of subsequent studies (see for instance [32],[69],[110],[84],[86]), although there is some disagreement regarding the innermost value of the logarithmic slope γ. NFW argued that a fitting formula where $\gamma = (1+3y)/(1+y)$ (where $y = r/r_s$ is the radial coordinate in units of a suitably defined scale-radius r_s) provides a very good fit to the density profiles of simulated halos over two decades in radius. Some authors (see [110],[77],[70]) have argued that γ converges to a value of ~ -1.5 near the center, rather than -1 as expected from the NFW fit. Others [94] initially obtained much shallower inner slopes ($\gamma \sim -0.7$) in their numerical simulations, but

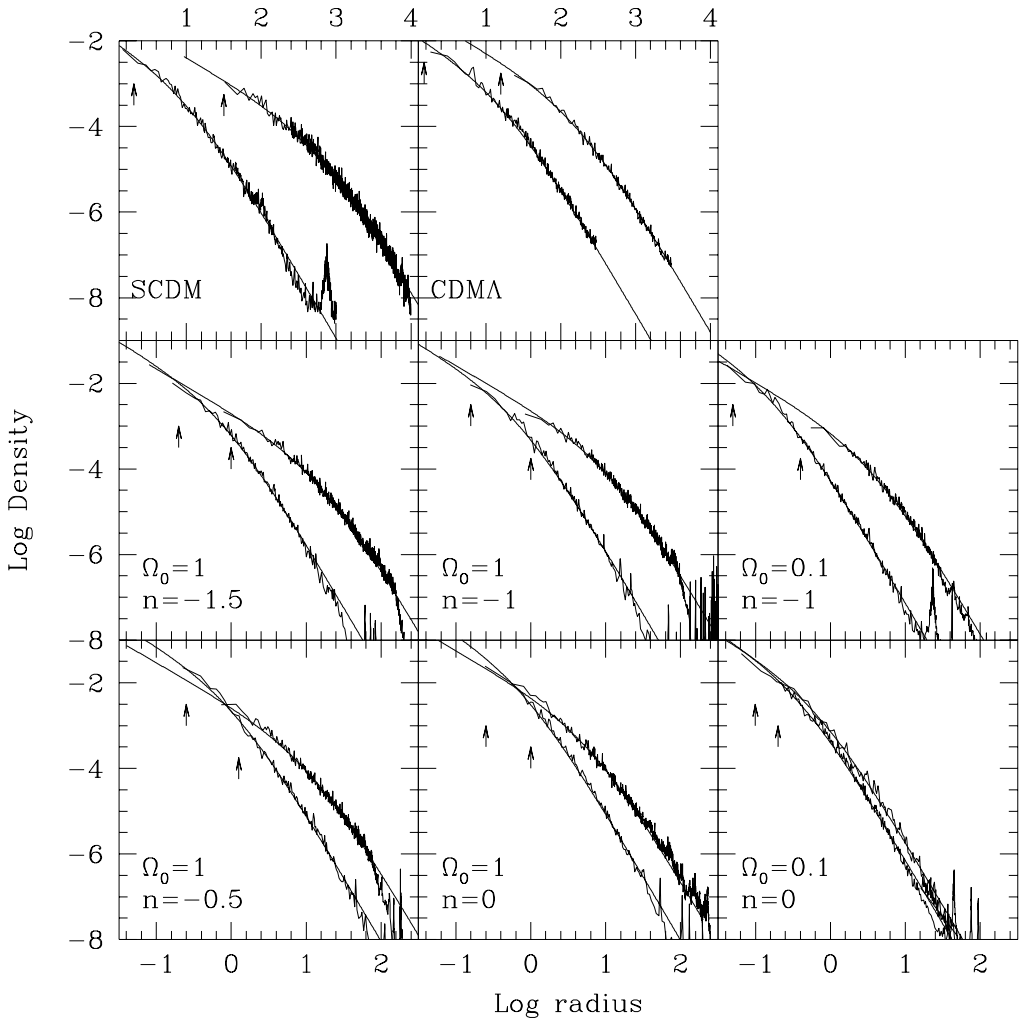

Figure 1.1 Density profiles of simulated halos in different cosmologies [114]. In each panel, the lower-mass halo is represented by the leftmost curve; the *solid smooth curve* is the NFW fit. *Left panels*: Standard CDM model ($\Lambda = 0$). *Right panels*: ΛCDM model. In each panel the varying cosmological parameters are specified. Radii are in kiloparsecs (*scale at top*); the arrows indicate the softenign length in each simulation.

have now revised their conclusions; these authors now argue that CDM halos have steeply divergent density profiles but, depending on evolutionary details, the slope of a galaxy-sized halo at the innermost resolved radius may vary between -1.0 and -1.5.

From the theoretical point of view, a number of plausible arguments have been advanced in order to try and explain the innermost behaviour of dark matter density profiles from collisionless dynamics' principles. These efforts, however, tend to give non-unique results and have so far been unable to explain the remarkable similarity in the structure of dark matter halos of widely different mass formed in a variety of cosmogonies ([64],[168],[119],[97]). As claimed in [199], the self-similarity would put a constraint on the slope of the power spectrum of primordial fluctuations, pinning it down betwenn $-3 < n < -1$. However, as will also be discussed in this Thesis, the self-similarity of halos can well be a numerical artifact or a lack of relevant physics in the inputs of simulations.

The self-similarity of dark matter halos can be investigated in phase-space, where it shows some more interesting facts. By examining the coarse-grained phase-space structure of CDM halos, Taylor & Navarro [173] argued of a pattern followed by all CDM-NFW halos regardless of virial mass; the *phase-space density*, a quantity defined in terms of the spatial density and the velocity dispersion profiles, can be expressed as a power law as a function of radius: $\rho/\sigma^3 \approx r^{-\alpha}$, with $\alpha \approx 1.875$; see Fig. (1.2).

Moreover, this slope coincides with that of the self-similar solution derived by Bertschinger [9] for the equilibrium phase-space structure of an object forming under spherical secondary infall of a gas of adiabatic index $\gamma = 5/3$ onto a point-mass seed in an unperturbed Einstein-de Sitter universe. Interestingly enough, the spatial density profile of the Bertschinger's system is a power law of constant slope $r^{2\alpha-6}$, quite different from the NFW. Notice that for the gas, the quantity $\rho^{5/2}/P^{3/2}$, where P is the pressure, is equivalent to the phase-space density, and is a measure of the local entropy of the system: the two are inversely proportional. Thus, for a DM halo, the phase-space density can be interpreted as an entropy measure, and the power-law dependence on radius of ρ/σ^3 describes an equilibrium configuration characterized by an entropy profile with a minimum in the center of the halo, and increasing outwards. It may well be that this entropy stratification is a fundamental property that underlies the self-similarity of CDM halos [173].

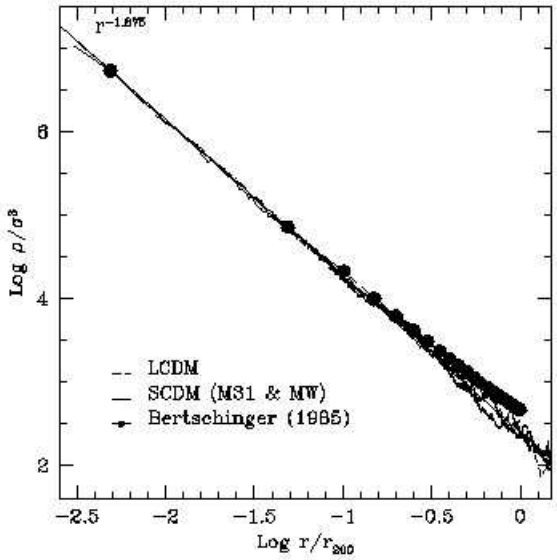

Figure 1.2 The phase-space density ρ/σ^3 as a function of radius, as shown in [173], with the Bertschiner's solution compared to the NFW .

There is more. Assuming that the phase-space density profile of a collisionless isotropic system is a power law of slope $\alpha = 1.875$, the Jeans' equations are satisfied by a one-parameter family of density profiles; the parameter k can be chosen as the ratio between the velocity dispersion and the circular velocity at the radius where the latter peaks. The Bertschinger's solution can be recovered for $k = \alpha = 1.875$, and the spatial density profile is also a power law. Very interestingly, the NFW profile belongs to this same family of curves, with $k \simeq 2.678$; this correspond to a critical value, above which there is no sensible, non-vanishing, monothonic profile in the center of the halo; see Fig. (1.3). Also, this is the critical value that correspond to the maximally mixed, most uniform phase-space distribution function, as shown if Fig. (1.4). In other words, given the entropy stratification constraint, the NFW is the highest-entropy profile. The theoretical explanation of these features is unknown [173].

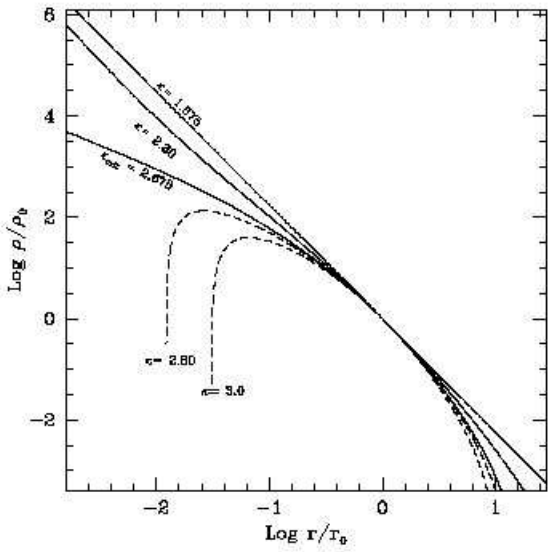

Figure 1.3 Density profiles corresponding to the Bertschinger's solution, for different values of the parameter α; the NFW corresponds to the critical solution, beyond which the profiles are unrealistic [173].

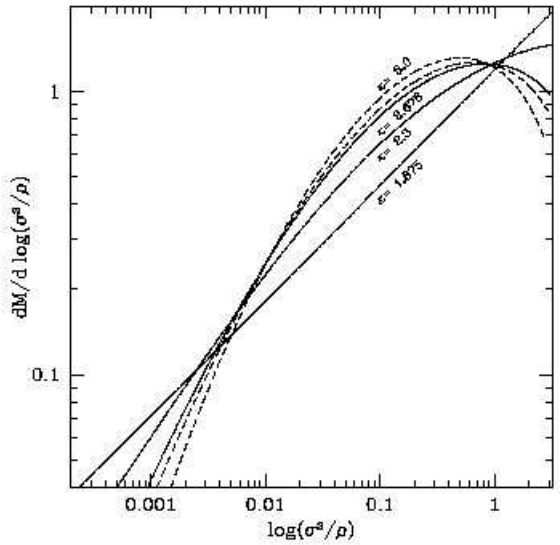

Figure 1.4 The phase-space distribution functions for the curves of Fig. (1.3), showing that the NFW is the maximally mixed configuration, corresponding to the most peaked DF [173].

1.3.2 Phase-space mixing and violent relaxation

One of the questions that are still unanswered is, how does a system choose its equilibrium state? Two scenarios are possible in principle (see for comparison [10]): (i) the final configuration of the halo is a reflection of the particular initial conditions of hierarchical clustering, *i.e.* the spectrum of fluctuations; (ii) the final state is favoured by some fundamental physical principle, that erases the memory of initial conditions. Smooth theoretical halos belong to the second class of objects; simulated halos belong to an hybrid class between the two. In fact, despite the analogy of (ii) with the description of the NFW as the maximally mixed configuration compatible with entropy stratification, the NFW itself is just the spherically averaged fit to the mass distribution of each simulated halo or subhalo, with the averaging procedure smoothing out the substructures, while the mass function actually conserves the hierarchy all the way through.

An elegant way to treat the equilibrium configuration of smooth halos would be to use the **maximum entropy** principle, exploiting the phase-space distribution function as a probability density; the equilibrium configuration would then be the one that maximises the quantity

$$S \equiv -\int_{phase\ space} f\ ln f d^3\mathbf{x} d^3\mathbf{v}\ . \tag{1.44}$$

Unfortunately, for self-gravitating systems of point masses with a finite total mass and energy, the entropy does not have a maximum, but can be increased with no limits simply by increasing the system's degree of central concentration [10].

An important consequence of this fact is that dark matter halos are not by themselves in long-term thermodynamical equilibrium, but constantly evolve into states of higher concentration and entropy. Althoug this is not the place to investigate such issues, it could be that the cuspy structure of the NFW stems directly from the absence of a maximum entropy state.

To understand the evolution of a system of point particles like a dark matter halo, with no underlying principle leading to equilibrium, two processes have to be taken into account.

The first is called **phase mixing**, and it is crucial in understanding the behaviour

of halos in numerical simulations, as will be clear in the following. Consider the system of N points shown in Fig. (1.5), that at some initial time t_0 occupies a volume of phase-space with constant $f = 1$. The system evolves in the Hamiltonian $H = p^2/2 + |q|$ of a point mass in $1D$ gravity; as time passes, volumes of $f = 1$ (black) get stretched out and folded together with volumes of $f = 0$ (white). The evolution is governed by the Boltzmann's equation, thus the distribution function f is conserved; the density of phase points in the spiral pattern into which the system evolves is the same as in the original configuration. However, the true f is not accessible to observations; an observer can only measure the average DF in a small volume around each point, *i.e.* the *coarse-grained* distribution function $\bar{f}$. At sufficiently small times, the observer can resolve small volumes around a point such that there are no white regions inside, and the measured $\bar{f}$ is actually the true f; but as time goes by, around $t \sim 100$ any distinction is barred by the finite resolution of any observation, and the observer can only measure an average of black regions blended with white ones. This makes her/him see a $\bar{f}$ decreasing in time around each point. In addition, the true f shows a very complex and continuosly evolving pattern, while equilibrium is reached in the coarse-grained sense, *i.e.* after a while $\partial_t \bar{f} = 0$ [50].

The meaning of the collisionless Boltzmann's equation can be analyzed from this point of view; while stating that f is constant, it also insures that $\bar{f}$ is *not increasing* along any trajectory in phase-space accessible by the system. The density of points in phase-space is diluted while the incompressible fluid represented by f is mixed with "air", in the form of stripes void of phase points.

The entropy defined by Eq. (1.44) is constant, since f is constant. However, by replacing f with $\bar{f}$ one obtains an entropy $\bar{S}$ that increases anytime $\bar{f}$ decreases along an orbit due to phase mixing; this sounds familiar, resembling the increase in entropy of a thermodynamical system when it moves towards thermal equilibrium [10]. In this sense, the evolution of the coarse-grained DF towards a minimum phase-space density brings the system towards more relaxed, more probable states. Notice however, that unless we can define a minimum phase-space density allowed for the system, we cannot find a maximum entropy state, not even in the coarse-grained sense; this is the case of the NFW, where the phase-space density is an unbroken power law with no minimum. For such systems, we can

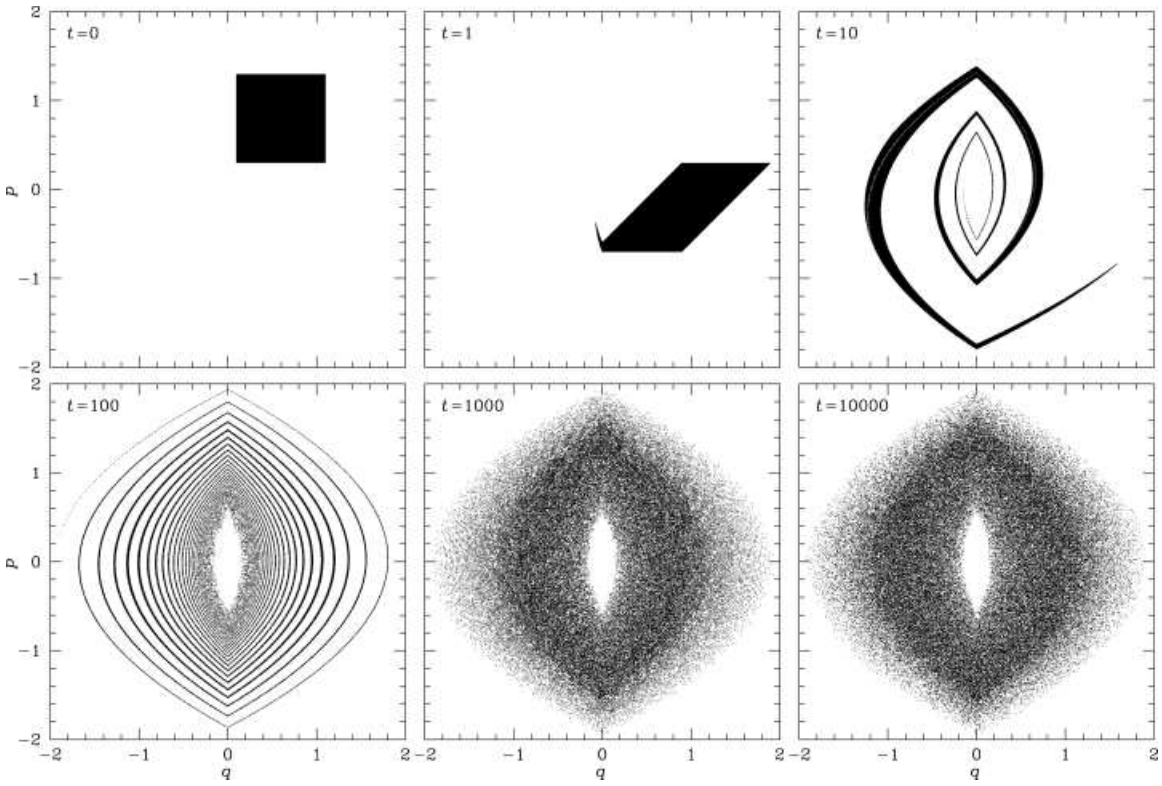

Figure 1.5 Demonstration of phase mixing; the evolution of a system of phase-space points under $1D$ gravity. The DF is constant at all times (1 or 0), but at late times, the coarse-grained system features a smooth distribution and a lower density [50].

only argue that they cannot evolve from a state A to a state B if $\bar{S}(B) < \bar{S}(A)$.

In the scenario of hierarchical clustering, where structures are formed through accretion of smaller units, another process is fundamental in shaping the final state of dark matter halos, and is called **violent relaxation** [100]. Rapid changes in the overall gravitational potential, during the collapse and the whole merger history of dark matter halos, provide relaxation on relatively short timescales (compared to the collisional case, for instance); this process governs the nonlinear evolution of halos into a final state characterised by structural regularities, with a universal density profile that does not depend on mass, on cosmological parameters or on the initial fluctuation spectrum (after smoothing out subtructures) [198].

During violent relaxation, the volume of phase-space accessible by the system increases [10]. This can be understood in the following way: consider a system of point masses uniformly distributed in a sphere, with a given distribution of initial velocities (like a DM halo), and consider a particle located somewhere in the sphere. Because of self-gravity, the particle will be pulled towards the centre of the system, and at the same time the potential well will deepen because of the infalling mass (all the other particles behave more or less in the same way than our test particle); the particle will gain a lot of kinetic energy, and when it passes near the centre and is on its way out again, the system is re-expanding, thus the potential well the particle has to climb is shallower than before. The particle will reach the potential at which it originally started with an excess of kinetic energy. Thus, the phase-space region of velocities and positions it can reach is wider than before [10].

Notice the difference between mixing and violent relaxation. The first process decreases the phase-space density around any point while conserving the phase-space volume; the second increases the phase-space volume accessible by the system, not necessarily altering the density of points. However, violent relaxation can increase the phase dilution by providing additional volume to the system, so it can be considered as another source of mixing.

While nobody knows whether mixing is well represented in numerical simulations, and the role it potentially plays, violent relaxation is thought to be responsible for the

universal density profiles, as well as the spin and shape distributions, of CDM simulated halos (as stated in [198]). In particular, the (smoothed) NFW density profile is the outcome of such process; its dependence on the halo mass, or on the initial power spectrum or cosmological context, is entirely upon the value of the concentration c, while the distribution itself is universal [198]. Moreover, the NFW fitting formula is a good representation of the mass distribution of halos originated through dissipationless hierarchical clustering in *any* Einstein-de Sitter universe [32], and the systematic dependences of c, on $P(k)$ and Ω can always be understood in terms of different formation times in different cosmologies [198]. Gravitational potential fluctuations during the collisions and mergings which characterize hierarchical clustering in simulations are evidently strong enough to cause convergent evolution [198].

1.4 Observations *vs* simulations: the cusp issue and the problem of substructures

When the predictions of the CDM model are tested against observations, some unpleasant facts about the halo equilibrium structure come into the spotlight.

The most succesful tool in studying the mass distribution of galactic dark matter halos is the spirals' rotation curves, that is particularly useful in investigating the inner density profile. Dynamical analysis of these curves shows, with increasing precision, that the favoured density profile (the best in fitting the observed data) is flat, corelike, with a central density significanlty lower than the NFW (see for instance [152],[16],[46],[196], [170],[72],[159], [73],[74]). To solve this striking disagreement, several authors (*e.g.*, [161],[1]) recurred to a framework different from the standard cosmology; however, as argued by [41] (and see references therein), neither self-interacting nor warm DM cannot explain the observed features of the inner halos. Alternatively [173] argue that the discrepancy arises from the imperfection of the numerical approach in simulating regions where the overdensities exceed $\sim 10^6$ and where the particles may have completed thousands of orbits during a Hubble time.

In addition, the DM density profiles inferred from observations do not show any

self-similarity; both the amplitude and shape of the profile depend strongly on the halo mass, as will be extensively discussed in Chapter 3.

The evolution of numerical simulations in 30 years has underlined another very important issue about hierarchical clustering, and another significant offset between theory and observations. By measuring the two-point correlation function of galaxies, we can infer a well defined power-law down to subgalactic scales, where the distribution is highly nonlinear. In the original formulation of the theory, Peebles [128] argued that the galaxy distribution and the mass distribution inside galaxies form an unbroken, scale-invariant or fractal-like hierarchy, thus reflecting the dynamical stability of this arrangement. In the same year, White & Rees [201] argued the contrary; a virialised clump of non-dissipative dark matter would not mantain a hierarchical structure, but would evolve into a monolithic halo with a well defined centre and a smooth mass distribution. As an example, consider a single cluster halo, containing many galaxies and not a single "supergalaxy"; the dark matter component is smoothed by virialization, while the baryons in single galaxies are concentrated enough by dissipative processes to avoid "overmerging" later on [199].

This is a sore point for numerical simulations. Still today, simulations confirm the theoretical expectation of a self-similar subhalo population, accoding to which galactic systems are simply scaled-down versions of clusters [55], with the result that simulated galaxies and groups feature an overaundance of substructures, with a mass function at small scales that is between one and two orders of magnitude higher than inferred from observations (see Chapter 6, and for instance [92],[111],[204],[91]). In addition to not being observed, such an overabundant subhalo population would represent a serious problem for disk galaxies; the presence of too much substructure would in fact mess up the observed galactic scaling relations (see Chapter 2), and cause dynamical heating and disruption of the fragile thin disk. In ordet to fit spirals into the hierarchical picture, the dark matter halos hosting them must assemble and be well relaxed relatively early, meaning that the last major merging events are expected to be sufficiently far in the past, to allow the disk to form and evolve unperturbed. In contrast, although galaxies in clusters are embedded in common halos, these halos can still feature significant substructure; in fact, they are relatively young, and still far from equilibrium [199]. Notice that the difference in scale

between these systems mirrors not only their different formation times and ages, but also a different mean density or concentration c.

The problem regarding real halos is twofold: on one hand, it may be that the equilibrium configuration of dark matter halos is always smooth, and that cluster halos simply have not had enough time to completely relax; on the other hand, there may be a mass-dependence trend for the survival of substructures, with baryons condensing in the subunits that may play a significant role (see Chapter 6).

The cusp issue and the substructure problem arising in simulations are linked. The explanation of the self-similarity of the NFW may reside in the radial stratification of the phase-space density, as explained before; if this is the case, the shape of the profile and the preservation of the hierarchy on the whole range of halo masses seem to be interconnected, in the sense that the NFW is the natural final state of the hierarchical clustering process. Hence, to deny the NFW means to deny the whole picture of structure formation as it is formulated today. This actually does not seem acceptable, given the number of successes of the model.

On the other hand, it is a fact that the self-similarity itself is not proven in real systems, nor is the validity of the density profile.

One way out is admitting that we are massively biased when we investigate DM halos observationally, since we actually see only the luminous component that evolves inside them; we do not really know how a pure DM halo looks like, or whether the presence of the galaxy affects its shape. In this case, there is a way to reconcile theory and observations, by modelling the halo reaction to galaxy formation and its subsequent evolution into different equilibrium structures, triggered by dynamical interactions between the dark matter and the baryons. This is the point of view adopted in this Thesis.

1.5 Galaxy formation and scaling relations

Galaxies form from the collapse of baryons inside the potential wells of dark matter halos, so their properties are expected to be regulated by the structure and formation history of their hosts, and the environment surrounding them. The dependence of the galactic properties

on those of the halo has been observed, in the form of *scaling relations* between the mass distribution and geometry of the galaxy and the halo structural parameters. The mass and angular momentum of the material available for galaxy formation, as well as the rate of interactions between galaxies, are determined by the halo structure and its evolution in the hierarchical picture ([200]). In addition, the global properties of galaxies depend on how the gas cools into clouds and how these fall and collapse into the halo potential, and on the characteristics of star formation and feedback.

The current theory of galaxy formation is a hybrid between numerical simulations, that account for the dark component, and semi-analytical models that take care of the baryonic one. The newest codes for SPH simulations are indeed refined and use the latest semi-analytical prescriptions to reproduce the observed features of galaxies; the general picture is thought to be understood ([197],[40],[107]), although many observational evidences are still not accomodated in the scenario (see above). Among these, spiral galaxies present problematic issues, regarding their dynamics and the geometry of their mass distribution. In fact, all the processes leading to galaxy formation affect each other in highly nonlinear ways, and involve a wide range of scales; simulations are not always the best tool in investigating such mechanisms, and semi-analytical models sometimes perform better. Here I present the current picture of galaxy formation, along with its shortcomings [3].

In the current scenario ([40],[107]), after decoupling baryons are trapped into the potential wells of the growing dark matter perturbations, and initially follow the same evolution patterns; the two components are initially well mixed, *i.e.* they share the same phase-space structure. They both start to collapse in some overdense regions that will become the centers of the dark matter halos, and while the density is low their dynamical behaviour is identical; however, contrary to the baryonic one, the dark matter collapse is dissipationless, and it halts when the system virialises.

The baryonic collapse proceeds, leading to densities high enough for radiative cooling to become effective; at this stage, the process accelerates and the baryons dynamically decouple from the dark component, fragmenting and condensing into self-gravitating units.

[3]The particular model discussed here is intended to give a general picture of the current theory; newer models by other authors may differ in some details.

The gravitational potential of the halo regulates the infall of the clouds towards the denser central regions of the system.

Tidal torques, originating with the mass accretion of the halo, spin up the clouds that, depending on the amplitude of the angular momentum J_z and on the details of the trajectories towards the inner regions, may or may not collapse along a preferential direction, forming a disk or a spheroidal component. At the same time, density in the central regions reaches the density threshold for star formation to begin; depending on the availability of gas, *i.e.* on the clouds reaching the center of the halo, star formation regulates the amount of feedback and balances the subsequent evolution, by expelling some baryon fraction and regulating the infall of material.

From the results of numerical simulations and a set of semi-analytic prescriptions, a number of predictions regarding the structure of disk galaxies have been made ([40],[107]). Of particular interest in this Thesis, the mass distribution and the geometry of the disk are expressed as functions of the halo mass and angular momentum.

The angular momentum J_z of simulated halos is characterized by the dimensionless **spin parameter** [124]

$$\lambda \equiv \frac{J_z \ |E|^{1/2}}{G \ M_{vir}^{5/2}} \ , \tag{1.45}$$

that can be approximated by the ratio between the rotational and circular velocity $\lambda \approx V_{rot}/V_c$, and expresses the degree of ordinate motions around the axis of rotation. The effective size of the disk forming inside the halo in simulations strongly depends on the clouds' angular momentum along the spin axis, which in turn depends on the halo's J_z; the spin parameter is therefore a useful tool to link the geometrical properties of the disk with the dynamics of the halo.

For a NFW halo of virial mass M_{vir} and concentration c, the mass profile is

$$M(x) = M_{vir} g(c) \left(ln(1+cx) - \frac{cx}{1+cx} \right) \ , \tag{1.46}$$

in terms of the radial coordinate $x = r/R_{vir}$. The total energy of the halo is recovered as

$$E = -\frac{G \ M_{vir}^2}{2 \ R_{vir}} \ f_c \ , \tag{1.47}$$

with f_c being a shape factor, function of the halo concentration. Given the circular velocity $V_c^2 = GM/r$, the halo total angular momentum is then

$$J_z = \sqrt{2/f_c}\lambda M_{vir} R_{vir} V_c \ . \tag{1.48}$$

The baryons inside the halo are supposed to collapse in a disk of mass

$$M_D = m_d \ M_{vir} \ , \tag{1.49}$$

with m_d a universal fraction [107]. As a consequence, the total disk angular momentum is also a universal fraction j_d of that of the halo:

$$J_D = j_d \ J_z \ . \tag{1.50}$$

Notice that this assumption is highly unrealistic, since the mass-to-light ratio in spirals is a strong function of mass, with small systems significantly more dark matter-dominated with respect to the massive ones ([151],[7],[157]).

The disk profile is assumed exponential, with scale-length R_D, and the specific angular momentum j_z is supposed to be conserved between the baryonic and dark component during the collapse. The resulting disk scale-length as a function of the halo parameters is then:

$$R_D = \frac{1}{\sqrt{2}} \left(\frac{j_d}{m_d} \right) \lambda R_{vir} f_c^{-1/2} f_R(c, \lambda, m_d, j_d) \tag{1.51}$$

where

$$f_R(c, \lambda, m_d, j_d) = 2 \left[\int_0^\infty e^{-u} u^2 \frac{V_c(R_D u)}{V_{vir}} du \right]^{-1} \ ; \tag{1.52}$$

for a detailed description, refer to [107]. From these prescriptions, the total rotation curve of the system halo + disk galaxy is obtained simply as $V_{TOT}^2 = V_D^2 + V_H^2$.

As will be discussed in the next Chapter, observations of disk galaxies show that the dependences of the disk properties on halo dynamics are highly nonlinear, and that the simple assumptions of this model are not suitable to yield the observed disk geometries or masses [176].

1.6 Plan of the Thesis

In Chapter 2 I will introduce a refined model of galaxy formation, that is based on the observed scaling relations existing between the dark and luminous components of galaxies, that circumvents the difficulties presented in the previous Section, and makes predictions about the dynamical properties of galactic halos from those of the disk galaxies. This allows me to constrain the halo mass accretion history.

In Chapter 3 I will present an observational counterpart to the NFW, that can be practically used to infer the global properties of halos (like the virial mass for instance) from the observed rotation curves, and that introduces a breaking in the self-similarity of halos.

In Chapter 4, I will further analyse the properties of the NFW, higlighting that the discrepancy between the expected mass distribution and the data coming from real systems is not due to numerical artifacts, but stems from the lack of a proper modelling of all the physical mechanisms involved in galaxy formation.

In Chapter 5, I will finally present a theoretical model of halo evolution triggered by galaxy formation. First, I will describe the evolution of the halo equilibrium structure in phase-space, when it is perturbed by angular momentum transfer, that modifies the anisotropy profile with the injection of tangential motions; according to the amplitude of the perturbation, the halo can acquire cored equilibrium configurations. Second, I will present a plausible physical mechanism to account for such a halo evolution, in the form of dynamical friction exerted by the DM on the baryonic clouds collapsing to form the protogalaxy.

In Chapter 6, I will describe my work-in-progress about the numerical simulation of dynamical friction, for the double purpose of testing the theoretical model of Chapter 5, and of addressing the issue of the disruption of substructures in galactic DM halos.

In Chapter 7 I will finally conclude.

Chapter 2

The Spin of Spiral Galaxies

I present a model for computing the angular momentum and spin parameter distribution function of dark matter halos hosting real spiral galaxies, entirely based on the observed scaling relations between the geometrical and dynamical properties of the galaxies and their hosts. I then use the spin parameter inferred from the observations as a tool to constrain the mass accretion history of dark matter halos.

2.1 Introduction

The spin of DM halos is thought to be originated during major mergers, where large-scale tidal interactions transform the orbital angular momentum of the colliding objects into a coherent rotation of the final halo [65]. Although this mechanism can explain the halo spin, the connection to the rotational motions of the galaxies hosted inside the halos is not completely understood. In fact, even if at early stages the baryons share the same phase-space structure of the dark component, and in particular have the same specific angular momentum distribution, they then undergo a number of physical processes (including radiative cooling and collapse, dynamical friction, star formation, heating and shocks, supernova winds and AGN activity) that dynamically decouple them from the DM to an unknown degree. For this reason, any determination of the halo dynamics from the baryons has to face the question of whether the baryons actually conserve any memory of it at all. On the other hand, it is plausible that the baryons and the host halo continue to dynamically

interact even after the galaxy formation, expecially when one considers global motions that, like the rotation around the spin axis, occur on scales comparable to the halo size and are therefore not largely affected by mixing, relaxation and local processes generally linked to feedback. So, as far as the spin is concerned, it is not far-fetched to expect a certain degree of self-regulation in the system galaxy-dark halo, in order to mantain a stable equilibrium configuration between the two components [176].

In the simplest scenario, the ratio bewteen the baryonic and the DM angular momenta is constant. In other words, the angular momentum per unit mass is conserved, and the only processes that affect its distribution are purely gravitational. This is a plausible picture if the baryons and the DM initially have similar phase-space distributions [176].

The collapse of the luminous component leading to the formation of a disk galaxy follows a preferential direction, thus setting the disk spin axis. The geometry of the disk is directly related to the initial dynamical state of the baryons, in particular the angular momentum distribution; provided a suitable scaling, this relates to the dynamics of the dark halo. In particular, [65] provided a link between the disk scale length and the halo angular momentum.

The tight connection between halo dynamics and disk geometry is quantified by the **spin parameter** λ [124], that proves to be a fundamental tool in the study of the formation of both the DM halo and the galaxy.

The physical meaning of the spin parameter is to represent the degree of rotation around a given axis in the motions of an object. In other words, one can represent the spin parameter as

$$\lambda \sim \frac{V_{rot}}{V_c} \tag{2.1}$$

where $V_c = \sqrt{GM(r)/r}$ and V_{rot} is the actual rotational velocity. A rotationally supported disk has $V_{rot}/V_c = 1$, while an object dominated by velocity dispersion has $V_{rot}/V_c \simeq 0$.

Mo and collaborators [107] described a procedure for the computation of the scale length of a disk embedded in a NFW dark halo of given mass and spin parameter, as yielded by numerical simulations (see Chapter 1 for a more detailed description). The model made use of a set of assumptions on the properties of the baryons, as dependent on the host halo: (i) the mass of the galactic disk is a *universal* fraction of the halo's; (ii) the total angular

momentum of the disk is also a fixed *universal* fraction of the halo's; (iii) the disk is thin and centrifugally supported, with an exponential surface density profile. The success of the model in reproducing real systems is limited [176].

In the present Chapter, I address the same issue from the opposite point of view, *i.e.* given the galactic observables, I infer the dark matter global properties. In particular, I provide a method for estimating the halo angular momentum J_z and the spin parameter λ of a DM halo hosting a spiral galaxy of measured mass and scale length. Instead of assuming arbitrary scalings between the baryons and the DM, the model relies on a series of empirical relations linking the disk geometry and mass distribution with the mass distribution and the dynamics of the halo, through the rotation curve.

For the sake of simplicity, I'll make use of the specific angular momentum conservation assumption, but it will be clear how to straightforwardly extend the method to more general cases.

More in particular, in a direct comparison with the Mo et al. method, we relax (i), and use instead an empirical relation that links the disk mass to that of its DM halo [157]; as for (ii), the baryonic angular momentum is therefore not a universal fraction of that of the halo, but rather depends on the mass-to-light ratio and on the chosen angular momentum conservation law between the components; (iii), the disk is still centrifugally supported, stable, and distributed according to an exponential surface density profile, but I'll also take into account the gaseous (HI+He) component, that turns out to give an important contribution to the overall angular momentum distribution, expecially in small galaxies. As for the shape of the DM profile, I'll present the results for a Burkert halo, in comparison with the NFW [26].

2.2 The halo angular momentum

Statistical studies about the observed properties of spirals, obtained from rotation curves and photometric measurements, allow for a set of scaling relations between the mass distribution and geometry of the systems galaxy + dark halo, in a range of masses including most of the population, with the exception of dwarves. For the purpose of computing the halo

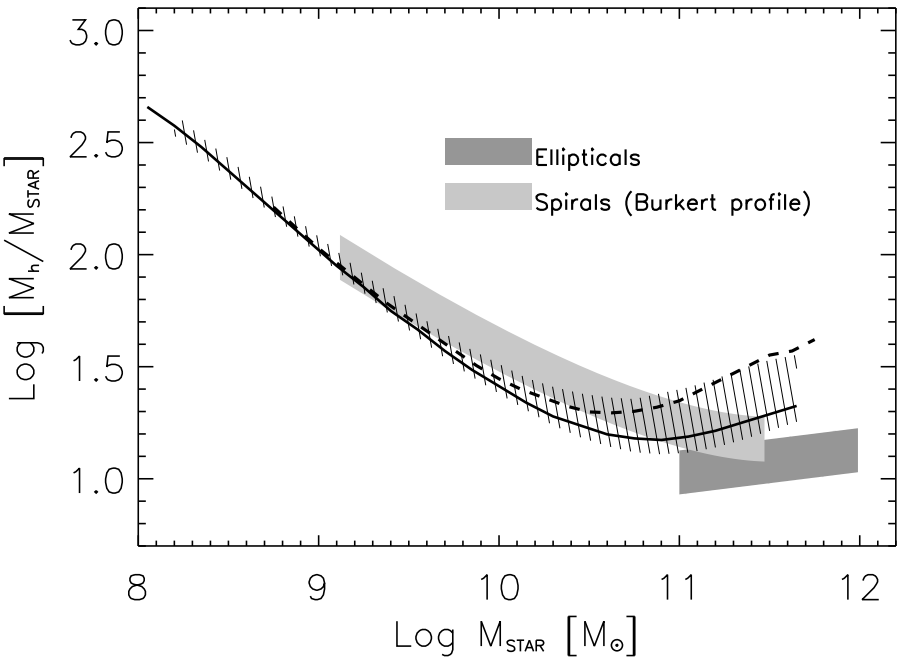

Figure 2.1 DM halo-to-stellar mass ratio as a function of the stellar mass [157]. The *dark shaded* area represents the data on giant elliptical galaxies [76]; the *light shaded* area represents data on spiral galaxies ([138],[152]).

angular momentum from the spiral observables, one needs to determine the ratio between the disk and halo mass, the link between the halo mass and the disk geometry, and the mass distribution of all the components; the gaseous baryonic component, lesser important mass-wise, is significant in its contribution to the angular momentum due to the fact that it is more diffuse.

The total mass of the stellar disk M_D that resides in a halo of mass M_H has been derived by the statistical comparison of the galactic halo mass function extracted from N-body simulations with the observed stellar mass function [157]:

$$M_D \approx 2.3 \times 10^{10}\ M_\odot\ \frac{(M_H/3\ 10^{11}\ M_\odot)^{3.1}}{1+(M_H/3\ 10^{11}\ M_\odot)^{2.2}}\ ; \tag{2.2}$$

it holds for halo masses between 10^{11} and about $3 \times 10^{12}\, M_\odot$, with an uncertainty around 20%, mainly due to the mass-to-light ratio used to derive the stellar mass function from the galaxy luminosity function; it is shown in Fig. (2.1).

This relation replaces the assumption (i) about a universal mass-to-light ratio

for spirals by [107], and is physically well motivated ([151],[7],[157]). In fact, the balance between two processes, namely cooling and feedback, leads to a ratio between the mass of the stellar disk and the halo mass that increases with the latter; the smaller the halo, the more the efficiency of feedback is enhanced, while the efficiency of baryonic cooling and collapse is diminished by the lesser halo gravitational potential.

The stellar disk is thin, gravitationally supported, with an exponential surface density profile described by

$$\Sigma_D(r) = \frac{M_D}{2\pi\ R_D^2}\, e^{-r/R_D}\ . \tag{2.3}$$

The characteristic scale-length R_D is the key parameter in defining the disk geometry, and is estimated from the disk mass, through dynamical mass determinations [138]:

$$\log \frac{R_D}{\mathrm{kpc}} = 0.633 + 0.379\ \log \frac{M_D}{10^{11}\, M_\odot} + 0.069\ \left(\log \frac{M_D}{10^{11}\, M_\odot}\right)^2\ . \tag{2.4}$$

This result is consistent with the scale-lengths inferred in previous works ([42],[158],[38]).

The halo mass distribution is inferred from the rotation curve; the majority of the observations of the rotational velocities of spirals yield a Burkert DM density profile as the best fit [26]. A statistical treatment is given by the Universal Rotation Curve (URC_0,[138]), a two-parameters family of curves for a Burkert halo, determined by the halo effective core density ρ_0 and core radius R_0. The halo density profile is thus given by:

$$\rho_H(r) = \frac{\rho_0\, R_0^3}{(r + R_0)(r^2 + R_0^2)}\ . \tag{2.5}$$

Correspondingly, the cumulative mass profile is given by:

$$M_H(< r) = 4\, M_0\ \left[\ln\left(1 + \frac{r}{R_0}\right) - \tan^{-1}\left(\frac{r}{R_0}\right) + \frac{1}{2}\ \ln\left(1 + \frac{r^2}{R_0^2}\right)\right]\ , \tag{2.6}$$

with $M_0 = 1.6\, \rho_0\, R_0^3$ being the mass contained inside the radius R_0.

The URC_0 itself provides a scaling for ρ_0 as a function of the disk mass:

$$\log \frac{\rho_0}{\mathrm{g\ cm^{-3}}} = -23.515 - 0.964\ \left(\frac{M_D}{10^{11}\, M_\odot}\right)^{0.31}\ . \tag{2.7}$$

For each given disk mass, the halo is therefore completely determined; the halo mass M_H is computed through Eq. (2.2), the virial radius of the halo is set by the cosmology through

$$R_H = [3\, M_H\, \Omega_M^z / 4\pi\, \rho_c\, \Omega_M\, (1+z)^3\, \Delta_H]^{1/3} \tag{2.8}$$

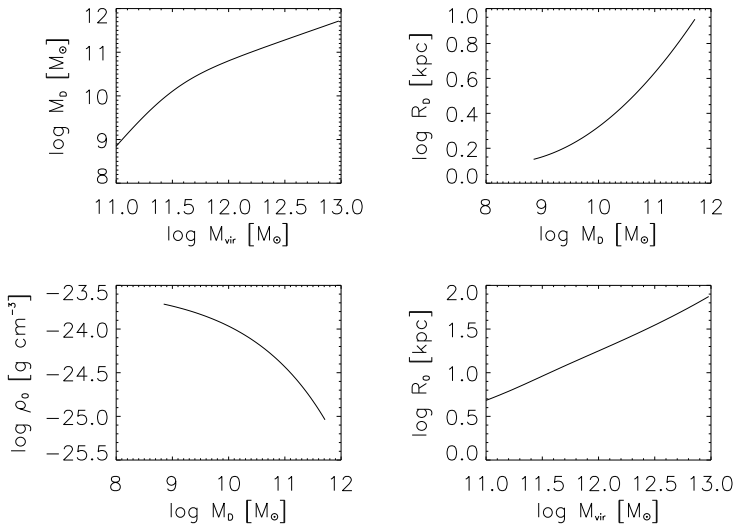

Figure 2.2 A summary of the empirical scaling relations adopted in the model; *top left*: stellar disk - halo mass; *top right*: disk mass - scale-length; *bottom left*: disk mass - halo central density; *bottom right*: halo mass - core radius.

the density ρ_0 is obtained through Eq. (2.7), and the core radius R_0 is then computed numerically by requiring that the mass $M_H(< R_H)$ inside R_H given by the r.h.s. of Eq. (2.6) equals the virial mass M_H. The resulting R_0 vs. M_H relation is approximated within a few percents by

$$\log\left(R_0/\mathrm{kpc}\right) \approx 0.66 + 0.58\,\log\left(M_H/10^{11}\,M_\odot\right)\;; \tag{2.9}$$

notice that these values of R_0 are obtained through a mass modeling of the whole mass distribution out to R_H, rather than from the decomposition of the inner rotation curves of single galaxies [152]. A summary of the scalings adopted by the model is given in Fig. (2.2).

Before considering the gas distribution in addition to the stars, I will compute the disk angular momentum and the Tully-Fisher relation for my mass spectrum, in order to compare this model with the NFW-Mo et al. theory and with observations.

The total circular velocity of the system is

$$V_c^2(r) = V_D^2(r) + V_H^2(r)\;. \tag{2.10}$$

For a thin, centrifugally supported disk the circular velocity is given by

$$V_D^2(r) = \frac{G\,M_D}{2\,R_D}\,x^2\,(I_0\,K_0 - I_1\,K_1)|_{x/2}\ ; \tag{2.11}$$

here $x = r/R_D$ and the quantity $B = I_0\,K_0 - I_1\,K_1$ is a combination of the modified Bessel functions that accounts for the disk asphericity [67]. The halo circular velocity is simply

$$V_H^2(r) = GM_H(<r)/r\ , \tag{2.12}$$

and it is useful to define the virial velocity $V_H \equiv \sqrt{GM_H/R_H}$. Given the scaling relations (2.2), (2.4), (2.7) and (2.9) linking the basic quantities of the system, only the disk mass is needed to completely determine the shape and amplitude of the velocity profile. Note that all the uncertainties on these relations combine to give a $10\% - 20\%$ total error on the determination of the velocity profile (see [175] and Appendix A).

A way of checking the performance of this model is through the computation of the Tully-Fisher relation. I obtained the B-band luminosity from the stellar disk mass, through the relation [157]

$$\log\left(\frac{L_B}{L_\odot}\right) \approx 1.33 + 0.83\,\log\left(\frac{M_D}{M_\odot}\right)\ ; \tag{2.13}$$

I then converted the related magnitude in the I-band, through the mean colour $B - I \approx 2$ [68]. In Fig. (2.3, *right*) I compare the resulting TF at $r = 3\,R_D$ with the data by [78], finding an excellent agreement.

The angular momentum of the disk is obtained as

$$J_D = 2\pi \int_0^\infty \Sigma_D(r)\,r\,V_c(r)\,r\,dr = M_D\,R_D\,V_H\,f_R\ , \tag{2.14}$$

with $x = r/R_D$, $f_R = \int_0^\infty x^2\,e^{-x}\,V_c(xR_D)/V_H\ dx$ acting as a shape factor, and $M_D = 2\pi\,\Sigma_0\,R_D^2$. Note that J_D depends linearly on both the mass and on the radial extension of the disk, while the DM distribution enters the computation through the integrated velocity profile, encased into the shape factor f_R; the latter slowly varies (by a factor 1.3 at most) throughout our range of halo masses.

In Fig. (2.3, *left*) I show the specific angular momentum of the disk, computed as $j_D = J_D/M_D$ from Eq. (2.14), as a function of the total circular velocity at $r = 2.2\,R_D$.

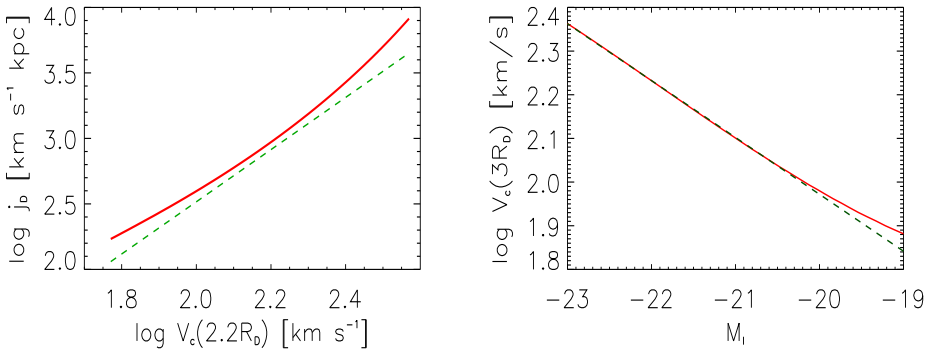

Figure 2.3 Left panel: the specific angular momentum of the disk as a function of the rotation velocity at $2.2\,R_D$. The *solid line* is the result from this model, adopting the Burkert profile; the *dashed line* is the best-fit relation from the data collected by [115], see their Figure 3. Right panel: the Tully-Fisher relation. The *solid line* represents the result from this model and the *dashed line* illustrates the fit to the data by [78].

Plotted for comparison is also the best-fit relation by [115] from their collection of data; note that these authors adopted a flat rotation curve, so that $f_R = 2$ and $j_D = 2\,R_D\,V_H$.

Fig. (2.4) shows a comparison between different models for the halo and baryonic mass distribution. The *black dots* represent again the specific disk angular momentum as a function of the total circular velocity in the current model, as in Fig. (2.3); the *pink dots* correspond to the same model, but with a halo described by the NFW profile; the *blue dashed line* is the result by the Mo et al. model; the *red line* is again the empirical relation by [115], with the *yellow* and *light blue shaded areas* representing its 1-σ and 3-σ regions respectively. Clearly, the model described here is the most successful in reproducing the empirical data.

I derive the halo angular momentum by assuming the conservation of the total specific angular momentum between the dark matter and the baryons:

$$J_H = J_D \frac{M_H}{M_D} \,, \tag{2.15}$$

an *ansatz* widely supported/adopted in the literature ([107],[182],[183],[27],[131]). Notice

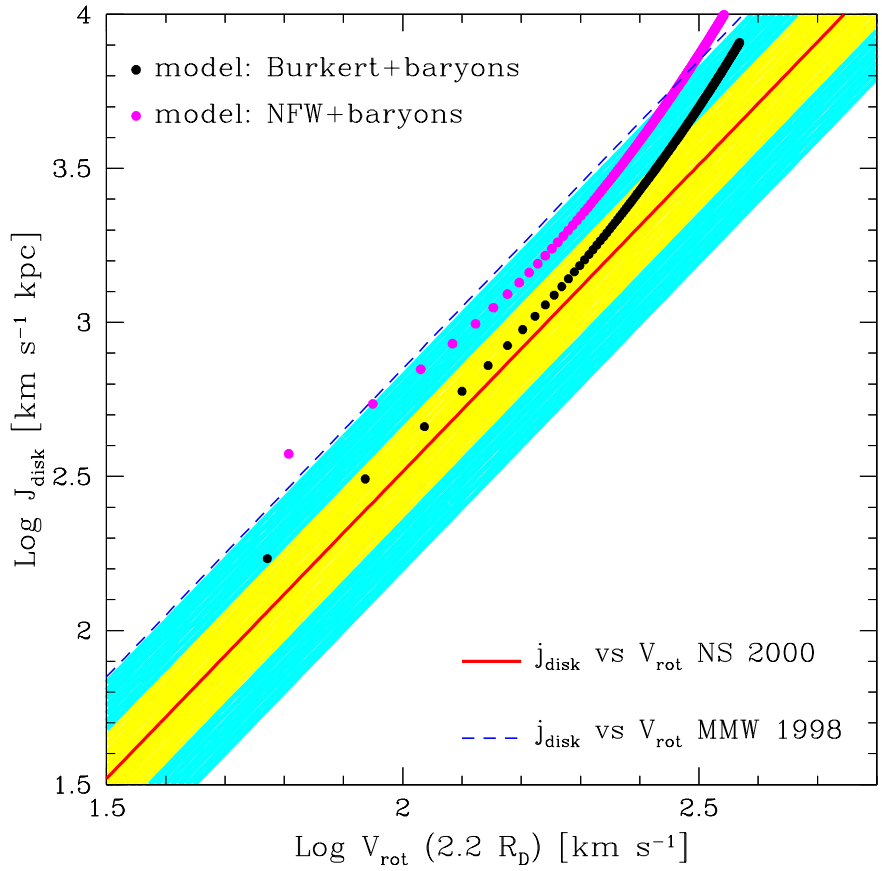

Figure 2.4 The specific angular momentum of the disk as a function of the rotation velocity at $2.2\,R_D$: Comparison with the NFW + Mo et al. model. *Black (lower) dots*: the result from this model, adopting the Burkert profile; *pink (upper) dots*: the result from this model, adopting the NFW profile; *blue dashed line* the Mo et al. model; *red line*: the best-fit relation by [115], with the 1-σ (yellow) and 3-σ (light blue) regions.

that the specific angular momentum conservation yields the maximum disk angular momentum, in the absence of any dissipation of j_z during and after the baryonic collapse. In any other case, a more general expression should be of the form $J_H = J_D\,\alpha(t,M)\,(M_H/M_D)$, where $\alpha(t,M) \geq 1$ takes into account dissipation of j_z and in principle depends on the halo mass and varies with time. Therefore the halo angular momentum may in principle be larger than that yielded by Eq. (2.15), even if unlikely (see the Discussion).

Small variations of J_D are magnified by a factor M_H/M_D in the value of J_H, i.e., the latter is rather sensitive to the mass and radial extension of the baryons, as shown in Eq. (2.14). For this reason I included in the computation, along with the stars, the gaseous component that envelops the disk of spiral galaxies.

The gas-to-baryon fraction in spiral galaxies is a decreasing function of disk mass, with a maximum ratio of ~ 0.5 for small spirals; I derived the total mass of the gas component from the disk luminosity (see above) through the relation

$$M_{\rm gas} = 2.13 \times 10^6\, M_\odot \left(\frac{L_B}{10^6\, L_\odot}\right)^{0.81} \left[1 - 0.18 \left(\frac{L_B}{10^8\, L_\odot}\right)^{-0.4}\right] \qquad (2.16)$$

by [139], where I included a factor 1.33 to account for the He abundance.

The tiny contribution to the total mass leaves the rotation curve virtually unaltered (in fact, $V_{\rm gas} \sim \sqrt{M_{\rm gas}/R_{\rm gas}}$). However, the gas is much more diffuse than the stars, reaching out to several disk scale-lengths ([36],[43]), and since most of the angular momentum comes from material at large radial distances ([182], and Eq. (2.14)), I expect the gas to add a significant contribution to the total angular momentum, especially in small spirals.

The detailed density profile of the gas in spirals is still under debate in the literature. However, I am confident that the main factors entering the computation of the gas angular momentum $J_{\rm gas}$ are just the gas total mass $M_{\rm gas}$ and the radial extension of its distribution, in analogy with Eq. (2.14); in other words, I expect the details of the gas profile not to significantly affect the results. In order to check this statement, I computed the total gas angular momentum for 3 different gas models, *i.e.* (i) a disk-like distribution (DL), with scale length αR_D; (ii) a uniform distribution (U) out to a radius βR_D; and (iii) an $M33$-like gaussian distribution (M33; [36]):

$$\Sigma^{\rm DL}_{\rm gas}(r) \;=\; \frac{M_{\rm gas}}{2\pi\,\alpha^2 R_D^2}\, e^{-r/\alpha R_D}$$

$$\Sigma^{\rm U}_{\rm gas}(r) = \frac{M_{\rm gas}}{\pi\,\beta^2 R_D^2}\,\theta\,(r-\beta R_D) \tag{2.17}$$

$$\Sigma^{\rm M33}_{\rm gas}(r) = \frac{M_{\rm gas}}{\pi\,(2k_1^2+k_2^2)\,R_D^2}\,e^{-(r/k_1R_D)-(r/k_2R_D)^2}\ ,$$

where θ in the second equation is the Heaviside step function. As fiducial values of the parameters, we adopt $\alpha \approx 3$ in the first expression, $\beta \approx 6$ in the second one [43], and $k_1 \approx 11.9$, $k_2 \approx 5.87$ in the last one [36]. Each profile has been normalized to the total gas mass $M_{\rm gas}$ as computed from Eq. (2.16).

As in Eq. (2.14), the gas angular momentum will be

$$J_{\rm gas} = 2\pi \int_0^\infty \Sigma_{\rm gas}(r)\ r\,V_c(r)\,r\,dr = M_{\rm gas}\,R_D\,V_H\,f_{\rm gas}\ , \tag{2.18}$$

where the shape factor $f_{\rm gas}$ encodes the specific gas distribution. On comparing its values for the three models I found differences of less than 15%, and so confidently choose the gaussian profile as a baseline.

It is time to compute the halo angular momentum as a function of the total baryonic one:

$$J_H = (J_D + J_{\rm gas})\ \frac{M_H}{M_D + M_{\rm gas}}\ . \tag{2.19}$$

The gas is dynamically affecting the system mainly through its different spatial distribution with respect to that of the stars, adding an angular momentum component that is relevant at radii larger than R_D. The final spin parameter turns out to be significantly different if the gas is included; this is a conservative case, as will be clear in the next Section.

Note that I do not include a bulge component, since it would contribute with a negligible angular momentum and a mass of $0.2\,M_D$ at most; in any case, this is again a conservative assumption, since the bulge would slightly lower J_H after Eq. (2.19) and, as will be evident in the next Section, would lower the spin parameter and strengthen my conclusions.

2.3 The spin parameter

The spin parameter is a powerful tool to investigate galaxy formation, as it is strictly related to both the dynamics and the geometry of the system. By studying its dependence on halo mass and its distribution function across the galaxy population, I can gain some insight on the mechanisms of mass accretion and the history of halos.

The spin parameter is defined as

$$\lambda = \frac{J_H \, |E_H|^{1/2}}{G \, M_H^{5/2}} \ , \tag{2.20}$$

where G is the gravitational constant and E_H is the total energy of the halo. The latter is computed as $|E_H| = 2\pi \int dr \, r^2 \, \rho_H(r) \, V_c^2$ after the virial theorem, assuming that all the DM particles orbit on circular tracks.

An alternative definition used in simulations [25] is given by the first equality in the following:

$$\lambda' = \frac{J_{\rm H}}{\sqrt{2} \, M_H R_H \, V_H} = \frac{J_H + J_D + J_{\rm gas}}{\sqrt{2}(M_H + M_D + M_{\rm gas}) \, R_H V_H} \ ; \tag{2.21}$$

the definition is such that $\lambda = \lambda'$ for a NFW halo. I found the second equality after Eq. (2.19), and determined that for Burkert halos the ratio λ/λ' is between $1.1 - 1.3$ in the mass range $10^{11} - 3 \times 10^{12} \, M_\odot$. In Fig. (2.5) (*top panels*) I plot both λ and λ' as a function of the halo mass. I also highlight the difference in the value of the spin parameter when the gas component is included, especially in low mass halos. As is clear in Fig. (2.5), there is no strong evidence of a correlation between the spin parameter and the halo mass; the halo angular momentum originates from tidal torques during the episodes of mass accretion throughout its history, and the similarity across the whole mass range suggests a common formation pattern for all halos, in agreement with the hierarchical scenario.

To compute the probability distributions $\mathcal{P}(\lambda)$ and $\mathcal{P}(\lambda')$ of the spin parameters, I exploited the galactic halo mass function, i.e., the number density of halos with mass M_H containing a single baryonic core [157]. A good fit is provided by the Schechter function $\Psi(M_H) = (\Psi_0/\overline{M}) \, (M_H/\overline{M})^\alpha \, \exp\left(-M_H/\overline{M}\right)$, with parameters $\alpha = -1.84$, $\overline{M} = 1.12 \times 10^{13} \, M_\odot$ and $\Psi_0 = 3.1 \times 10^{-4}$ Mpc^{-3}; note that within our range of halo masses, this is mostly contributed by spirals. For the computation of $\mathcal{P}(\lambda)$ or $\mathcal{P}(\lambda')$, I randomly picked a

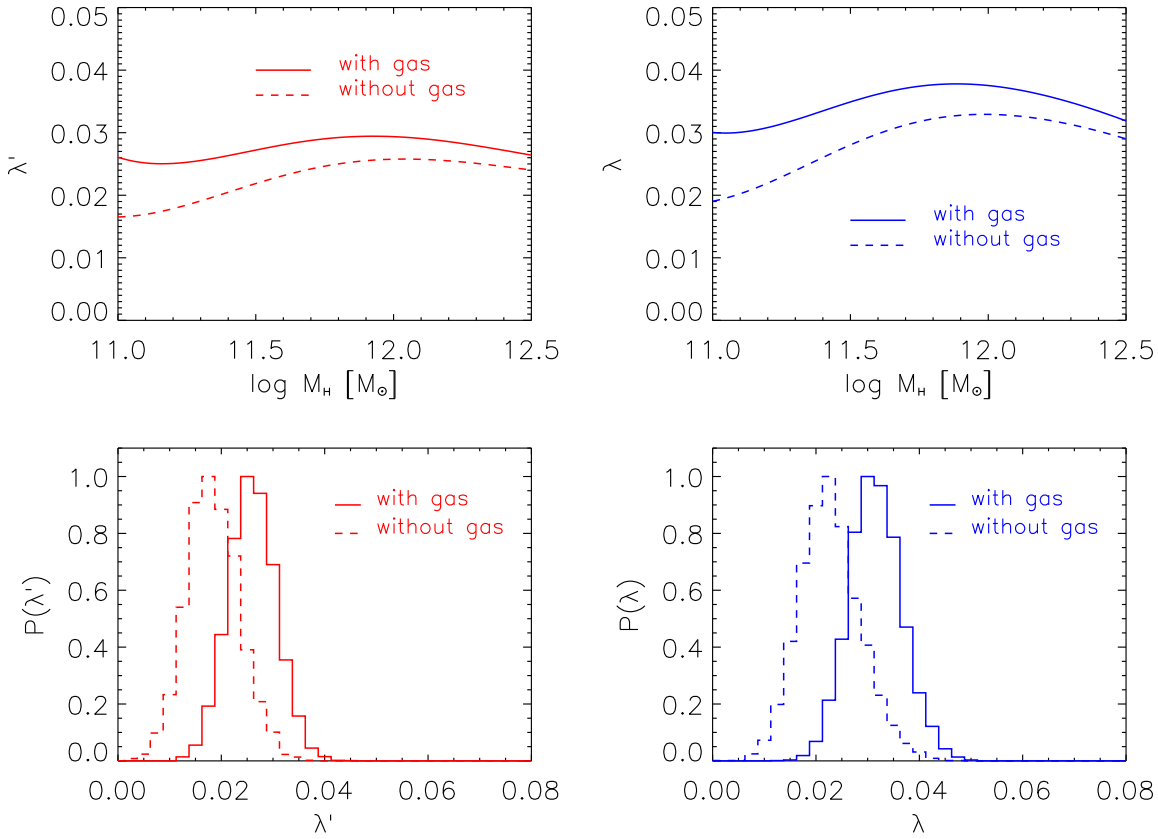

Figure 2.5 The spin parameter and its distribution function. *Top* panels: λ' (*left*) and λ (*right*) as a function of the halo mass, when the gas component is included in the system (*solid line*) and when it is not (*dashed line*). *Bottom* panels: the distribution function of λ' (*left*) and λ (*right*), again with gas and without gas.

large number of masses distributed according to $\Psi(M_H)$, computing then λ and λ' for each of them using Eqs. (2.20) and (2.21), and I eventually built up the statistical distributions. During this procedure I convolved the relations (2.20) and (2.21) with a gaussian scatter of 0.15 dex that takes into account the statistical uncertainties in the empirical scaling laws adopted in this work; these are mostly due to the determination of R_D through Eq. (2.4), for which I obtained the scatter by using the disk mass estimates of individual spirals [134].

As shown in Fig. (2.5) (*bottom panels*), I find a distribution peaked around a value of about 0.03 for λ and about 0.025 for λ', in the case when the gas is considered. This value of λ' is close to the result of the simulations by [53], who on average find $\lambda' = 0.023$ for spirals quietly evolving (i.e., experiencing no major mergers) since $z \approx 3$, see their Figure 4. In addition, [27] argue that this value of λ' provides a very good fit to the observed relation between the disk scale-length and the maximum rotation velocity (see their Figure 1). Moreover, the peak value of λ is in agreement with the results by [71], [192] and [131], who find a distribution centered around 0.03 for halos that evolved mainly through smooth accretion.

In addition, notice the effect of the gas contribution on the peak of the distribution; if it is not taken into account, the values of the halos' angular momenta are underestimated, and the offset with simulations is even more striking.

2.4 Discussion and Conclusions

The spin parameter distribution functions obtained from numerical simulations based on the ΛCDM framework performed by various authors ([25],[53] and references therein), show peak values of $\lambda' \geq 0.035$ for the whole halo catalogue, significantly higher than our empirical value. However, [53] highlight the fact that, considering only halos that have not experienced major mergers during the late stages of their evolution ($z \lesssim 3$), the average spin parameter λ' turns out to be around 0.023, very close to our observational result (see Fig. 2.6). Moreover, [71] and [131] showed that the spin parameter λ undergoes different evolutions in halos that have grown up mainly through major mergers or smooth accretion: in the former case λ takes on values around 0.044, while in the latter case λ has lower values around 0.03.

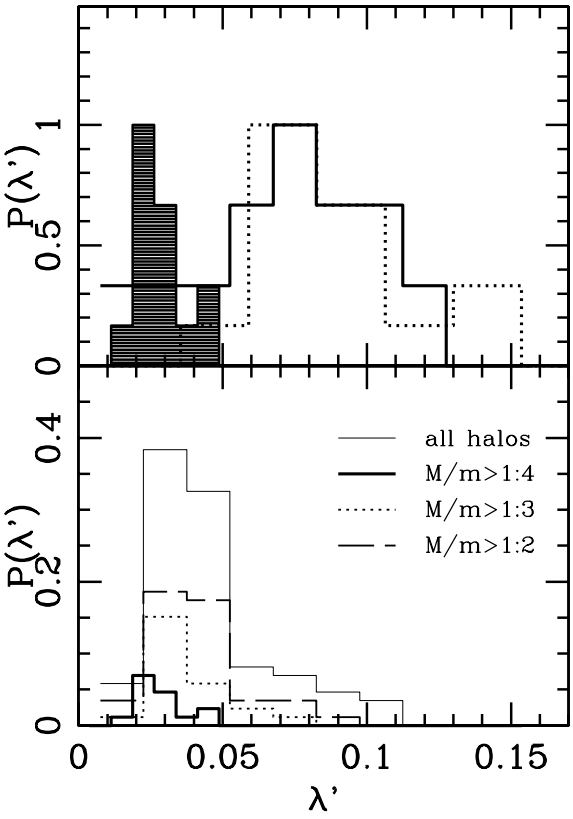

Figure 2.6 *Top panel*: the spin parameter distribution function as found by [53], for halos that did not experience any major merger since z=3 (*dashed region*). *Bottom panel*: the spin parameter distribution function of the entire halo population (thin solid line). Sub-populations are also plotted if one assumes that the definition of a major mergers requires mass ratios of $> 1:4$, $> 1:3$, and $> 1:2$, respectively, since z=3.

The results presented in this Chapter have therefore a precise physical meaning; the empirical determination of the spin parameter distribution function, on the basis of the observed geometry and relative mass distribution of the dark and luminous components, shows that spiral galaxies are hosted in halos characterized by a relatively poor history of major merging events, that grow mainly through quiet accretion from $z \simeq 3$.

Moreover, the distribution is quite tight, reflecting the very weak dependence of the spin parameter on the halo mass, as pointed out in the previous Section; this excludes significant frequent events of disk-disk collisions and gravitational fly-bys in the majority of the spiral systems, because they would introduce a large scatter in the values of λ and λ' due to the high number of different final states produced.

This scenario is not inconsistent with the hierarchical picture of structure formation, but challenges the proposed mechanisms for the formation of spirals, based on major mergings up to recent times ($z \leq 1$) [166].

Another feature of these distribution functions strikes as impressive: the absolute value of λ and λ' is quite small. On average, the degree of ordinate global rotational motions inside DM halos is around 3%. By comparing these values with the disk's $\lambda \simeq 0.4$ ([198]; it corresponds to $V_{rot}/V_c = 1$), and supposing that at the early stages of the baryonic cooling the luminous and dark components share the same phase-space region (a case consistent with the specific angular momentum conservation scenario), it is clear that the formation of the galaxy inside the DM halo happens with a significant transfer of angular momentum towards the central regions of the system, as the baryons carry their angular momentum with them during their collapse.

In a spiral galaxy, the collapse happens preferentially along one direction, taken as the spin axis z, so that it is a good aproximation to suppose that the specific j_z along this direction is conserved. This is the reason why the disk angular momentum is a good proxy (through a scaling) to the halo angular momentum.

However, the total angular momentum L^2 of the baryonic component is not constrained to be conserved during the collapse, and in fact, as will be discussed in Chapter 5, it is plausible that a fraction of the baryonic total angular momentum, while carried towards the center of the halo, is lost to the DM via processes like dynamical friction.

Chapter 3

Breaking the self-similarity

I present an observational counterpart to the NFW to model the mass distribution of systems of disk galaxies embedded in dark matter halos. The model is based on the observational scalings between the dark and luminous components discussed in Chapter 2, and produces a one-parameter family of curves that can be used to fit the observed rotation curves of spirals. The validity of the model resides in its being observation-based and therefore reliable in reproducing real systems; it shows that dark matter halos hosting spirals are not self-similar, and that the shape of their mass distribution features strong trends with the galactic mass.

3.1 Introduction

Numerical simulations of the hierarchical clustering predict the equilibrium density profile of DM halos to be described by the one-parameter NFW family of curves, that features self-similarity on the whole mass spectrum:

$$\rho_H(r) = \frac{M_{vir}}{4\pi R_{vir}^3} \frac{c^2\, g(c)}{x\,(1+cx)^2} \ , \tag{3.1}$$

where $x \equiv r/R_{vir}$ is the radial coordinate, M_{vir} and R_{vir} are the virial mass and radius, c is the concentration parameter $c \approx 9.5(M_{vir}/10^{12}M_{\odot})^{-0.13}$, and $g(c) = [\ln(1+c) - c/(1+c)]^{-1}$ (see Chapter 1 for a more detailed description). The corresponding velocity features the same self-similarity:

$$V^2_{\rm NFW}(r) = V^2_{vir} \frac{c}{g(c)} \frac{g(x)}{x} \ , \tag{3.2}$$

with $V_{vir}^2 = GM_{vir}/R_{vir}$. The total circular velocity of a system made of a disk galaxy embedded in a DM halo, build through the Mo et al. [107] model described in Chapter 1, is predicted to be a *universal* function of radius.

On the other hand, observations of galaxy rotation curves, up to now still the most reliable and abundant source of data on the mass distribution of the DM in galaxies, are at odds with the theoretical predictions and show a shallower cusp-less profile (among them, [136],[181],[170], [196],[57],[73],[159],[74]), usually parameterised by the Burkert halo [26]. A number of studies cast doubts on the reliability of the mass modelling procedure and the data analysis of some galaxies ([181],[170], [179]), or propose different explanations for the discrepancy, like triaxiality effects [81]. The debate is still on, but the evidence for a cored, Burkert-like DM profile is getting stronger ([72],[73],[74],[47],[48]); [30] and [169] confirm the Burkert profile to be the one that most successfully reproduces the observed profiles of spirals, with an analysis of 2200 curves and 60 extended curves respectively (see also [203],[206]). Persic and collaborators [138] presented an empirical model called the Universal Rotation Curve (from now on URC_0), a family of two-parameters velocity profiles that reproduce most of the systems, with the exception of bulge-dominated spirals (Sa-type) and dwarves; the DM density profile is described by the Burkert halo, and the disk luminosity and scale-length are the free parameters discriminating different systems. Independent analysis by [145] and [146] of the same samples are in agreement with the URC_0 description; the predictions of the model have been tested by [37] and [188] on additional different samples.

The discrepancy between observations and simulations regarding the structure of DM halos may stem from the fact that we observe the luminous component to understand the dark one; if we combine this with the structural difficulties of Nbody-SPH codes to penetrate the finest processes of galaxy formation and baryonic collapse, and the limitations of observations due to the uncertainties and model-dependent assumptions, the picture does appear a bit confused.

Yet, aknowledging the problem leads half-way to the solution. What this Thesis proposes is based on a simple consideration; if when observing the baryons we don't recover what the theory predicts for DM halos, then the cause of the discrepancy may well reside

in the baryons themselves. In Chapter 2 I showed how the structural parameters of disk galaxies, as yielded by observations, lead to a different conclusion regarding the spin of DM halos with respect to the theoretical predictions. The same line of reasoning can be used to infer an observational counterpart to the NFW velocity profile, that features the same degree of universality even if it entirely relies on empirical laws. And again, this will show how, by taking the baryons into account, another feature of the theory fails to show up in real systems, namely the self-similarity of dark matter structures.

3.2 The rotation curves of spirals and the global properties of halos

To gain information about DM halos from the galactic observables, I need to overcome the difficulty of relating the baryonic structure, that dwells in the central regions of the system, to the whole equilibrium structure of the halo.

For such a purpose, rotation curves alone are not a reliable tool, since the most recent and extended ones barely reach radial distances of $\leq 30\%$ of the virial radius. In the case of the URC_0, the model suffered from three main limitations; (i) it strictly held in a region extended less than $\sim 5\%$ of the halo size; (ii) the velocity profile of the halo component was fine-tuned to reproduce the data in this small region, and was not suitable for extrapolation to larger radii, in regions of cosmological interest; (iii) the free parameters of the family of curves were the disk luminosity and scale-length, thus introducing uncertainties due to the need of assuming a mass-to-light ratio, dependent on star formation rate, stellar evolution and extinction models.

Here I present a model for the velocity profiles of spirals that is based entirely on dynamical observations, and is able to make predictions on the DM halo global structure. Such a model can be used as an observational counterpart to the theoretical scenarios as the NFW, to predict the structure of single halos as well as mass and spin distributions to be used in statistical studies. It yields a one-parameter family of curves, so as to be as general as the NFW and equally straightforward to use and while it reproduces the data coming from the local matter distribution in the inner parts of the halo, at the same time it

predicts the halo global properties, like virial mass and spin, given the galactic mass alone.

The model described in Chapter 2, based on the observed scaling relations between disk and halo, provides the tool to build a Universal Rotation Curve determined by the whole equilibrium structure of the DM halo, thus consistently extending it to the dynamical edge of the system.

Consider a Burkert halo hosting a spiral galaxy; the dark matter cumulative mass profile is described by Eq. (2.6), and the corresponding halo circular velocity profile is

$$V_H^2(r) = 6.4\ G\ \frac{\rho_0 R_0^3}{r}\Big\{ln\Big(1+\frac{r}{R_0}\Big) - \tan^{-1}\Big(\frac{r}{R_0}\Big) + \frac{1}{2}ln\Big[1+\Big(\frac{r}{R_0}\Big)^2\Big]\Big\}\ , \qquad (3.3)$$

with R_0 and ρ_0 being the core radius and density respectively. Provided that $R_0 \ll R_{vir}$, this converges to the NFW profile outside the core. The disk velocity profile is given by Eq. (2.11).

To completely determine the total velocity profile $V^2(r) = V_D^2(r) + V_H^2(r)$ as a function of one free parameter, I use the empirical scalings described in Chapter 2, and summarized in Fig. (2.2); namely, the halo mass - disk mass relation of Eq. (2.2), obtained through a study of the halo occupation statistics, the disk mass - disk scale-length relation of Eq. (2.4), compared between a number of different authors (see Chapter 2), the halo central density - disk scale-length relation of Eq. (2.7), determined by [152] from a sample of extended rotation curves (up to $\sim 15\%$ of R_{vir}), and finally the halo mass - core radius relation, derived by inserting the above equations into

$$M_H(R_{vir}) = M_{vir}\ , \qquad (3.4)$$

to extract R_0 for any given halo mass (see Eq. 2.9). The present derivation of R_0 is very solid; in fact, errors up to a factor of 2 in the mass determination lead to an uncertainty in R_0 of less than 40%, while errors in the outer halo velocity slope in any case do not affect it by more that $\sim 10\%$. In comparison, the pure determination of R_0 in the URC_0 obtained by fitting the central velocity profile ($r \leq 0.05 R_{vir}$), was subject to large uncertainties, namely $\delta R_0/R_0 \sim 0.3-0.5$. In addition, the core radius obtained from global scalings works equally well in reproducing the single inner rotation curves, than its counterpart defined only by the inner kinematics, as is shown in Fig. (3.1); the solid line represents the ρ_0-r_0 relation as

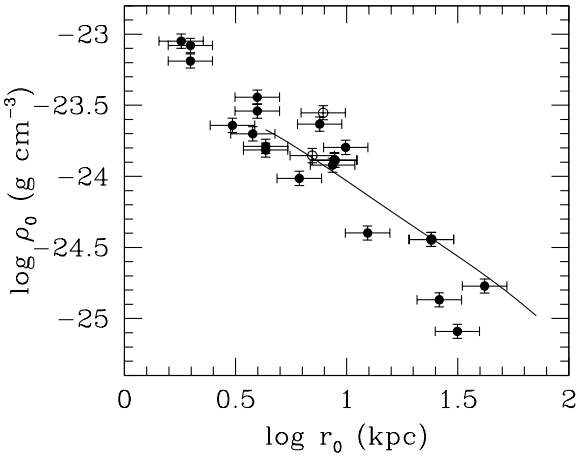

Figure 3.1 The core radius *vs* virial mass relations obtained in the present work (*solid line*), compared with fitted values from single curves (*dots*, see text for references).

obtained from the current model, while the dots represent fitted values from single curves extending to a maximum radius of $5-15\%$ of the virial radius ([57],[72],[153]).

The velocity profile thus obtained is a one-parameter family of curves, extended to the halo virial radius, and is determined by the whole halo equilibrium structure (instead of being fitted to match the central $\sim 5\%$ of the profile). Being the free parameter the galactic mass, it does not suffer from the model-dependent uncertainties that affected the URC_0, and makes the URC directly comparable with the results of numerical simulations. Further improvement is brought about by the newer and more complete sample of data for the determination of the scalings used in Chapter 2 (in particular, curves reaching out to several disk scale-lengths, see [152]), with respect to [138].

Given the galactic mass (or the halo mass, or disk scale-length), the halo structural parameters are determined, and the model yields the circular velocity at any radius, with an error that is an order of magnitude smaller than the variations occurring among different radii and different galactic masses (see Appendix A for a complete description of the mass modelling uncertainties). Therefore, given the observation of the inner rotation curve of

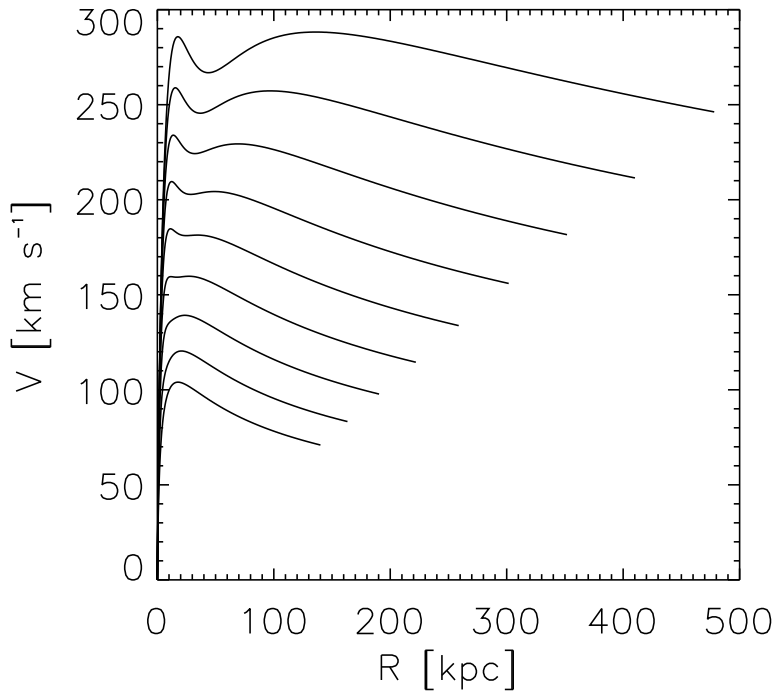

Figure 3.2 The Universal Rotation Curve in physical units. Each curve corresponds to $M_{vir} = 10^{11}\ 10^{n/5}\mathrm{M}_{\odot}$, with $n = 1 \ldots 9$ from the lowest to the highest curve.

a disk galaxy, the URC can be practically used to determine the global disk and halo structural parameters, with no degeneracy.

3.3 Results and discussion

In Fig. (3.2) I show the URC in physical units, in the halo mass range $10^{11}\,\mathrm{M}_{\odot} \lesssim \mathrm{M}_{\mathrm{vir}} \lesssim 10^{13}\,\mathrm{M}_{\odot}$; the amplitude of the curve is obviously determined by the halo mass, but the latter seems to affect the shape as well, contrary to any claim of self-similarity across the mass spectrum. I'll be back on this issue with the next plots.

In the meantime, notice the contribution of the baryonic component, negligible for small masses but increasingly important in the larger structures, that mirrors the behavior of the $M_{vir} - M_D$ relation. The baryonic peak becomes visible in the curve for systems with

$M_{vir} \sim 10^{12} M_{odot}$, while for lower masses the inner curve is DM-dominated down to the center. For increasing galactocentric distances, the halo eventually becomes the dominant mass component in all systems, but it does so at different radii according to the virial mass: from $\sim 10^{-2} R_{vir}$ for the smallest objects, to $\sim 10^{-1} R_{vir}$ for the massive ones. Remarkably, the maximum value of the circular velocity occurs at about 15 ± 3 kpc, independent of the galaxy mass, but due to different components: this seems to be a main dynamical imprint of the DM - luminous mass interaction occurring in spirals.

Furthermore, Fig. (3.2) shows that the "Cosmic Conspiracy" paradigm has no observational support: there is no fine-tuning between the dark and the stellar structural parameters to produce the same particular velocity profile in all objects (e.g. a flat one). Conversely, the scalings between the parameters produce a variety of profiles. Moreover, the peak velocity of the stellar component $V_{disk}^{peak} = V_D(2.2R_D) = GM_D/R_D\ k$, with $k = const$, is not a constant fraction of the virial velocity as is found in ellipticals, (i.e $\sigma \propto V_{vir}$), but it ranges between the values 1 and 2 depending on the halo mass.

Notice how the URC profiles are found to be (moderately) decreasing over most of the halo radial extent; the available kinematical data ([138],[152], [153],[57],[72]) show that both at the last measured point (between 5 and 15% of the virial radius) and at $r \sim 3R_D$, the velocity $V(r)$ is significantly higher than V_{vir} (of about $10 - 30\%$). The same behaviour is found with the NFW and Burkert profiles, showing that the assumption of flat rotation curves, often adopted to simplify calculations no matter the density profile, is not observationally supported, even as an asymptotic behavior at large radii.

In Fig. (3.3) I plotted the inner velocity profile, in the radial range including the luminous regions of spirals, normalized at a radius $r/R_D = 4$. There is an inverse correlation between the average steepness of the profile slope and the halo mass, due manly to the $M_{vir} - M_D$ relation; this is similar to the slope-luminosity relationship found by [133].

In Fig. (3.4) I show the same curves from a DM perspective, normalizing the velocities to V_{vir} and the radii to R_{vir}, comparing them with a pure NFW profile (*black line*). Although the URC is a one-family of curves, there is a remarkable, strong mass-dependent systematics: clearly, this curves are not self-similar.

There is a duplice source for the non-similarity. On the one hand, the scalings

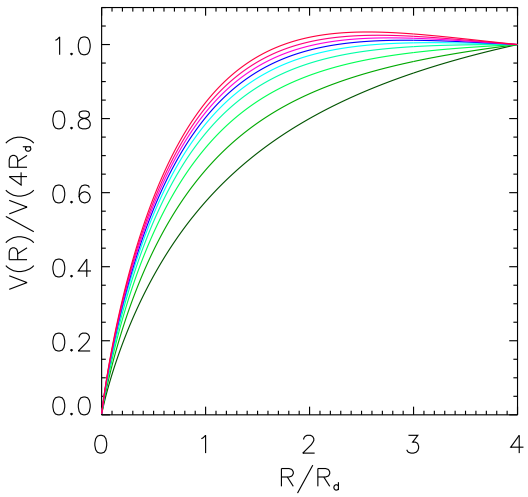

Figure 3.3 The inner URC, normalized at its value at $4R_D$, as a function of r/R_D. The single curves correspond to the same masses of Fig. (3.2), with the lowest curve representing the lowest mass.

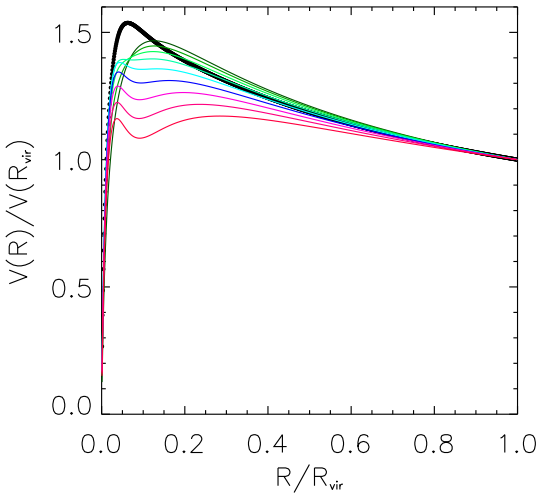

Figure 3.4 The URC normalized at its virial value V_{vir}, as a function of $x = R/R_{vir}$. The single curves correspond to the same masses of Fig. (3.2), with the lowest curve representing the highest mass. The solid black line is a pure NFW.

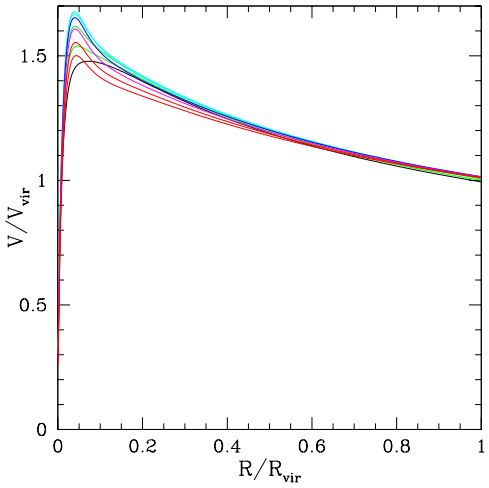

Figure 3.5 The same set of curves of Fig. (3.4), but with the NFW density profile substituting the Burkert; notice the amplitude of the "baryonic break" of the self-similarity.

between the baryons and the DM adopted in this model are not linear functions of the mass; the mass-to-light ratio is not constant on the mass spectrum, nor is the disk scale length-to-virial radius ratio, and in general terms the baryonic mass distribution strongly depends on the total mass, leading to a "baryonic break" of the self-similarity. To quantify this effect, I plot in Figure (3.5) the rotation curves of galaxies of the same masses as in Fig. (3.4), after substituting their observed Burkert halos with the theoretical, self-similar NFWs (with the same normalization), so that the offsets between the curves depend only on the different baryonic distributions according to the empirical scalings.

On the other hand, a comparison between Figs. (3.4) and (3.5) shows that in the observed systems, where the halo is better represented by the Burkert profile, the baryons alone cannot account for the differences in shape and amplitude between curves of different masses; rather, this is an evidence of a "DM break" of the self-similarity, with the halo mass distributon that changes depending on the galactic or virial mass, as shown also in Fig. (3.2).

Given the empirical base of the model, observations remarkably show that galaxies of different masses reside in halos of different shapes, with the luminous and dark components linked through smooth monothonic scalings. The amplitude of the "DM break" of

the self similarity is significant but small compared to the amplitude of the whole rotation curve, and it manifests itself as a perturbation of the central halo equilibrium structure, as a function of the disk mass; this strongly hints to a halo reaction to the baryonic presence.

An underlying physical mechanism that, most likely during galaxy formation, may affect the equilibrium structure of both components, luminous and dark, which react to each other and readjust their mass distribution (see Chapter 5), could be a way out of an old debate. The NFW halo is the final equilibrium state of DM structures in numerical simulations, but is not the preferred profile yielded by observations; in Figure (3.5) it looks quite static, equally unaltered by the presence of baryons, even in a wide range of disk masses. The gap between Figs. (3.4) and (3.5) could be of an evolutionary nature; the primeval NFW halo, dominated entirely by DM dynamics at early stages, is perturbed by galaxy formation, to an amount depending on the size and mass of the galaxy itself, and changes its equilibrium structure into a cored configuration.

Chapter 4

The dark matter distribution at the edge of spirals

I present some evidence that the discrepancy between observations and numerical simulations regarding the shape of the mass distribution in dark matter halos extends to the whole region where the luminous component is present, with the observed density profile not converging to the NFW even outside the halo core. This indicates that such discrepancy cannot be due to numerical effects or pure microscopic physics; the observed excess of mass around $5-30\%$ of the virial radius hints to a mechanism of mass redistribution, probably occurring during the disk formation, that offsets the density profile in the whole central region of the dark matter halo.

4.1 Introduction

The CDM halo structure, as predicted by numerical simulations, has not yet found a physical explanation ([173],[198]). The phase-space structure of the NFW halo looks like an attractor for hierarchical clustering in different cosmogonies [198], and the self-similarity and the intrinsic simplicity of its shape make for a very attractive picture of structure formation, that is particularly successful in reproducing the observed large-scale structure and the objects at cluster scales, and fails to reproduce galaxy-size systems.

As discussed in Chapter 1, the invariance of the predicted halo structure at all scales, together with the solidity of the final density profile against different initial conditions like the details of the power spectrum or the cosmological parameters, points towards a universal mechanism of assembly characterised by processes like violent relaxation, that erase the memory of the initial state of the system prior to each main accretion event, and makes the final structure converge towards the NFW [198].

It is not clear to what amount the numerical treatment is responsible for this formation pattern. An example is the cusp feature, that may be a spurious product of an intrinsic deficiency of simulations in treating small-scale gravitational interactions. Mixing processes are not scale-invariant, and there are fundamental differences in the behaviour of a system after coarse-graining; the numerical approach is not suitable to address such issues, almost by definition, and the entity of the unavoidable approximation in representing such mechanisms is unknown. These effects must manifest themselves at small scales, and it is not a cohincidence that the claimed discrepancies between simulations and observations mainly regard the inner halo structure and the amount of substructures.

However, in this Chapter I present recent observational evidence that the cusp-core discrepancy is just part of a more serious and general offset betweent the CDM predicted profiles and the observed ones, at least in some galaxies (as suggested by [104]). The state-of-the-art high quality rotation curves of spirals are extended out to several disk scale-lengths, and allow to probe regions that previously were observationally off-limits; for these systems, the density profile does not converge to the NFW even outside the halo core, but shows an interesting excess of mass around $5-6\ R_D$, corresponding to $5-30\%$ of the virial radius [75]. It is fundamental to notice that these galactocentric distances represent scales large enough to be unaffected by numerical effects, or by the smoothing of the cusp due to self-interacting or warm DM (see [41] for instance).

As will be extensively discussed in Chapter 5, I don't believe these observations are in conflict with the hierarchical paradigm, nor do they prove that the simulation process is severely inaccurate, but rather, they highlight a lack of a proper physical description of some of the mechanisms accompanying galaxy formation inside the halos. In the specific case, the baryonic collapse and the subsequent formation of the galaxy represent a major

perturbation in the halo structure; given the hierarchical clustering scenario leading to the NFW halo, the new observations of galactic dynamics are consistent with a halo response to galaxy formation causing the evolution of its equilibrium structure.

4.2 The evidence of a discrepancy outside the core

In this Section I will analyze the data coming from two spirals' samples spanning 3 orders of magnitude in disk mass, namely: i) the sample of high-quality rotation curves selected by [57], discarding the 4 galaxies with the smallest extension relative to the disk exponential scale length R_D; ii) a sample selected from the literature with a criterium based on the extension of the rotation curve, *i.e.* either the last measured point is at a radius larger than a fixed distance (chosen as $r > 6R_D$ or $r > 30$ kpc), or the velocity at the last measured point is higher than a threshold (chosen to be 250 $km\ s^{-1}$). These conditions ensure that each curve is extended enough to map regions of the system where the baryons are markedly sub-dominant, so that the velocity profile is regulated by the dark matter distribution; moreover, these regions are distant enough from the center of the halo not to be affected by the particular shape of the inner profile. As an additional measure of precaution, only galaxies with curves regular out to the last data point are considered. In addition to these two samples of galaxies, I will consider two particular spirals, namely DDO 47 ([153],[73]) and ESO 287-G13 [72], due to the exceptional quality of their observed curves (H_α and HI respectively). For all the 37 galaxies considered, the rotation curves reach maximum galactocentric distances between $\sim 5\%$ and $\sim 35\%$ (NGC 9133) of the virial radius, with an average outermost radius of 24 kpc. In Table (1) I list the galaxies of sample (ii), marking with "$*$" those whose mass decomposition was provided in the reference. For those unmarked, the mass decomposition was obtained following [135].

The mass modelling of the rotation curves of these samples of galaxies yields cored DM density profiles as best fits ([153],[73],[72]); however, I'm interested in the outer regions of the disk, to check whether the discrepancy extends to the whole DM profile. I found out these halos do not converge to NFW profiles anywhere; moreover, they show an interesting trend in their mass distribution.

Table 4.1. Sample (ii) with references.

Galaxy	Reference
NGC 289*	Walsh et al., 1997
NGC 1068	Sofue et al., 1999
NGC 1097	Sofue et al., 1999
NGC 1232*	van Zee & Bryant, 1999
NGC 3198*	Blais-Ouellette et al., 2001
NGC 3726	Verheijen & Sancisi, 2001
NGC 4123*	Weiner et al., 2001
NGC 5055	Sofue et al., 1999
NGC 5236	Sofue et al., 1999
UGC 5253	Noordermeer et al., 2004
NGC 5985	Blais-Ouellette et al., 2004
NGC 6946*	Carignan et al., 1990
NGC 7331*	Bottema, 1999
UGC 9133*	Noordermeer et al., 2004

Note. — Selected galaxies with their references. The asterisk indicates that the original work provided also the dark-luminous decomposition of the rotation curve.

In order to compare the observed density profile of these galaxies, represented by the Burkert model, with an NFW halo, there are different possible choices. Due to the poor performance of the NFW profile in fitting these curves, instead of adopting the minimum χ^2 criterium, I impose a more physical condition; the chosen NFW model must yield the observed total mass at the last measured point, thus satisfying the condition

$$M_{\rm NFW}(r_{\rm f}) = M(r_{\rm f}) \ . \tag{4.1}$$

Notice that, if the observed density profile indeed converged to an NFW, this equality would hold for all radii outside the cusp/core, including the last measured point (the contribution of the cusp to the total mass is negligible). On the contrary, if Eq. (4.1) is true *only* for some radius smaller than r_f, then the two profiles are significantly discrepant from that point outwards. In the case the equality holds for radii larger than r_f, the two profiles are indeed completely different in all the radial range considered.

Fig. (4.1) shows the result of this comparison for DDO 47 and ESO 287-G13, for which I find NFW halos of concentration and virial mass of $c = 18.4,\ M_{vir} = 6\times10^{10}M_{\odot}$ and $c = 13.3,\ M_{vir} = 7 \times 10^{11}M_{\odot}$ respectively. The dots represent the best-fit Burkert profile, and the errorbars mirror the uncertainties in the fitting parameters ([153],[72],[73]), which are larger in the inner parts, due to the difficulties of the mass decomposition. The solid lines represent the best NFW profiles, chosen according to Eq. (4.1). For ESO 287-G13, the dashed line is the best NFW determined with a slightly different mass modelling, with halo + disk + gas components [72], and M_{vir} and M_D/M_{vir} as free parameters. Fig. (4.1) highlights a discrepancy between the NFW and the observed profile that goes beyond the cusp/core issue: the observed profile does not converge to the NFW anywhere. In the outer parts, the measured density is higher than the NFW, and the slope of the profile is shallower. Notice that such a discrepancy was already present in some previous investigations (e.g. [11],[16],[46]), although it was not claimed explicitly.

Another viable method to compare the observed dark matter mass distributions with the NFW profile is to impose that, at the last measured point of the rotation curve, the densities coincide:

$$\rho_{\rm NFW}(r_f) = \rho(r_f) \ , \tag{4.2}$$

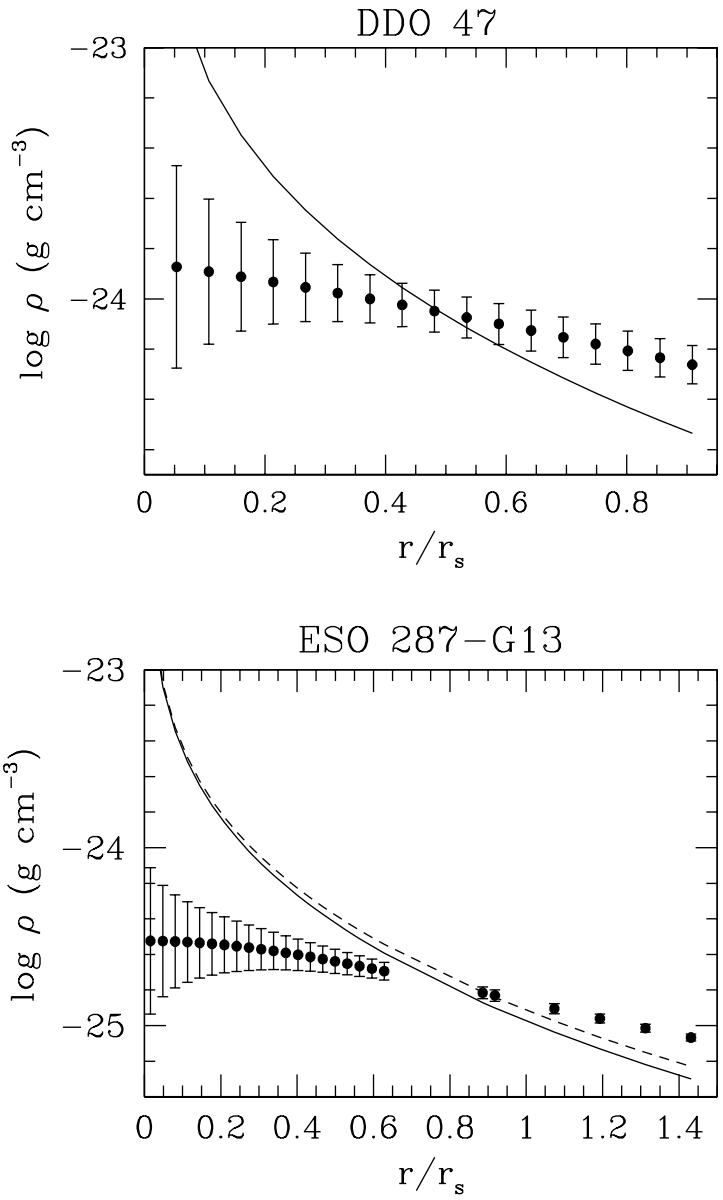

Figure 4.1 *Dots*: DM density profiles for DDO 47 and ESO 287-G13, as yielded by the best fits (Burkert halo) in the original papers (*dots*; [153],[72],[73]). *Solid lines*: NFW density profile such that $M_{NFW}(r_f) = M(r_f)$ (see text). *Dashed line*: best-fit NFW for ESO 287-G13.

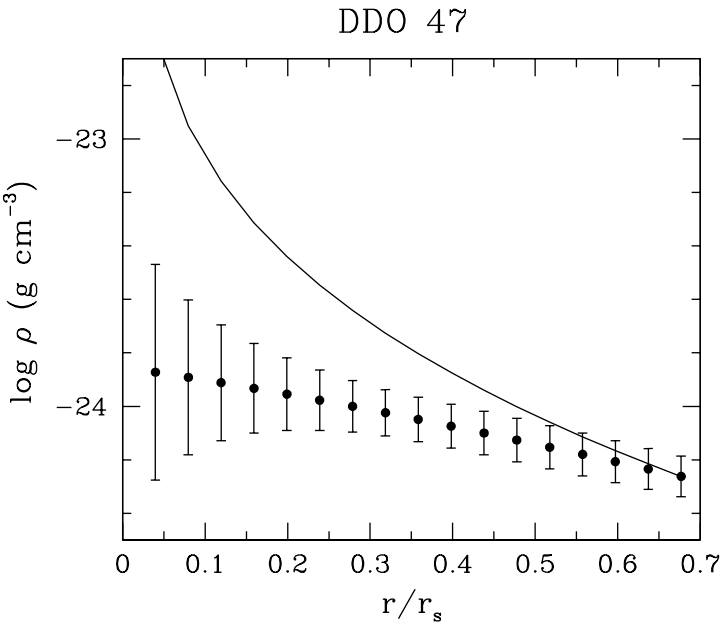

Figure 4.2 Density profile of DDO 47 assuming $\rho_{\rm NFW}(r_{\rm f}) = \rho(r_{\rm f})$ (*solid line*), compared to the data (*dots, as in Fig. (4.1)*).

as illustrated in Fig. (4.2) for DDO 47. In this case, the NFW is well above the observed profile anywhere inside the last point, showing an even wider discrepancy.

No matter the normalization, from these plots it is evident that the observed density profiles of these two galaxies do not converge to an NFW; moreover, the NFW is steeper everywhere. The measured mass distributions show an inner density deficit, and an excess of mass in the outer regions, when compared to the theoretical expectations; this may happen for a number of reasons, the first being the possibility that these halos are not in equilibrium.

To address this issue, I analyse the whole sample of galaxies, checking whether their outer mass distribution converges to an NFW. In order to do this, I take advantage of the fact that the NFW is a one-parameter family of curves, and exploit the radial dependence of mass and density to build a curve $M(\rho, r)$; as it turns out, an aproximation is given by

$$M(\rho, r) \simeq \rho(r)^{3/4}\ r^{11/4}\ . \tag{4.3}$$

Notice that this simply reflects a relation of the kind $M \sim \rho\, r^3$, corrected by a shape factor

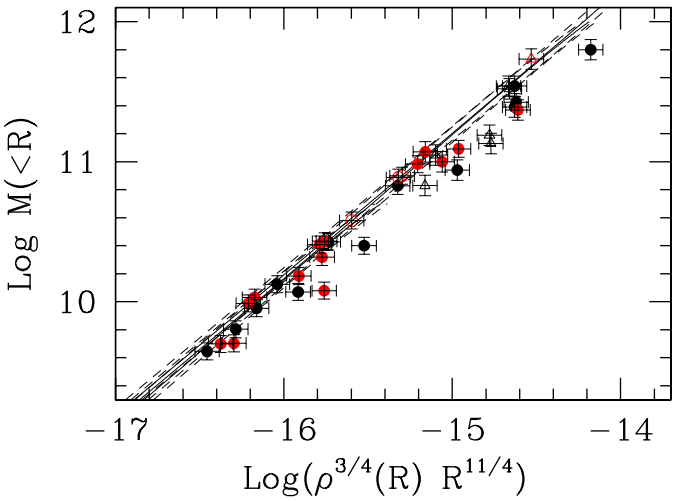

Figure 4.3 The $M - R - \rho$ relation: the *solid lines* represent NFW halos of virial masses $5 \times 10^{10}\ M_\odot$, $1 \times 10^{12}\ M_\odot$ and $1 \times 10^{13}\ M_\odot$. The dashed lines enclose the 1σ regions for the determination of c (see [194]). The radial range for all the halos is between 1% and 20% of the virial radius. The *dots* represent the galaxies of the samples described in the text, at the last measured point. The three edge-on galaxies are denoted by *empty circles*. *Empty triangles* denote the objects of sample (ii) for which we computed the mass decomposition. Red symbols are isolated halos and black symbols are subhalos.

accounting for the deviation of the NFW density profile from a uniform sphere. As expected, for a given halo the plot is a straight line with slope around 1. However, the self-similarity of the NFW halo endows the nice property that the *same* straight line is followed by *all* halos, regardless of the virial mass; this mirrors the phase-space stratification during the mass accretion of the halos in hierarchical clustering. This is shown in Fig. (4.3), where I plotted 3 halos of masses $5 \times 10^{10}\ M_\odot$, $1 \times 10^{12}\ M_\odot$ and $1 \times 10^{13}\ M_\odot$. The scatter among the lines is due to the uncertainties in the determination of the concentration c as a function of the virial mass.

I then compare this theoretical prediction with the observed properties of the galaxies in the samples cited above. For each galaxy, I compute the mass enclosed inside the last measured point, and the density at that point. Notice that the mass $M(< r)$ is mainly affected by the DM matter distribution near r, while the presence of a cusp/core in

the centre (as well as a baryonic component) is totally marginal.

For these galaxies, the NFW is not the best-fitting profile, so I do not expect them to sit on this relation. However, they do show an interesting pattern: all the galaxies are sistematically offset on the same side of the curve, and in particular, at a given last radius and enclosed mass, the density is always higher than in the NFW case, up to a factor of ~ 3. This is the equivalent of what was shown in Fig. (4.1), and the conclusion is the same: in the majority of these galaxies, the DM density profile around $5-6$ disk scale-lengths shows an excess of mass enclosed in this region, compared to the NFW.

Conversely, this plot can be read the other way around; if at a certain radius r the density profile is described by the NFW, then the mass inside that radius would be higher than observed, and this is the case represented in Fig. (4.2), with an even larger overall discrepancy between the theoretical and observed profiles (see for comparison [156], with a case where, in order to fit two observed galaxies with an NFW profile and to match the outer mass distribution, the inner rotation curve is significantly overestimated). Again in this case, all the galaxies are offset on the same side of the theoretical curve. This result excludes the possibility that non-equilibrium effects are responsible for this discrepancy.

The mean offset of $\sim$0.1 dex is solid (but note that larger offsets are also observed); in fact, the error propagation analysis shows that the 3% error in the measure of the circular velocity and the 0.05 error in the logarithmic gradient $d\log V(R)/d\log R$ yield uncertainties of the order of 0.025 dex in M and 0.06 dex in ρ. The errors in the objects distances are not included since they only induce random uncertainties.

It is interesting to see whether the environment has an effect on our results: I distinguished between galaxies in "isolated" halos and galaxies in "subhalos" (for details, see [154]). Qualitatively there are no obvious trends between the two subsamples, although the result is consistent with the predictions of [25] regarding the difference between the concentrations of halos and subhalos.

Three of the galaxies in the samples were edge-on ($i > 85°$); the HI rotation curves in these cases may suffer from unaccounted-for projection effects, while the Hα curves may be plagued by extinction [19]. However, they do not seem to occupy any peculiar region of the plot, nor to be any more offset than the other galaxies.

Finally, the galaxies from sample (ii) for which the mass modelling was not provided in the literature, and that were mass-decomposed following [135], do not show any special trend with respect to the others, indicating that the particular method for fitting the rotation curve does not significanlty affect the result.

In the present analysis, spurious dynamical effects such as warps and non-circular motions can bias the determination of the mass distribution. In fact, actual CDM halos are expected to be triaxial, which may induce non-circular motions in the gas [81]; in addition, gas moving along filaments [51] may interact with the galaxies, triggering the formation of warp-like features in the disks. Nearly all the rotation curves collected in the present work were derived using the tilted-ring fitting of the velocity field, which can account for warps but not for non-circular motions. The exception is DDO 47, which was studied in detail by [73] using the harmonic decomposition of the velocity field [205]. In summary, only the effects of warps are taken into account; however, non-circular motions are expected to produce only random scatter in the observations, without any systematic effect.

4.3 Discussion

The observed rotation curves were fitted with the Burkert profile, exploiting the empirical relation found in [152], linking the core radius and density (which is consistent with the URC model in the halo's inner regions, as shown in Chapter 3). The virial masses were computed by integrating the density profile until the mean density was Δ_{vir} times $\rho_{\rm c}$ (see Chapter 1). In Fig. (4.4) I plot the observed galaxies against a relation between the Burkert mass, density and radial distance that is equivalent to the one described by Eq. (4.3), finding the expected random scatter around the curve. This Figure highlights the main difference between the density profile inferred from observations and the NFW; the Burkert profile is not self-similar, and in fact halos of different virial masses do not sit on the same straight line, due to the marked mass-dependency of the Burkert shape factor. In addition, the different position of the overall relation in the plot with respect to the NFW, highlights again that the two profiles are significantly different at the edge of the disk, in the regions investigated by this dynamical analysis ($\sim 5-30\%$ of the virial radius).

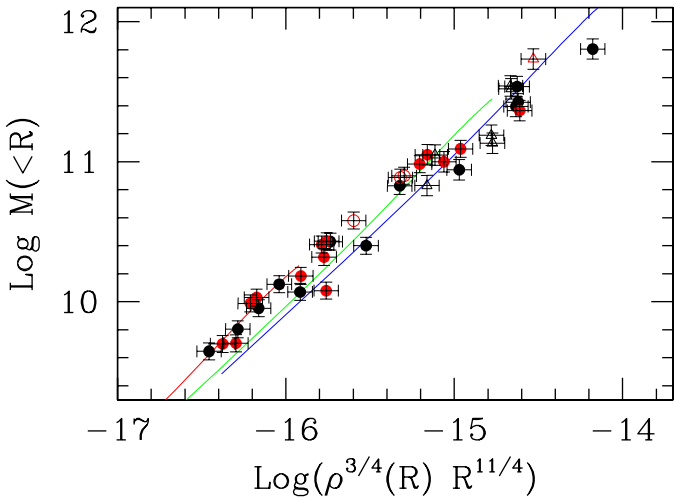

Figure 4.4 The same as Fig 4.3, but showing that Burkert halos predict a mass dependent $Mvs(\rho^a\ R^b)$ relation in good agreement with observations [152]. Symbols are the same as Fig 4.3, and the 3 lines correspond to 3 different virial masses (5×10^{10} M$_\odot$, 1×10^{12} M$_\odot$ and 1×10^{13} M$_\odot$.

There are hints in the literature of an observed convergence of the DM density profile to the NFW in regions more external than the ones analyzed here; [142] for instance investigated the DM profiles outside the optical radii of isolated galaxies ($r > 0.2-0.3\ R_{vir}$), by studying the kinematics of satellites. Similar conclusions were reached by ([20],[21]) for scales $\geq 50\ h^{-1}$ kpc, using weak galaxy lensing in addition to the dynamics of satellites; [191] and [207] show the agreement between X-ray data and NFW profiles in galaxy clusters.

Although the statistical significance of the results of this Chapter has to be improved with more data, so far in this Thesis the evidence presented indicates a trend for galactic halos to feature an inner mass distribution that is not universal, and does not resembre the one predicted by numerical simulations. In addition, this seems to apply to galaxies but not to more massive systems.

As already pointed out, the discrepancy is manifested at galactocentric distances too high for numerical effects to be significant. In addition, for the same reason such a discrepancy cannot be explained by effects due to self-interacting o annihilating DM, that would indeed erase the halo cusp but would yield a profile convergent with the NFW already

at small radii (see for instance [161],[1] and references therein).

If one wants to speculate about the physics beneath this puzzle, she may find herself wondering around the idea of baryons. The effects of baryons on DM halos, and in particular of baryonic collapse and galaxy formation, are poorly understood. So far, adiabatic contraction has been the only process extensively studied ([14],[79],[155]), and it is thought to increase the halo concentration after the formation of the galaxy. However, it is difficult to reconcile adiabatic contraction with the chaotic and random mass accretion process that characterizes hierarchical clustering. On the other hand, a few have studied mechanisms with opposite effects, like adiabatic expansion [58] or dynamical friction [177], that transfers angular momentum to the centre of the halo and mass to the regions outside the halo core. In addition, [156] show the failure of the NFW in fitting the mass profile of a barred galaxy, the concentration parameter of which has to be much smaller than the averaged predicted value; the authors discuss possible evidence of the absence of adiabatic contraction or alternatively of some dynamical effects that compensates for it.

Although baryons represent an almost negligible fraction of the halo mass, their collapse trasfers this mass and all the relative angular momentum to the inner halo, as discussed at the end of Chapter 2. From an initial state in which they are distributed following the DM, the system ends up in a state where the baryons completely dominate the center of the halo. Chapter 5 of this Thesis will deal with the evolution of the halo structure following a perturbation in its dynamical state, suggesting a kind of interaction, dynamical in nature, between the DM and the luminous component, that re-shapes its equilibrium configuration. Notice that, up to now, there is evidence of such a baryon-induced evolution only in galaxy-size halos, where the ratio between the luminous and dark mass is high enough, and the formation timescales short enough, to allow the baryonic collapse to significantly affect the final equilibrium structure of the system.

Chapter 5

Dynamics of dark matter halo evolution and galaxy formation

I present a theoretical model of the dynamics of the halo reaction after a perturbation of its equilibrium structure, highlighting the tight connection between the spatial mass distribution and the shape of the velocity dispersion tensor. An unbalance in the components of the internal velocities, arising from angular momentum injection into the halo, triggers a mass rearrangement and the evolution into a new equilibrium configuration; if the tangential motions dominate in the inner halo, the cusp is smoothed out into a corelike profile. I also present a physical model describing such a halo evolution; during the baryonic collapse leading to the formation of the protogalaxy, the gas clouds infalling towards the center of the halo experience dynamical friction with the background dark matter, locally transferring angular momentum to the halo and thus enhancing its tangential velocity dispersions. The amplitude of such a perturbation is big enough to unbalance the halo and cause structural evolution.

5.1 Introduction

So far, the evidence gathered in this Thesis can be summed up in three main points:

a- the DM mass distribution in galactic halos is not self-similar, but present strong

trends with the galactic mass;

b- the DM profile is not well fitted by the NFW in spirals, but features instead shallower central slopes and excesses of mass in the outskirts of the disk, that cannot be attributed to numerical effects or more exotic variants than the CDM;

c- the angular momentum measured in galactic halos strongly depends on the mass and distribution of the baryonic component, and is not correctly predicted by numerical simulations.

In brief, the observations of disk galaxies do not support the existence of a universal, self-similar equilibrium DM halo, as naturally arising from the patterns of hierarchical clustering; rather, they suggest a more complex scenario where the halo structure is determined by the global properties of both the dark matter and the baryonic components.

It is now the time to try and give some theoretical interpretation to these facts. The equilibrium structure of halos is tightly linked to the mechanism of halo formation, so one may think that doubting the NFW means to doubt the whole hierarchical clustering theory; to the contrary, my take is that the theory is correct, but there are some pieces of physics missing as far as galactic halos are concerned. The existence of determined scalings between the properties of the DM and the baryons in disks, and the fact that the discrepancy between observations and theoretical predictions regarding the structure of halos, manifest itself precisely where the baryonic component is present (see [57]), leads me to consider an evolutionary approach.

Suppose that a pristine, unperturbed DM halo, as emerging from the non-linear growth of perturbations in a hierarchical scenario, features a phase-space structure and mass distribution as predicted by the CDM theory. The mass distribution would be described by the NFW profile, the phase-space density would be a power-law of slope ~ 1.875, and the velocity anysotropy profile would be null in the centre and slighlty increasing in the outskirts (see Chapter 1 for reference).

Some billion years later, we observe a disk galaxy inside the halo, we recognize that its main features are probably related to the halo structure, and yet we find that the same structure is non consistent with the picture of a theoretical DM halo. This makes me wonder whether the baryons themselves could be at the origin of the disagreement.

As the galaxy formation is undoubtedly determined by the halo dynamical properties, could the baryon collapse and galaxy formation induce a perturbation big enough to trigger an evolution of the halo, in response to the changing equilibrium conditions of the whole system? And in particular, could such perturbation affect the dynamics and structure of the inner halo in such a way that the original NFW profile is flattened into a corelike structure?

When the baryonic component in the Universe decouples from radiation, early dark matter structures are already in place, hierarchically growing. The gravitational potential of the overdense regions attracts the baryons, and in the simplest scenario they settle into the wells in dynamical equilibrium with the dark matter. In other words, the phase-space structure of the two components is similar in these very early stages; the baryons share with the dark matter the mass and specific angular momentum distributions. However, in the densest regions the baryons are subject to a series of dissipative processes, namely the radiative cooling and the subsequent condensation, that lead to the formation of self-gravitating clouds, that may or may not contain dark matter. Because of the high concentration of the baryons at this stage, the clouds remain bound, and dynamically decouple from the background halo, whose mass distribution in comparison is relatively smooth (see Chapter 1 for references).

These baryonic substructures fall towards the centre of the halo under the effect of gravity; as a consequence, the fraction of the total angular momentum of the system shared by the baryons is carried to the center. The cloud orbits inside the halo potential well are determined by the cloud initial position and relative velocity (that in turn may depend on the large-scale dynamical conditions, like the overall velocity and density fields).

As the clouds fall into denser and denser regions, dynamical friction exerted by the background dark matter slows them down, with a net transfer of angular momentum locally from each cloud to the dark matter, thus enhancing the halo tangential random motions. The anisotropy profile, measuring the balance between radial and tangential velocities, governs the equilibrium mass distribution of the halo through the Jeans' equation; the predominance of tangential motions in the center of the halo moves the particles on orbits of higher energy and increases the entropy, with the result of partially unbounding the

system and triggering a mass transfer out of the cusp, flattening the density profile ([177]).

This Chapter is divided into two main parts. At first, I will give the mathematical description of the halo evolution under perturbations of the velocity anisotropy profile, and show in particular that an injection of random angular momentum flattens the inner density profile. Secondly, I will produce a physical model accounting for the dynamical coupling of the baryons to the dark matter through dynamical friction, and show that random angular momentum is transferred from the formers to the latter, with the right amplitude and distribution to trigger the described halo evolution.

5.2 The NFW distribution function

As already mentioned in Chapter 1, the microscopic dynamical properties of a collisionless system of particles, like a dark matter halo, are described in phase-space by its distribution function (DF), a 7−dimensional function of coordinates, velocities and time $f(\mathbf{x}, \mathbf{v}, t)$, that is the solution of the collisionless Boltzmann equation; as stated by the Jeans' theorem [10], f depends on the phase-space coordinates only through the integral of motions in the halo potential, thus defining the symmetries governing the system's evolution. It is not observable in itself, but its integrals yield the description of the macroscopic properties of the system; any macroscopic observable O is obtained by means of f through the average

$$\langle O \rangle = \int O\, f\, \mathrm{d}^3 v / \int f\, \mathrm{d}^3 v. \tag{5.1}$$

Thus, in particular, the mass distribution of a DM halo is linked to its microscopic dynamical properties through:

$$\rho(r) = \int f(r, v) \mathrm{d}^3 v \ , \tag{5.2}$$

at any particular time. In this Chapter I will assume that the halo evolves through a series of stationary states, thus discarding the explicit dependence of f on time.

In order to represent the NFW halo in phase-space, I need to find its distribution function. This is almost never a trivial task, even in the simplest of scenarios, and for the NFW the additional complication is that the process is not analytical.

I remind the reader of the characteristics of my adopted unperturbed equilibrium density profile:

$$\rho = \frac{M_H}{4\pi R_H^3} \frac{c^2\, g(c)}{x\,(1+cx)^2} \ , \tag{5.3}$$

where c is the concentration parameter, and $g(c) \equiv [\ln(1+c) - c/(1+c)]^{-1}$. From now on, all the physical quantities will be expressed in units of the virial mass M_H and radius R_H. The gravitational potential is obtained through the Poisson's equation

$$\nabla^2 \Phi(x) = 4\pi G \rho(x) \ , \tag{5.4}$$

and is expressed in terms of the virial velocity $V_H \equiv \sqrt{G\,M_H/R_H}$:

$$\Phi(x) = -V_H^2\, g(c)\, \frac{\ln(1+cx)}{x} \ . \tag{5.5}$$

In the simple case of a totally isotropic halo, f is explicitly a function of energy alone (both positions and velocities of the particles are defined by their energy), and its determination from the density profile is unique. By conventionally defining the relative potential and binding energy as $\Psi = -\phi$ and $\varepsilon = -E = \Psi - \frac{1}{2}v^2$ [98], the DF describing the equilibrium is obtained from the potential-density pair through the Eddington's inversion formula [10]

$$f(\varepsilon) = \frac{1}{\sqrt{8}\pi^2} \frac{d}{d\varepsilon} \int_0^\varepsilon \frac{d\rho}{d\Psi} \frac{d\Psi}{\sqrt{\varepsilon - \Psi}} \ . \tag{5.6}$$

However, the simulated halos show a nontrivial anisotropy profile; the degree of anisotropy is commonly expressed through the parameter

$$\beta(r) = 1 - \frac{\sigma_t^2}{\sigma_r^2}, \tag{5.7}$$

where σ_t^2 and σ_r^2 are the $1D$ tangential and radial velocity dispersion profiles respectively. In simulations the halos turn out to be isotropic in the center ($\beta = 0$), and radially anisotropic ($\beta > 0$) outwards ([33],[70]).

For anisotropic, spherically symmetric systems, f is an explicit function of two integrals of motions, commonly taken as the energy and the total angular momentum L^2 [10]. The quantity $\vec{L}(r) = \vec{r} \times \vec{v_T}$ is defined in terms of the tangential velocity $\vec{v_T}(r)$; this is the $2D$ vectorial sum, on spheres of radius r, of all the velocity dispersions orthogonal

to the radial direction. For this reason, $\vec{L}$ is not an angular momentum in the strict sense, as it does not define any preferential direction of rotation; rather, the quantity $L^2(r)$ is a measure of the tangential component of the internal, randomly-oriented motions of the halo, and for this reason I will from now on refer to it as the halo's *random angular momentum*.

With two explicit variables, there are infinite allowed DFs that satisfy Eq. (5.2). However, only some of the possible DFs correspond to equilibrium configurations of the system, or in other words, satisfy the Jeans' equation. A generalization of the Eddington's solution, for systems with generic anisotropy profiles, yields a DF of the form [39]:

$$f(Q, L^2) = f_0 \left(\varepsilon - \frac{L^2}{2r_a^2} \right) (L^2)^\alpha \ . \tag{5.8}$$

$f_0(Q)$ is an equilibrium DF describing systems characterized either by isotropy or by radial anisotropy, with r_a being the anisotropy radius, at which $\beta = 0$ ([120],[105],[10]); the orbital energy $L^2/2r_a^2$ associated with L lowers the particle binding energy, that becomes $Q = \varepsilon - L^2/2r_a^2$. To account for tangential anisotropy, a pure angular momentum component is given to the DF, taking the simple functional form of a power-law of index α.

This DF represents a very general family of equilibrium solutions of the Jeans' equation [39], for spherically symmetric systems with mass distribution and anisotropy profile depending on f_0, r_a and α. Systems described by this DF include the NFW (both in the isotropic and radially anisotropic realizations), and the cored profiles, as I will show in the next Section.

The spherically averaged density profile of a system described by a DF of the family of Eq. (5.8) can be recovered by transforming the coordinate system from (v_r, v_T) to (Q, L^2) in Eq. (5.2), yielding

$$\rho(r) = \frac{2\pi}{r^2} \int_0^\Psi f_0(Q) \mathrm{d}Q \int_0^{2r^2(\Psi - Q)/(1 + r^2/r_a^2)} \frac{(L^2)^\alpha \, \mathrm{d}L^2}{\sqrt{2(\Psi - Q) - (L^2/r^2)(1 + r^2/r_a^2)}} \tag{5.9}$$

(for comparison see [10], sections 4.4 - 4.5). In spherical symmetry, the averaged $1D$-components of the velocity are null, and the first non-zero moments are the radial and tangential velocity dispersions:

$$\sigma_r^2(r) = \frac{2\pi}{\rho r^2} \int_0^\Psi f_0(Q) \mathrm{d}Q \int_0^{2r^2(\Psi - Q)/(1 + r^2/r_a^2)} (L^2)^\alpha \sqrt{2(\Psi - Q) - \frac{L^2}{r^2} \left(1 + \frac{r^2}{r_a^2} \right)} \, \mathrm{d}L^2 \ , \tag{5.10}$$

$$\sigma_t^2(r) = \frac{\pi}{\rho r^4} \int_0^{\Psi} f_0(Q)\mathrm{d}Q \int_0^{2r^2(\Psi-Q)/(1+r^2/r_a^2)} \frac{L^2\,(L^2)^{\alpha}}{\sqrt{2(\Psi-Q)-(L^2/r^2)(1+r^2/r_a^2)}}\,\mathrm{d}L^2\ , \tag{5.11}$$

with the total velocity dispersion being $\sigma^2(r) = \sigma_r^2(r) + 2\sigma_t^2(r)$.

By substituting σ_r^2 and σ_t^2 in Eq. (5.7) as in [39], the anisotropy profile now reads

$$\beta(r) = \frac{r^2 - \alpha r_a^2}{r^2 + r_a^2}\ . \tag{5.12}$$

Notice that, for positive α, the anisotropy is tangential in the inner regions where $r^2 < \alpha r_a^2$, zero at $r^2 = \alpha r_a^2$ and radial in the outer regions where $r^2 > \alpha r_a^2$; on the other hand, if α is negative the model is radially anisotropic everywhere and for all values of r_a.

I remind the reader that the simulated halos are centrally isotropic and radially anisotropic in the outskirts so that, with the DF chosen above, the correct value is $\alpha = 0$ for the NFW. Moreover, I set the value of the anisotropy radius $r_a \simeq 1$ [98]. With this choice of α and r_a I obtain a precise representation of the NFW halo. Under these conditions, the relation between the DF and the density profile reads

$$f_0(Q) = \frac{1}{2^{5/2}\pi^2}\frac{d^2}{dQ^2}\int_0^Q \left(1+\frac{r^2}{r_a^2}\right)\rho(\Psi)\mathrm{d}\Psi\ , \tag{5.13}$$

after integrating in dL^2 [39]. In Fig. 5.1 I plot the "energy part" f_0 of the DF defined by Eq. (5.8, 5.13) that represents the NFW, with $\alpha = 0$ and $r_a \simeq 1$ (*solid line*), compared with that of a totally isotropic halo (*dashed line*).

In Fig. 5.2 I show the halo as reconstructed through the DF defined by Eqs. (5.8, 5.13) (*solid lines*), compared with the original NFW (*dashed lines*) taken from simulations ([33],[70]); in the upper panels I show the logarithmic density profile (*left*), and the gravitational potential (*right*), as well as the rotation curve (*inset*). In the lower left panel, I show the velocity dispersion profiles for the radial (*thick*) and the tangential (*thin*) components; this halo is isotropic in the inner 10% of the virial radius, and becomes radially anisotropic in the outer regions, as mirrored by the anisotropy parameter profile (*right*).

Once I know a suitable DF, I can investigate the specific angular momentum profile yielded by the dark matter tangential random motions, that is defined as follows:

$$\langle L(r)\rangle = \frac{2\pi}{\rho r^2} \int_0^{\Psi} f_0(Q)\mathrm{d}Q \int_0^{2r^2(\Psi-Q)/(1+r^2/r_a^2)} \frac{L\,(L^2)^{\alpha}}{\sqrt{2(\Psi-Q)-(L^2/r^2)(1+r^2/r_a^2)}}\,\mathrm{d}L^2\ . \tag{5.14}$$

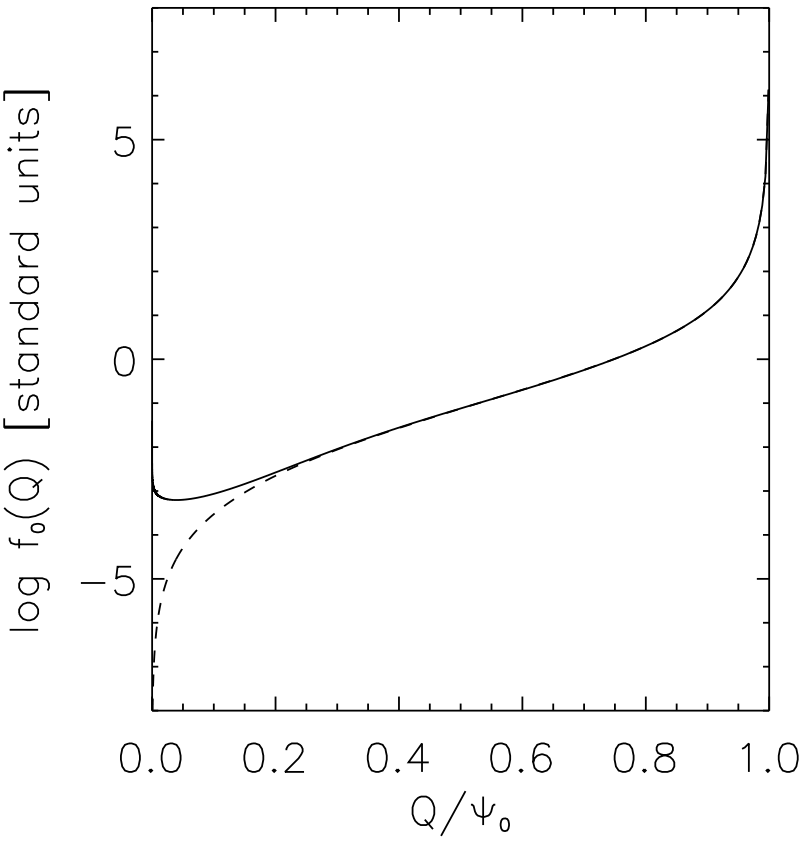

Figure 5.1 The phase-space distribution function for a NFW halo, in standard units of $G = M_H = R_H/2 = 1$, see [98]. *Solid line*: halo as simulated, isotropic in the center and radially anisotropic at the outskirts; *dashed line*: totally isotropic.

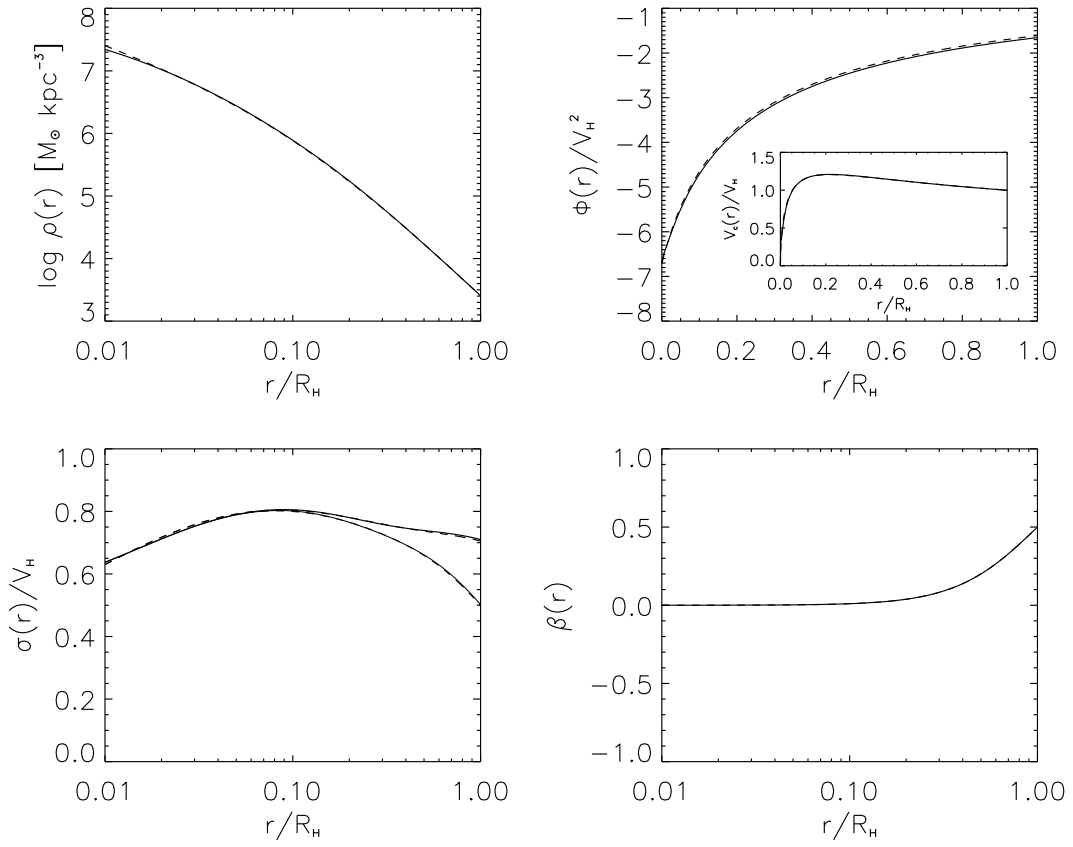

Figure 5.2 The NFW halo (*solid lines*) as reconstructed from the DF of Eq. (5.8), compared to the original one from simulations (*dashed lines*, [33],[70]). *Upper left panel*: logarithmic density profile; *upper right*: gravitational potential and rotation curve (*inset*); *lower left*: velocity dispersions profiles, radial (*thick*) and tangential (*thin*); *lower right*: anisotropy profile.

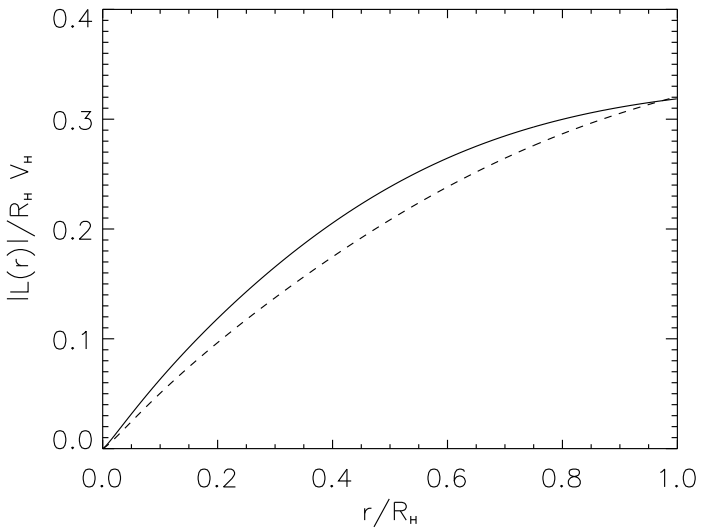

Figure 5.3 Angular momentum profile yielded by the new phase-space DF (*solid line*), compared to the unperturbed NFW one (*dashed line*), under the same unevolved gravitational potential.

Notice that, even if the averaged $1D$ velocities are null, the averaged angular momentum is nonzero, due to the symmetry of the DF, as discussed after Eq. (5.8). This is plotted as the *dashed line* of Fig. (5.3).

5.3 Perturbing the halo: the angular momentum transfer

From the above description of the halo, one can argue that the mass distribution of the system is strictly linked to its dynamics. The question that now arises is the following: is the halo stable against perturbations in its dynamical state? In other words, suppose that the halo becomes involved in a process that causes a variation in its velocity dispersion tensor, such as an increase of energy and angular momentum L; will the macroscopic observables, like the density profile, the gravitational potential and the anisotropy profile, be affected?

I defer the reader to the next section for a toy model of angular momentum transfer between baryons and DM during the first stages of galaxy formation, and I proceed now to analyze its effects on the equilibrium state of the halo.

Consider a system described by the DF of Eqs. (5.8, 5.13), and suppose to inject random angular momentum, of the kind L described above, into it; the measured value of L, given by an equation like (5.1), increases, and this is achieved by assigning a positive value to α (and a suitable value to r_a). From Eq. (5.8) one can see that the particle orbital energy increases; more importantly, from Eq. (5.12) it is clear that the anisotropy of the halo decreases and becomes negative, meaning that the tangential motions dominate.

The DF is function of both energy and angular momentum, and is a solution of the Jeans' equation; the halo is bound to conserve E and L^2 before the perturbation, and $E+\Delta E$ and $L^2+\Delta L^2$ afterwise, redistributing the excess and rearranging the DM particles in the $6D$-space of coordinates and velocities. This in turn implies an evolution of the gravitational potential; hence, the system moves towards a new equilibrium configuration of density and velocity. This process is governed by the Poisson's equation

$$\frac{\mathrm{d}^2\Psi}{\mathrm{d}r^2}+\frac{2}{r}\frac{\mathrm{d}\Psi}{\mathrm{d}r}=4\pi\,G\int_0^{\Psi}\int_0^{2r^2(\Psi-Q)/(1+r^2/r_a^2)} f(Q,L^2)\,\mathrm{d}L^2\,\mathrm{d}Q\ , \tag{5.15}$$

where α and r_a are now to be intended as the new, perturbed parameters. This integro-differential equation has to be solved for Ψ; the consistent density and anisotropy profiles are linked to the evolved potential through the Jeans' equation, or alternatively are yielded by the DF through Eqs. (5.9, 5.10, 5.11, 5.12); they are the observables of the new equilibrium state of the halo. While the complete integration has to be done iteratively, the solution for small radii is analytical, and gives an interesting insight on the behavior of the halo.

Before proceeding, note that the density profile of Eq. (5.9) can be written as

$$\rho(r)=\frac{(2\pi)^{3/2}\ 2^{\alpha}\ r^{2\alpha}}{(1+r^2/r_a^2)^{\alpha+1}}\frac{\Gamma(\alpha+1)}{\Gamma(\alpha+3/2)}\ \int_0^{\Psi} f_0(Q)(\Psi-Q)^{\alpha+1/2}\mathrm{d}Q\ , \tag{5.16}$$

after the integration in L^2 is performed explicitly. For small radii, *i.e.* when $Q\to\varepsilon\to\Psi_0$, with Ψ_0 the central value of the potential, it is easy to see that $\rho(r)\propto 1/r\propto 1/[\Psi_0-\Psi(r)]$; by changing variable in Eq. (5.13) from ε to $(\varepsilon-\Psi)/(\Psi_0-\varepsilon)$, the energy part of the DF behaves like

$$f_0(\varepsilon)\propto(\Psi_0-\varepsilon)^{-5/2}\ . \tag{5.17}$$

I then put this expression into Eq. (5.16), and pass from ε to $(\Psi-\varepsilon)/(\Psi_0-\Psi)$; I find the

density profile at small radii to behave as

$$\rho(r) \propto [\Psi_0 - \Psi(r)]^{\alpha-1} r^{2\alpha} \ . \tag{5.18}$$

I now insert this expression into the Poisson equation (5.15), to obtain the self-consistent solution for the new potential $\Psi(r)$, which reads

$$\Psi_0 - \Psi(r) \propto r^{2\,(\alpha+1)/(2-\alpha)} \ . \tag{5.19}$$

Finally, the new density profile $\rho(r)$ from Eq. (5.18) reads

$$\rho(r) \propto r^{-2\,(1-2\alpha)/(2-\alpha)} \ . \tag{5.20}$$

Thus I find that for $\alpha \to 0$ the inner profile behaves like r^{-1} (NFW), while for $\alpha \to 1/2$, *i.e.* when the DF is linear in L, I obtain $\rho(r) \to$ *constant*, which is a core. For intermediate values of α I obtain anything between a cusp and a core; for values of α larger than $1/2$ the density profile is not realistic, featuring a "hole" in the centre, while for negative values of α, corresponding to enhancing the radial motions over the tangential (or, alternatively, to subtracting angular momentum from the halo) the cusp's slope steepens.

Notice that, from Eqs. (5.12) and (5.16), I conclude that $\rho(r) = \rho(r, \beta)$, and for $r \to 0$,

$$\rho(r) \propto r^{-2\,(1+2\beta)/(2+\beta)} \ , \tag{5.21}$$

i.e. the density profile is a function of the anisotropy parameter, that represents the balance between the radial and tangential motions inside the halo; it is then clear that the shape of the velocity dispersion tensor determines the halo mass distribution. In particular, for $r \to 0$ the anisotropy parameter behaves like $\beta(r) \to -\alpha$, therefore for $\alpha = 1/2$ the halo features a constant tangential anisotropy in the inner regions. The corelike feature in a halo is always accompanied by tangential anisotropy, and it is possible to verify that radially-dominated halos cannot develop a core.

The value of α determines the inner specific angular momentum profile as well, which is obtained as

$$L(r) \propto r\ [\Psi_0 - \Psi(r)]^{1/2} \propto r^{3/(2-\alpha)} \ ; \tag{5.22}$$

notice that for the unperturbed halo $L(r) \to r^{3/2}$ and for $\alpha = 1/2$ I get $L(r) \to r^2$.

Along with these analytical results, I performed the full numerical integration of Eq. (5.15). As a boundary condition throughout this computation I adopted the halo mass conservation; I further normalized the evolved potential in order to obtain the same behavior of the outer rotation curve as before.

It is interesting to analyze this process in two steps: since the density and anisotropy profiles and the potential well evolve together, it is impossible to evaluate the variation in the angular momentum of the system after the new equilibrium state is reached from Eq. (5.14), because the system has then lost memory of its initial conditions. Instead, suppose to picture the halo at the moment when it receives its input in energy and angular momentum, but the potential well has not yet evolved; then I can evaluate the amount of angular momentum that has been injected into the halo. In Fig. 5.3 I show the specific averaged angular momentum profiles as yielded by the old, NFW-like (*dashed*), and new (*solid*) DFs, in the same potential. Keep in mind that this is not a stable state, the system is unbalanced and is going to evolve into a new configuration that satisfies the Jeans' equation.

The final configuration of the system, corresponding to its new equilibrium state (with $\alpha = 1/2$), is showed in Fig. (5.4). The density profile (*upper left*) has been smoothed and the cusp erased; this mirrors the mass loss experienced by the inner regions of the halo, since the DM particles have been moved to more energetic orbits. Notice the corresponding flattening of the potential well (*upper right*). Accordingly, the rotation curve (*inset*) is more gently rising in the inner regions and is nearly unchanged beyond half of the virial radius.

As for the velocity dispersion, the symmetry between the radial and tangential motions has been broken in favor of the latter (*lower left*); correspondingly, the anisotropy parameter profile (*lower right*) is now negative in the inner halo and changes sign at a radius corresponding to the new $r_a = 1/\sqrt{2}$, that is set by requiring the same outermost value of $\beta(r)$ as before, although it scarcely affects the results shown above.

In sum, given the DF of equation (5.8), the couple ($\alpha = 0,\ r_a \sim 1$) describes the known NFW halo, cuspy and almost entirely isotropic, while the couple ($\alpha = 1/2,\ r_a \sim 1/\sqrt{2}$) produces a corelike halo, with a constant inner density profile and a tangentially-dominated inner anisotropy profile.

It is also interesting to see the behaviour of the evolved halo in phase space; in

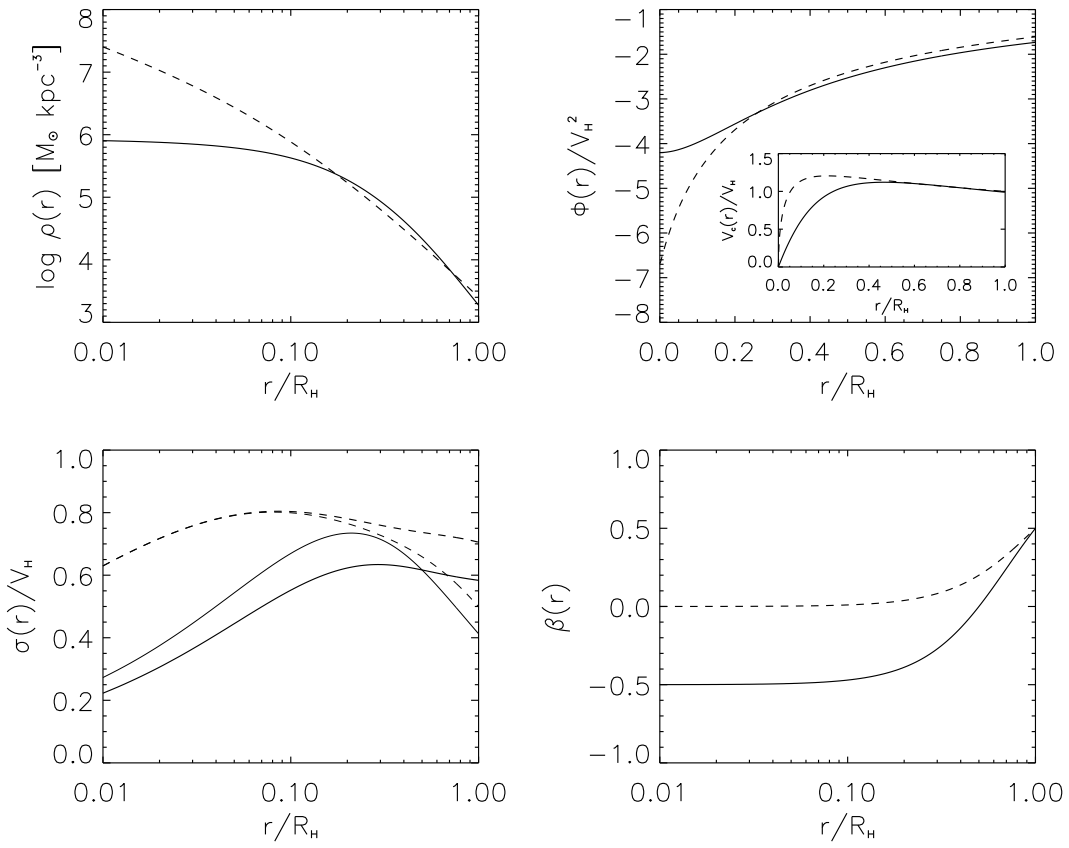

Figure 5.4 New equilibrium configuration of the perturbed halo (*solid lines*), compared to the initial NFW (*dashed lines*). *Upper left panel*: logarithmic density profile; *upper right*: gravitational potential and rotation curve (*inset*); *lower left*: velocity dispersions profiles, radial (*thick*) and tangential (*thin*); *lower right*: anisotropy profile.

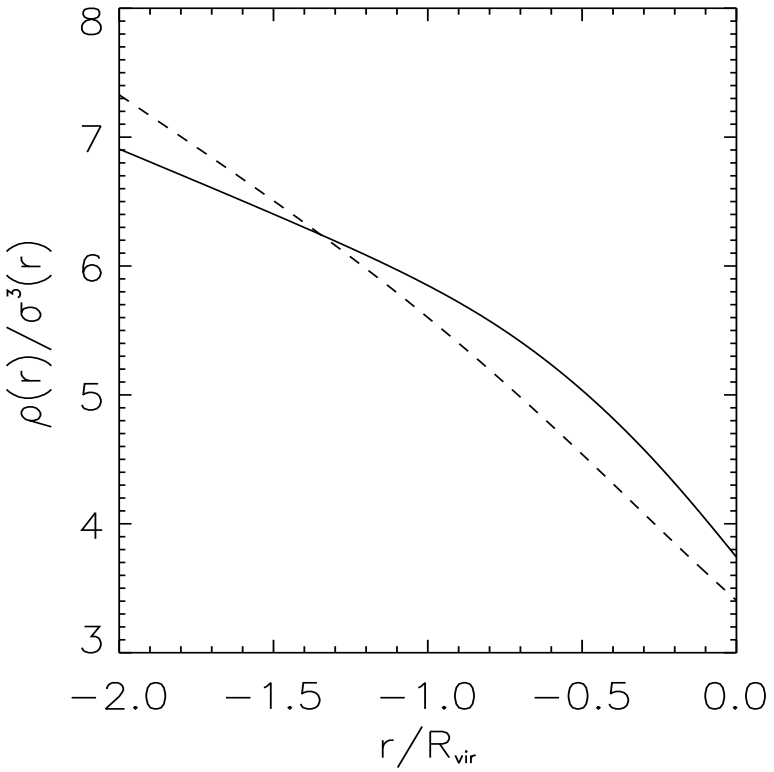

Figure 5.5 The phase-space density ρ/σ^3 of the unperturbed NFW (*dashed*) and of the perturbed halo (*solid*) as a function of radius, to be compared with Fig. (1.2). The injection of tangential motions increases the entropy in the center of the halo and flattens out the power-law.

Fig. (5.5) I show the phase-space density ρ/σ^3 for the original NFW (*dashed line*) and for the perturbed halo (*solid line*), to be compared with Fig. (1.2) in Chapter 1. Notice that the DF described by Eq. (5.8) yields the power-law dependence on radius expected for the NFW, with the correct slope. The injection of tangential motions into the halo, however, perturbs the phase-space structure by increasing the entropy in the center of the halo, thus flattening out the power-law.

I point out that the injection of angular momentum of the kind described here generates additional random tangential motions, that do not produce an *ordinate* rotation; in fact, the symmetry of the halo and its dynamics are determined by the DF, that does not define a preferential direction of rotation (*i.e.* this halo has no spin). The DM particles move on orbits around the center of mass with random orientations, so that the resulting angular momentum L^2 is nonzero, but the average value of each velocity component is null.

Notice also that the assumption of injecting angular momentum into the halo is quite realistic, since halos interact only gravitationally; any tidal encounter, accretion of satellite or merging is accompanied by angular momentum exchange. A pure energy transfer on the contrary, is quite difficult to achieve, and given the DF described by Eq. (5.8), it is clear that it would have no effect on the equilibrium state of the halo; in fact, injecting or subtracting energy would enhance or diminish the velocity dispersions isotropically, without unbalancing the anisotropy profile. With the same dispersion tensor, the mass distribution would conserve its shape, and only expand or contract.

5.4 Dynamical friction as an angular momentum engine

Is there a physical process that can account for the evolution described above? In this Section I present a toy model that provides the halo with such an amount of random angular momentum to allow it to evolve from a cuspy to a cored configuration. The natural framework is galaxy formation, when the baryons collapse inside the halo potential well and exchange angular momentum with the dark matter through dynamical friction.

Specifically, in the very early stages of galaxy formation, the baryons trapped inside the potential wells of the halos undergo radiative dissipation processes that cause

them to lose kinetic energy and to condense in clumps inside the relatively smooth dark halo. If radiative cooling is effective, the gas will organize into self-gravitating clouds before it collapses to the halo center and fragments into star-forming units; moreover, the clouds are likely to survive the tidal stripping due to the DM, because of their relatively high binding energy [108]. The infalling, clumpy gas component decouples from virial equilibrium, and while the clouds spiralling down get closer and closer to the halo center, increasing their tangential velocity along their orbits and reaching regions with higher and higher density, they dissipate their orbital energy.

In these regions in fact, a gravitational effect becomes relatively efficient in slowing down the clouds, namely the dynamical friction exerted by the background DM particles, that causes part of the cloud tangential velocity to be transferred from the baryons to the DM itself. Notice that, for clouds spiralling down the potential well, the istantaneous orbit is elliptical, and the radial component of the velocity is on average much smaller than the tangential; thus, the radial velocity transfer is negligible. A complementary analysis of this process, focussing on the energy transfer from the baryons to the dark matter, that causes halo expansion, can be found in ([60],[61]). Conversely, I specifically focus on angular momentum transfer, the reason being that energy transfer alone is not viable to unbalance the halo anisotropy profile; in this case, any expansion could be contrasted by the deepening of the potential well caused by the baryonic mass accumulating in the halo center.

As a result of the dynamical friction, the inner part of the halo is therefore granted with a surplus of angular momentum L (as described above) and energy, depending on the number, mass and initial velocity of the clouds.

Consider a cloud of mass M_c that at time $t = 0$ is at a certain distance from the center of the halo, with initial velocity $v^2 = v_r^2 + (L/r)^2$ and angular momentum L; I define the initial pericenter of its orbit as $r_+(0)$, the eccentricity as $e(0)$, and the apocenter as $r_-(0) = r_+\,(1-e)/(1+e)$. The cloud is self-gravitating and hence I consider it as a point mass, immersed in the halo potential well; in the orbit-averaged approximation [96], the equations of motions for the cloud energy and angular momentum are given by

$$\frac{\mathrm{d}E}{\mathrm{d}t} = -\frac{\int_{r_-}^{r_+} (1/v_r) \;\; v\,|F_{\rm frc}|/M_c \;\mathrm{d}r}{\int_{r_-}^{r_+} (1/v_r)\;\mathrm{d}r}\;, \tag{5.23}$$

$$\frac{\mathrm{d}L}{\mathrm{d}t} = -\frac{\int_{r_-}^{r_+} (1/v_r) \;\; L\,|F_{\rm frc}|/(M_c v)\;\mathrm{d}r}{\int_{r_-}^{r_+} (1/v_r)\;\mathrm{d}r} \;, \tag{5.24}$$

with initial conditions set by

$$L(0) = \sqrt{\frac{2[\Psi(r_+) - \Psi(r_-)]}{1/r_+^2 - 1/r_-^2}} \;, \qquad\qquad E(0) = \Psi(r_+) + \frac{v^2(r_+)}{2} \;. \tag{5.25}$$

At each instant, the force exerted by the background DM particles on the cloud is [10]

$$|F_{\rm frc}| = -4\pi G^2\, M_c^2\, \ln\Lambda\, \frac{\int_0^v f(v')\;\mathrm{d}^3v'}{v^2} \;, \tag{5.26}$$

in terms of the NFW phase-space distribution function f (see Section 2), of the cloud speed $v = \sqrt{2[\Psi(r) - E(t)]}$ and of the Coulomb logarithm $\ln\Lambda = \ln(M_H/M_c)$ [10]. At each timestep, $r_\pm(t)$ are given by the condition $v_r^2 = \sqrt{v^2 - L^2/r^2} = 0$. Due to the dynamical friction, the orbit shape and the velocity of the cloud evolve in time, so that this set of equations has to be solved iteratively.

For a halo of virial mass M_H I performed a series of Montecarlo simulations for different realizations of the baryonic component, organizing it in ensembles of clouds, characterized by a mass function scaling as $M_c^{-\delta}$, with index δ ranging from 0 to 2; both these extremes are to be considered unrealistic, 0 corresponding to a constant mass function, and 2 yielding an excessive clumping factor. In each realization, I allowed the cloud masses to range from 10^{-5} to $10^{-2}\,M_H$ [61]. The number of clouds is actually constrained by the total amount of baryons, set to equal the cosmological fraction $0.16\,M_H$. The initial spatial distribution of the clouds is uniform between $r = 0$ and $r = R_H$; at time $t = 0$ the clouds are in statistical equilibrium with the background halo, therefore I randomly sampled their initial velocities from a Maxwellian distribution, with mean 0 and variance $\langle\sigma_{t,r}^2\rangle/2$.

For each δ I performed 100 runs, and computed the average specific angular momentum transferred by the clouds to the halo after 2 Gyr; I expect that after this time the inner part of the halo becomes so crowded with clouds that they start to collide and disrupt, and the star formation effects dominate over the dynamics of the gas [61]. However, in the outer regions the process continues with longer timescales, so that I also followed the evolution of the system for about 6 Gyr.

In Table 5.1, for each δ I give the average number and mass of the clouds, the total angular momentum gained by the halo, and the mass accumulated in the center of

Table 5.1. Dynamical friction results

δ^a	$\langle N_i \rangle^b$	$\langle M_c \rangle^c$	$\langle \Delta L_{DM} \rangle^d$	M_g (2 Gyr)^e	M_g (6 Gyr)^f
0	31.45	5.03e-3	1.04	0.039	0.074
1	109.66	1.46e-3	1.86	0.032	0.064
2	2276.98	7.05e-5	7.54	0.019	0.043

Note. — Column label: (a) cloud power-law mass function index; (b) average number of clouds; (c) average cloud mass (units of M_H); (d) average of the exchanged specific angular momentum (units of $R_H\ V_H$) integrated over the profile; (e) average baryonic mass that falls inside $0.1\,R_H$ after 2 Gyr and, (f) after 6 Gyr (units of M_H).

the halo after 2 and 6 Gyr. Note that with my power-law mass functions, the massive clouds constitute a small fraction of the total; on the other hand, the dynamical friction is more effective on them, and therefore they have a large probability to lose all their angular momentum quickly, and to collapse in the center of the halo soon. The small clouds instead take more time to spiral down in the halo potential well, and retain a larger fraction of their initial angular momentum. Notice that this is consistent with a scenario of rapid initial baryonic collapse followed by smooth subsequent infall, and that depending on the initial cloud mass function, the morphology of the galaxy could be affected [177]. In the end, a steeper mass function, that selects a high number of small clouds, results in a more effective transfer of angular momentum L to the halo.

In Fig. 5.6 I illustrate an example of the time evolution of a set of clouds sampled with power-law index $\delta = 1$. In the time interval from $t = 0$ to $t = 6$ Gyr a fraction of the clouds reaches the inner 10% of the virial radius (*upper panel*), building up the mass that is likely to end up in the spheroidal component of the forming galaxy. In the middle panel I show the evolution of the orbit eccentricity, and in the lower panel the angular

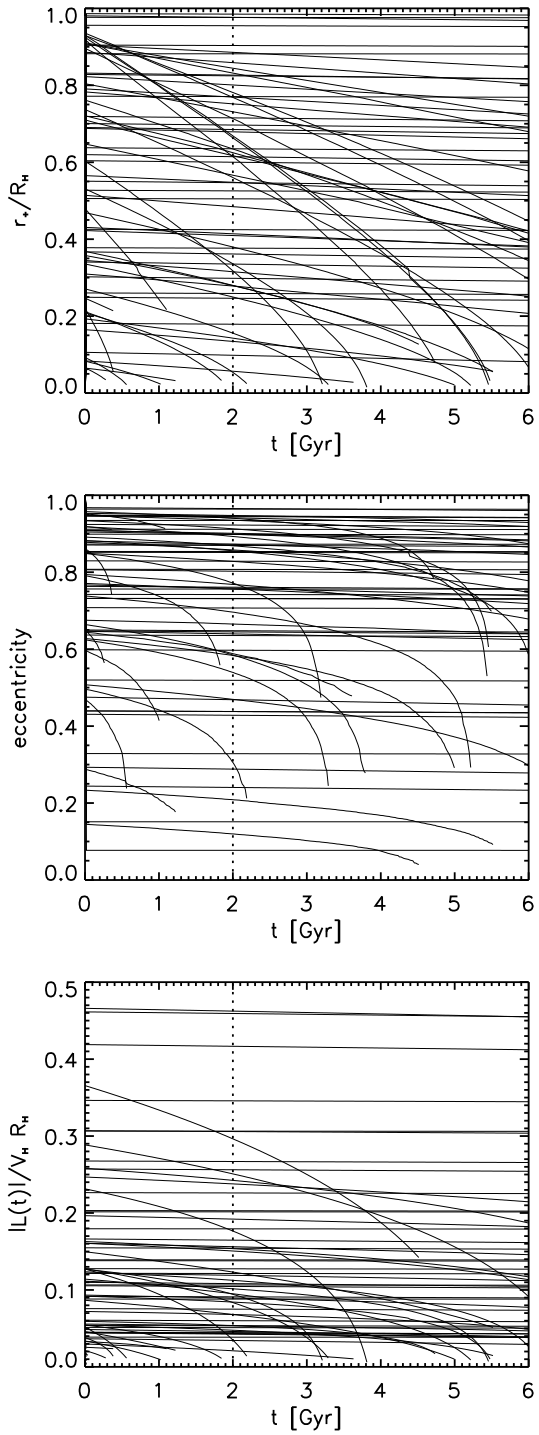

Figure 5.6 Time evolution of a set of clouds sampled with power-law index $\delta = 1$. *Upper panel*: apocenter of the orbit; *middle panel*: orbit eccentricity; *bottom panel*: angular momentum retained by the clouds.

momentum lost by the single clouds and transferred to the halo. Notice that the fraction of clouds that effectively transfer angular momentum to the halo is relatively small, and that the majority of the clouds remains on almost unperturbed high orbits, meaning that the timescales of dynamical friction are long. This effect is enhanced for increasing δ, as shown in the last two columns of Table 5.1; a steeper mass function results in a slower accumulation of baryons in the center. In any case, the final amount of baryons inside the inner 10% of the virial radius after 2 and 6 Gyr is overabundant with respect to the known galactic masses (spheroidal and/or disk components; see [157]), due to the fact that the total baryonic component initially matches the cosmological fraction. However, while baryons accumulate in the center of the potential well and organize themselves into the protogalactic structure, star formation and AGN activity start, along with the ensuing feedback processes that eventually regulate the actual amount of baryons. Notice that these feedback mechanisms can in no way affect the transfer of angular momentum between the visible and dark components, as they take place after the cloud collapse; as will be discussed in the next section, the mass of the growing baryonic component at the center of the halo can affect the final dynamical state of the system only marginally.

Notice also that the angular momentum transfer from the clouds to the dark matter happens locally, and with random orientations; this corresponds to the kind of random angular momentum L described in the previous Sections.

In Fig. 5.7 I present the final angular momentum profile of the halo, for $\delta = 0, 1, 2$. From each run of my simulation I extract a transferred momentum profile ΔL after 2 Gyr and then add it to the original NFW (*dashed lines*, see also Fig. 5.3); the *shaded areas* represents the overlap of all the resulting new profiles. For comparison, I plot the profile obtained in Section 3 through the transformation of the DF (*solid lines*, see also Fig. 5.3).

I find that the angular momentum profile produced through the dynamical friction mechanism is clearly compatible with that resulting from the perturbation of the halo DF described in Section 3. In fact, the effect of the dynamical friction on the halo is of enhancing the random tangential motions with respect to the radial; this produces an unbalance in the velocity dispersion tensor, with an anisotropy profile that becomes more tangential in the center of the halo, where the dynamical friction is more effective.

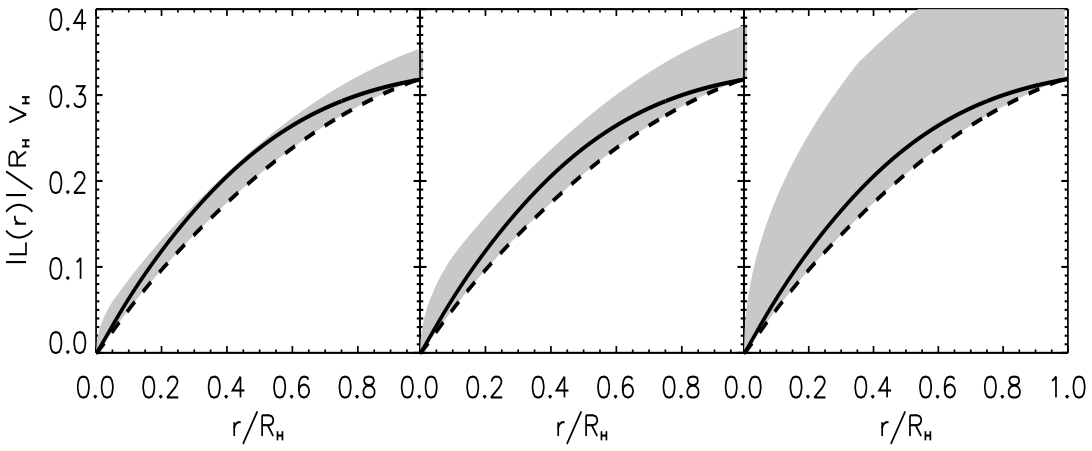

Figure 5.7 Comparison between the angular momentum profiles yielded by the phase-space DFs and by dynamical friction. *Dashed line*: unperturbed NFW halo (see Section 2); *solid line*: perturbed halo, new DF (see Section 3); *shaded regions*: NFW angular momentum profile plus ΔL from dynamical friction, for $\delta = 0$ (*left*), $\delta = 1$ (*center*) and $\delta = 2$ (*right*).

5.5 Discussion and conclusions

In the previous Chapters I collected some observational evidence about an incompleteness in the theoretical description of galaxy formation in the CDM hierarchical scenario, resulting in a discrepancy between the predicted and observed mass distribution of DM halos, and the predicted and observed spin parameter distribution function. The limited mass range of halos affected by this issue (galactic halos), along with the scale where the discrepancy manifests itself (galactic scale), on the one hand excludes that this is a fundamental problem of the whole hierarchical scenario, that still works on groups and clusters scales, and on the other rules out that this is merely a numerical problem originating from the failure of N-body codes to represent very small scales.

I approached this topic from the point of view of the coevolution of the baryons and their host DM halo, and investigated whether the mechanism of galaxy formation involves perturbations in the halo structure, big enough to rearrange its mass and velocity distribution, flattening the inner density profile with a mass transfer to outer regions, and thus reconciling the observational evidences with the standard theory of hierarchical clustering.

The NFW halo is rather sensitive to variations of its anisotropy profile; if the tangential components of its velocity dispersion are enhanced, for instance by means of a transfer of random angular momentum as shown in this Chapter, its phase-space structure enters a new equilibrium configuration, and a flat density profile can be attained.

From the macroscopic side, I looked for a mechanism of random angular momentum transfer that directly involved the baryons, that was especially efficient during galaxy formation, and that directly affected the microscopic state of the system; thus I focused on dynamical friction ([60],[61]). Angular momentum can be transferred to the halo also by tidal interactions and mergers; however, such events are less and less frequent with decreasing redshift both for spheroidal galaxies ([93],[56]) and for spirals ([53],[176], and Chapter 2). Moreover, such interactions between the halo and its neighbours occur on scales comparable to that of the halo itself, thus giving rise to perturbations of its dynamical state that produce global ordinate motions; these events are thought to produce the halo spin.

When modelling the phase-space DF, I had to face the degeneracy intrinsic to this kind of problem, that makes its determination not unique (contrary to the case of isotropic halos). With the method described in this Chapter, I ensure that the adopted DF describes an equilibrium phase-space configuration [39], and that it reproduces the observables of a given halo (density, anisotropy and velocity dispersion profiles, rotation curve and potential). Moreover, regardless of the particular shape of the function, the symmetry of the system in phase-space is set by the DF explicit dependence on the integrals of motion, thus the halo dynamics is set with no ambiguities.

For an isotropic NFW, $f(\mathbf{x},\mathbf{v}) = f(\epsilon)$, *i.e.* the phase-space coordinates are completely determined by the particle's energy. A symmetry breaking between the radial and tangential components of the velocity dispersions causes an evolution of the system into $f(\epsilon, L^2)$, thus the shape of the mass distribution depends explicitly on the shape of the anisotropy profile: $\rho(r) = F(\beta(r))$. In physical terms, the excess or deficit of tangential motions determines a mass rearrangement to attain equilibrium.

Notice that this kind of DF cannot account for the halo spin L_z, that is found to be $\lambda \sim 0.03 - 0.06$ from observations and simulations (see [176] and Chapter 2). This value of λ is small, nonetheless it yields information on the true shape of the halo in phase-space.

Following from the Strong Jeans theorem ([10]; see Chapter 1), a real collisionless system such a DM halo would be described by a DF function of 3 integrals of motion, and following the approach of this Chapter, it would be of the form $f(\varepsilon, L^2, L_z)$; the explicit dependence on L_z, setting a preferential direction of rotation, would manifest itself at the breaking of the symmetry between the two tangential velocity components.

A generalized DF could be written as $f(Q, L^2, L_z) = f_0(Q)\, f_1(L^2, L_z)$, where f_1 may be a power-law or a more complex function, odd in L_z to produce net bulk rotation around the symmetry axis. With this DF the average $1D$ tangential velocity $\vec{v_t}$ parallel to the equatorial plane is not null, and the halo features a macroscopic total angular momentum in the z-direction, $\vec{L_z} = \vec{r} \times \vec{v_t}$, that is aligned with the spin, $\lambda \simeq v_t/\sigma$.

In the computation of the perturbed gravitational potential I did not include the baryonic mass; although the baryons piling up in the center of the halo tend to deepen the well, this process does not interfere with the flattening of the density profile. In fact, three considerations are needed here: 1) the final amount of baryons that is actually observed in the center of halos is deeply connected with feedback processes, that are responsible for removing at least half of the initial baryonic mass [157]; 2) as hinted in Section 1, the feedback processes themselves can transfer energy to the DM and cause halo expansion; 3) most importantly, the dominant effect in changing the equilibrium configuration of the halo is the symmetry breaking of the velocity dispersion tensor, that determines the final density profile, regardless of the depth of the potential well. For this reason, the excess of mass carried by the baryons simply produces an isotropic enhancement of all the σ components, that may cause contraction or expansion without preventing the flattening of the density profile. Notice that, for the same line of reasoning, mechanisms to erase the cusp that are based on feedback alone (like [112] where the baryonic mass loss produces a core) are implausible because they cause temporary expansion out of equilibrium, without transforming the halo into a stable new configuration.

Up to now, there is no definite knowledge of the details of the baryon collapse into the protogalactic structure. Nevertheless, if dynamical friction indeed plays a major role in the collapse, it could affect the morphology of the galaxy that is to form, possibly through its timescale that in turn depends on the cloud mass function, and in conjunction

with feedback processes.

In this scenario, spheroids may be formed by the massive clouds, that lose all their angular momentum and collapse early and quickly; rapid and intense star formation would arise at the center of the halo, where the clouds crash into one another and settle down. On the other hand, small clouds are slower in losing their momentum and tend to stay on higher orbits, thus being more likely to end up in a rotating disk; feedback from the forming galaxy is likely to be more efficient on small clouds, thus preventing star formation in the more external regions until later times. The slow, gradual accretion of small clouds and the consequent propagation of star formation can be assimilated to the *inside-out* formation of disks [31]. As a possible evidence of this process, I can point out the molecular clouds that today travel across the Galactic disk, trapped inside the potential well of the DM halo; they may be the low-mass tail of the cloud mass function. So small as to have been only marginally affected by dynamical friction, they are still on high orbits and are not yet actively participating to the growth of the disk. In this picture, the initial conditions of the baryonic collapse play an important role.

From the dark point of view, a similar argument holds; depending on the details of the baryon collapse and dynamical friction, the equilibrium structure of the halo evolves into different final states. This hints to a very complex picture, where the dark matter density profile is not universal, but strongly depends on the baryonic structure that forms within the halo. In my opinion, it would be very interesting to look for patterns in the co-evolution of the luminous and dark structures; I find this approach most promising to understand the mechanisms of galaxy formation.

Chapter 6

Simulating the infalling of substructures

I present my work in progress, on the topic of dark matter substructures and halo evolution. I am currently engaged in devicing a simulation able to correctly reproduce the dynamical friction inside halos, for a double purpose; (i) to test the semi-analytical model presented in Chapter 5, and (ii) to address the issue of the disruption of satellites infalling into a dark matter halo, in an attempt to find a solution to the problem of the overabundance of substructures predicted in galactic systems. I describe the method for writing initial conditions for a simulation featuring stable halos with different phase-space equilibrium structures, and eventually report my plans for the suite of simulations.

6.1 Introduction

The hierarchical evolution of a generic dark matter halo can be roughly divided into two phases; the mass accretion phase, during which smaller subunits merge and build up its mass, shaping its equilibrium structure, and the satellite phase, during which the halo itself is accreted onto a larger object.

The universal structure of pure DM halos that grow hierarchically arises from physical mechanisms that smooth out the clumpy satellite component infalling onto the

parent halo (see Chapter 1); on the other hand, the inner regions of early virialized objects often survive accretion on to a larger system, thus giving rise to a population of subhaloes. This substructure evolves as it is subjected to the forces that try to dissolve it: dynamical friction, tidal forces and impulsive collisions. Depending on their orbits and their masses, these subhaloes therefore either merge, are disrupted or survive to the present day ([184]). From Chapter 5, it should be clear that the processes that determine the satellite disruption are the same that shape the halo equilibrium structure in reaction to the accretion, whether of luminous or dark components.

A longstanding prediction of the theory of hierarchical clustering is that the subhalo population is self-similar, with low-mass systems such as galaxies being simply scaled-down versions of larger systems like clusters ([55],[184] and references therein). This would imply that the subhalo mass function is independent of the parent halo mass. The Milky Way for instance is predicted to have nearly the same distribution of substructures (scaled down in mass) as the Virgo cluster ([92],[111]). These expectations are supported by numerical simulations, that predict about 500 satellites in Milky Way-like objects. Observations of galactic systems (see for instance the SLOAN data, [204],[91]) find ~ 30 satellites in the Local Group, highlighting an offset in the theoretical predictions of more than one order of magnitude. Moreover, [54] showed that fossil groups with intermediate mass between the Local Group and the Virgo cluster feature the same lack of substructures. Some authors (see for instance [167]) suggest that the discrepancy in general arises because a large number of satellites are dark, *i.e.* they contain no stars; the problem with this approach is that disk galaxies would be perturbed by the dark substructure nevertheless, with the consequent heating of the thin disk and visible, and disruptive, effects.

The offset between the predicted and observed substructure mass function and distribution points towards what has been called the "missing satellite problem". Obviously, this is rather an "overabundant substructure problem" of numerical simulations and of the hierarchical clustering picture. Numerical simulations have been on the scene for more than 20 years [197]; in time, the coding techniques have been constantly refined, and the resolution and dynamical range of the runs has improved enormously. Still, simulations are not always the best of tools in studying dark matter structures, and despite their terrific

performance on large scales, they cannot address many questions regarding the detailed physical processes taking place inside galaxies. Among these in particular, the effects of tidal stripping and dynamical friction on the orbits of satellites are not satisfactorily reproduced ([186],[180],[35],[103],[177]), along with the aforementioned survival and evolution of substructures ([109],[171],[80]); as for the baryons, the heating of galactic disks due to substructure remnants, ([144],[187],[172],[66]), the susceptibility of disks to bar instabilities [106], and the effects of these bars on the halo central density cusps ([45],[3],[178]) are not well traced [87].

In this Chapter, I address the issue of simulating the infalling of substructures in a parent halo, focussing on the correct implementation of the physics of dynamical friction, in order to test it as a viable mechanism to alleviate the satellite discrepancy; in fact, the dynamical coupling between the parent halo and an infalling object affects the structure of both, with the result that the subhalo can be unbound and destroyed. There have been recent attempts at specifically simulating dynamical friction on dark matter satellites accreted into larger systems, with positive results for cluster and galactic halos ([116],[101]). In particular [101] find that the same mechanism is able, under certain conditions, to flatten the parent halo's inner density profile.

The numerical representation of dynamical friction, as well as tidal stripping and all the small-scale processes, is indeed a delicate procedure, with many caveheats and problems. Let alone the implementation of the baryonic physics, the numerical modelling of the gravity and dark matter dynamics encounters serious difficulties at small scales. In fact, the scale-invariance of the NFW mass distribution resulting from simulations has induced many into thinking that the accuracy and robustness of the numerical treatment of the halos is not affected by scale either, and that the method can be safely extrapolated to the small scales. Actually, this operation is subject to a number of risks, arising from problems intrinsic to the numerical method. For instance, the extreme coarse-graning of a simulated system (the halo is modelled as an ensemble of particles of given phase-space dimension) affects the mixing mechanisms in an unknown way (see [10],[50]). Moreover, the limited mass range accessible with the numerical treatment generates two main problems. First, a simulation of dynamical friction needs a very high resolution, because the process efficiency

is extremely sensitive to the ratio between the test particle (the cloud for instance) and the background particle (the DM); but even with the state-of-the-art computational facilities, it is virtually impossible to correctly model gravitational effects that stem from the behaviour of the DM as a smooth fluid of microscopic particles and from *local* variations of the smooth background potential, while considering objects of the size of dark matter halos. Second, and unfortunately opposed to the previous point, the higher the ratio between the test particle and the background particle, the more the 2-body scatterings between the two components become important, making the infalling cloud behave like a bowling ball among the pins. If the softening length applied to the potential in order to avoid these spurious interactions is set on the small background particle's dimension, it would have no effect whatsoever in preventing the scattering; on the contrary, if set on the cloud's dimension, it would be so large that the background particles would not feel the cloud at all, and they would let it pass through the halo undisturbed (C. Frenk, private communication).

Still, I am currently making an attempt at numerically modelling the dynamical friction inside halos. A way around the main difficulties with the method involves the use of dark matter substructures instead of solid bodies like clouds; in this case, the infalling object is made of particles itself, of size comparable to the background ones, and this should in part smooth out the unwanted 2-body interactions. On the other hand, the object is not totally self-gravitating once it enters the parent halo, but it is subject to tidal disruption; this works against dynamical friction, in that the mass of the object is decreasing as it falls towards the centre of the halo.

On the bright side, having dark matter substructures fall into the parent halo allows me to learn something about the fate of the satellites at the same time, studying their disruption and the mass accretion mechanisms, as depending on a number of boundary conditions. In particular, I am interested in investigating the fate of satellites with different phase-space structures, like for instance cored *versus* cusped, or with isotropic *versus* anisotropic velocity dispersion tensors; obviously, I need a very high number of particles, in order to model the satellites with an accuracy high enough to properly represent different inner structures. In addition, other parameters like the satellite's initial velocity or orbit eccentricity are likely to affect its evolution.

My simulations are performed with the use of the facilities of the Institute for Computational Cosmology in Durham. The simulation code is Gadget-2 ([165],[166]).

6.2 Setting the initial conditions for equilibrium DM halos

Since I need to build isolated halos with different and well defined phase-space structures, and sort them into parent and satellites, the latters organized following some distribution in mass and orbital parameters, I cannot use halos taken from cosmological simulations, but rather I need to write controlled initial conditions (ICs). If the halos are anywhere near realistic, building numerically their equilibrium structure is not an easy task. For brevity I will describe the procedure for an isotropic NFW, while a generalization to a halo of any generic phase-space structure follows from Chapter 5.

There are two steps in constructing a numerical halo: (1) finding the phase-space distribution function (DF) producing the desired equilibrium structure; (2) using Monte Carlo samplings of this DF to generate the N-body realization. It should be clear, from Chapter 5, that determining an equilibrium DF for a given halo structure is the actual main difficulty of this process. Simple, analytical DFs are known only for a handful of models, such as Plummer spheres [140], lowered isothermal models (e.g. King models [89]), lowered power-law models ([62],[95]), and a few special cases (e.g. the Hernquist model [82], and [85],[49]). There is no universal procedure to achieve the determination of the DF, but according to the single cases, different methods can apply. For the NFW, one way is to follow Chapter 5, and use the "theoretical" DF described there. However, the N-body NFW is only an approximation of the theoretical one, being truncated at large radii to yield a finite mass, and being softened at small scales; not sure about the effects of these features on the DF, I chose to find a steady-state DF numerically, that reproduces the desired density and velocity anisotropy profiles.

Following the suggestion of [87], I avoided a shortcut often used in the literature (see for example [164],[15]), *i.e.* of finding the velocity distribution by means of the *local maxwellian approximation*; with the latter, the velocity at each point in space consistent with a given potential is approximated by a multivariate Gaussian, whose *mean* velocity

and velocity dispersion tensor satisfy the Jeans' equation at this point (see [83]). In fact, there is a dangerous shortcoming of this approximation when it is used to generate initial conditions for high-resolution numerical simulations; most of the models of interest have local self-consistent velocity profiles that become strongly non-Gaussian, especially near the center so that, if one uses the local Maxwellian approximation to construct an N-body realization of such a model, the center of the resulting N-body system will be far from equilibrium. When the halo is evolved in isolation, it rapidly relaxes to a steady state whose density and velocity profiles differ significantly from the initial, intended ones. In particular, satellites constructed using the local Maxwellian approximation can undergo rapid artificial tidal disruption [87].

With no other help, the numerical determination of the DF for a given halo follows the theoretical treatment, with some computational issues to consider.

The first step is to set the mass distribution of the halo. The NFW *per se* has an infinite mass, so I need to cut it at some point, that is taken far outside the virial radius in order to avoid boundary effects on the halo particles; the cutting function must be smooth, since a sharp truncation would lead to unphysical models with $f < 0$. Of course, this results in a waste of particles used to represent uninteresting regions of the system. The density profile I adopt features an exponential cutoff [164]; I will refer to it as the "modified NFW":

$$\rho(r) = \frac{c^2\ g(c)}{4\pi}\ \frac{1}{r\ (1+cr)^2} \quad for\ r\ < 1 \tag{6.1}$$

$$\rho(r) = \frac{c^2\ g(c)}{4\pi}\frac{1}{(1+c)^2}\ r^{\gamma}\ e^{(1-r)/R_{decay}} \quad for\ r\ > 1 \tag{6.2}$$

here all the distances are in units of the virial radius R_{vir}; r is the radial coordinate defined on a grid uniformly spaced in logarithm, R_{decay} is a parameter setting the sharpness of the profile decay that starts after the virial radius, and $\gamma = (-1-3c)/(1+c) + R_{vir}/R_{decay}$ is set by the condition of a continuous logarithmic slope, that insures the smoothness of the transition at R_{vir}. The minimum radius of the system is chosen in order to be sufficiently close to the centre of mass (for example, $r_{min} = 1e-3$); the maximum radius R_{cut} is chosen as the distance from the centre where the density falls below a given threshold value ($\rho < 1e-10\ \rho_{central}$ for instance). As an example, for a halo of concentration $c = 10$ and

$R_{decay} = 5$ the cut radius is $R_{cut} \simeq 17$. This density profile yields a finite total mass, that in this example is $M_{cut} \sim 2M_{vir}$. So, only about half of the particles used to simulate this halo in a stable configuration end up inside the virial radius.

The second step is to initialize the particles' positions. These are obtained from the cumulative mass profile, that in the case of the modified NFW lacks an analytical expression. Given $M(r)$, I randomly pick radial distances out of the inverse relation $r(M)$, and in each position I assign a particle of mass $m_{part} = M_{cut}/N_{part}$, where N_{part} is the total number of particles. To obtain a spherically symmetric system, I pick two random angles and split the radius r in the (x, y, z) components. In this way, I obtain a spherically symmetric system of particles, whose mass distribution is the NFW inside the virial radius, and decays exponentially outside.

The third step is to determine the gravitational potential generated by this particle distribution. This is the solution of the Poisson's equation, but numerically it is more straightforward to evaluate the force acting on each particle, as the sum of the contributions by all the others; the complication is that the forces need to be softened at small scales. For this purpose, I define a *softening length*

$$S = \frac{4\ R_{vir}}{N_{vir}} \tag{6.3}$$

following from [141], with N_{vir} being the number of particles inside the virial radius. A correct softening length should be of the order of $< 1\%$ of the virial radius.

There are several prescriptions for the softened potential, and at the beginning I was using the one by Springel ([165],[166]). In the end, I found it more consistent to simply feed my particle distribution to Gadget-2, and have it evaluate the potential directly.

Once the potential is set as a function of the particles' positions, the allowed range of velocities for each particle is determined by the prescription that its binding energy must be positive or null:

$$\epsilon(r) = \Psi(r) - 1/2\ v(r)^2 \geq 0\ ; \tag{6.4}$$

here $\Psi(r) = -\Phi(r)$, with Φ being the gravitational potential. It follows that the escape velocity is defined as $v_{esc}(r) = \sqrt{2\Psi(r)}$ at each radius, where the allowed velocities span

from 0 to v_{esc}. Notice that, under the condition $\epsilon \geq 0$, a physically meaningful constraint on the DF is to set $f = 0$ for unbound particles.

In order to assign a velocity to each particle, I need now to evaluate the single particle's DF. In the case of the isotropic halo, I obtain it from the density profile and the potential through the Eddington's inversion, that I re-write here in a version of more practical use (for halos of any phase-space structure, the generalization of this formula follows from Chapter 5):

$$f(\epsilon) = \frac{1}{\sqrt{8}\pi^2}\left[\int_0^\epsilon \frac{d^2\rho}{d\Psi^2}\,\frac{d\Psi}{\sqrt{\epsilon-\Psi}} + \frac{1}{\sqrt{\epsilon}}\left(\frac{d\rho}{d\Psi}\right)_{\Psi=0}\right] . \tag{6.5}$$

The second term on the r.h.s. is null for any sensible potential [10]. The first term contains the second derivative of the density profile with respect to the potential, and for both the NFW and the modified NFW the relation $\rho(\Psi)$ is not analytical. The attempt to evaluate it numerically, with different methods, failed already for the first derivative, due to the very high noise. At the end, I found that the best alternative is to fit the $\Psi - \rho$ relation and find the second derivative of the fit analytically.

For each particle at a position r, I need the values $f(\epsilon)$ on a grid $0 \leq \epsilon \leq \Psi(r)$, where $\Psi(r)$ is the maximum value of the binding energy for a particle at r; $f(\epsilon)$ is then given by an intregral in the potential from 0 to ϵ. Notice that, at a fixed particle's position, $f(\epsilon) = f(v^2)$, thus the energy DF evaluated at r directly yields the probability density for the particle's total velocity to have a value in the volume d^3v.

It follows that the particle's velocity probability function is obtained as

$$f(v)dv = 4\pi v^2 f(v)dv \ , \tag{6.6}$$

where at each radius the values of v are given by $v = \sqrt{2(\Psi(r) - \epsilon)}$ and span the interval $0 \leq v \leq \sqrt{2\Psi(r)}$. The probability function correctly goes to 0 at the extremes of the allowed velocity range, with a peak that moves towards higher velocities as the particles are closer to the center of the halo.

Notice that this method is computationally expensive, since it involves the evaluation of a set of integrals on a different grid for each particle; instead of doing this, I evaluate $f(\epsilon)$ on a grid of values ϵ equispaced in *log*, that spans the whole range defined by the halo

potential; then for each particle I perform a series of interpolations in f and ϵ to build its velocity DF. The accuracy of the two methods are comparable [87].

Finally, I have everything I need to assign the velocities to the particles. Given the relation $v - f(v)$, I use the acceptance-rejection technique to set $v(r)$ ([143],[95]); it consists in randomly sampling a velocity in the range $0 - v_{esc}(r)$, and a value of f in the range $0 - f_{peak}$, and confronting the point I obtain with the plot $v - f(v)$: if it falls under the curve, the random velocity is taken and assigned to the particle. The single (v_x, v_y, v_z) components of the velocity vector are then assigned in analogy with the coordinates, with two random angles, thus obtaining an isotropic velocity distribution. For different shapes of the velocity dispersion tensor, the components are set through the anisotropy profile parameter $\beta(r)$ (see Chapter 5).

In Figure (6.1) I show the result of a stability test on a simulated modified NFW with isotropic velocity dispersions, made of 10^6 particles. The density profile is recovered from different simulation snapshots, up to 3 dynamical times (*different colors*). The halo looks stable from the very beginning of the simulation, with no oscillations and no deviations from its correct mass distribution. As already discussed here and in the previous Chapters, the stability condition is verified by the use of the Eddington's inversion (or its generalizations). Of course, this does not apply to radii smaller than the softening length, where the N-body approximation fails and numerical artefacts dominate the dynamics. In Figure (6.2) I show the velocity dispersion profiles $\sigma_x, \sigma_y, \sigma_x$ for the same halo (in *different colors*), and confirm that the halo feature the correct isotropy; in addition, I show the velocity dispersions profiles σ_r, σ_t obtained by projecting the total velocity on the radial and tangential directions; notice that there is no directional dependence whatsoever of the velocity distribution profiles. The *green line* represents the theoretical one-dimensional σ obtained from the Jeans' equation for the isotropic modified NFW; notice a bit of noise for small radii, due to the numerical implementation and the randomness of the velocity selection process. As it is immediately apparent, anything at radii smaller than the softening length (*vertical green line*) is out of equilibrium.

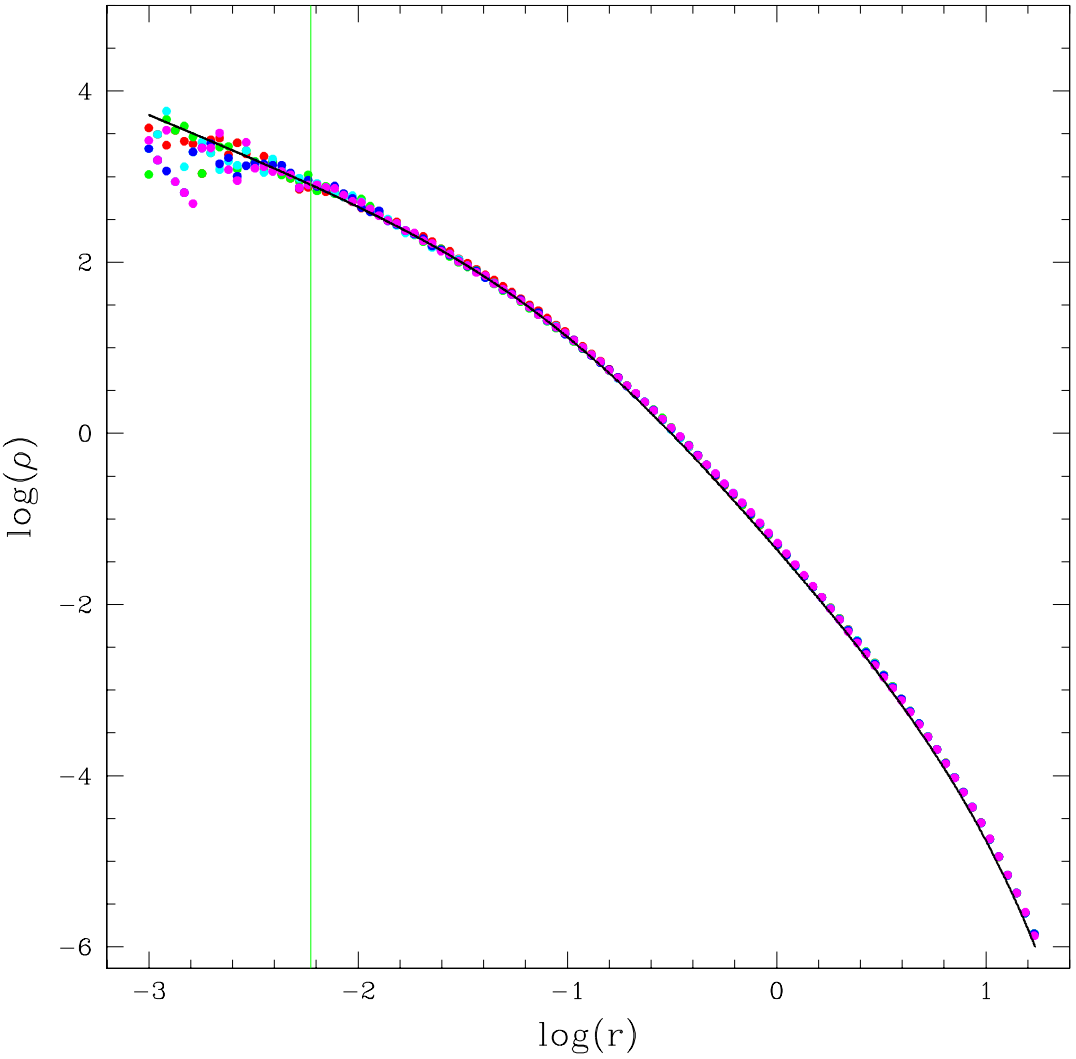

Figure 6.1 Stability test for the initial conditions of a simulated NFW of 10^6 particles: density profile at different snapshots, up to 3 dynamical times (*different colors*). *Solid line*: theoretical modified NFW. *Vertical green line*: softening length limit; inside this radius any result is dominated by numerical artefacts.

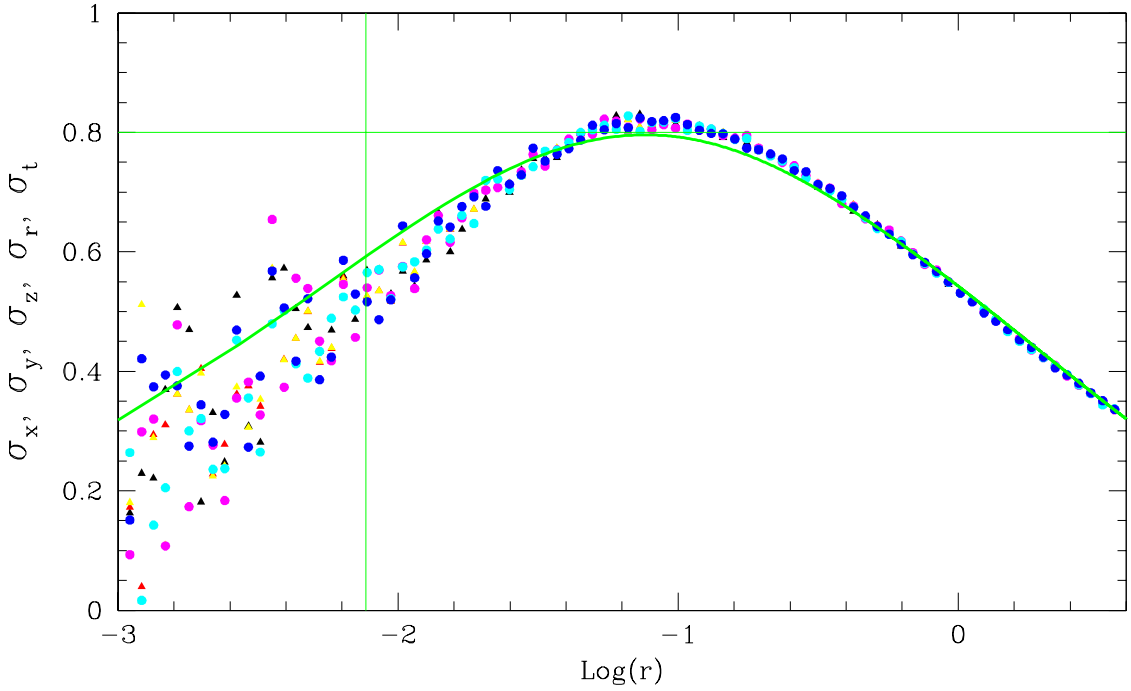

Figure 6.2 The velocity dispersions' profiles for an isotropic 10^6-particle modified NFW (different colors for $\sigma_x, \sigma_y, \sigma_x, \sigma_r, \sigma_t$); the *green line* represent the theoretical solution of the Jeans' equation for the modified NFW density profile. The softening length is marked by the *vertical green line*.

6.3 Work in progress

I intend to start with a suite of simulations specifically studied to model the satellite disruption. To this purpose, I am going to make an ensemble of satellites infall into a parent, trying different equilibium configurations for the halos. In particular, the parent will be a modified NFW, with anisotropy profile as resulting from cosmological simulations. For the satellites, I will try various solutions, for instance (i) the same as the parent, (ii) cored configurations with tangential anisotropy. In addition, I am going to set the satellites' orbits following [8]. In order to test the parent halo response to the substructure infall, I plan to try different subhalos mass functions, as discussed in Chapter 5.

The first issue to consider is the simulation resolution; the inner regions of the satellites must be resolved with an accuracy high enough to appreciate the differences between cores and cusps, and radial and tangential anisotropies. In order to reach this level of precision, I initially plan to use 5×10^5 particles for the biggest substructures. This makes the total number of particles for the parent halo $\sim 5 \times 10^7$ at least.

The tidal stripping of the satellites is going to offset the dynamical friction efficiency in the central regions of the halo; I expect this effect to depend on the orbital parameters, and on both the parent and the satellite structure. Since I cannot evaluate the entity of the offset a-priori, I plan to run a number of tests before the actual simulations.

The main problem is that the dynamical friction efficiency strongly depends on the mass of the satellite as compared to the mass of the background particle; 2-body effects will also depend on the same parameter. If I use dark matter particles of the same mass for the satellite and the halo, the softening length is unique for all particles, and will have to be tuned in order to minimise the spurious gravitational scattering and at the same time maximise the dynamical friction efficiency. Again, a number of preliminary tests are required to settle this question.

Regarding the evolution of the parent halo, there are some interesting side issues that can be investigated. The first is linked to the lack of self-similarity at small scales. In galaxies we do not observe a large number of substructures, while on cluster scales their mass function as predicted by simulations is much more in accord with observations.

This suggests a mass-dependent mechanism of disruption, or alternatively an environment dependency, and I would like to examine this matter further.

The second regards the mass accretion of the parent halo due to substructure infall. As explained in Chapter 1, the phase-space density of NFW halos is described by a power law of critical slope, that maximizes the phase mixing. I am interested in testing this result against different boundary conditions for the mass accretion, including different phase-space structures of the satellites, and with the inclusion of an accurate treatment of dynamical friction, to see whether the same relation still holds, or is replaced by some other functional form, or even whether a universal relation continues to exist.

Chapter 7

Conclusions

In this Thesis I investigated the structure of galactic dark matter halos, encouraged by the lack of a consensus about their mass profile and angular momentum distribution. In fact, while the hierarchical clustering scenario leads naturally to the NFW halo profile, the latter is challenged by observations of the inner structure of galaxies.

My analysis started from the study of the properties of halos in relation to the host galaxies, and the determination of scaling relations between the dark and luminous components, that allowed the construction of an observation-based spin parameter distribution function. During this analysis, it became apparent that the halo mass distribution is not a universal feature deriving from hierarchical clustering, but is instead heavily dependent on the baryonic mass hosted in the halo; I quantified this with an extension of the Universal Rotation Curve to include the whole virialized halo. One interesting feature emerging from this study was that, when compared to the density profile predicted by numerical simulations, the dark matter mass distribution appears not only to be flat in the centre of halos (the core-cusp problem), but also to be overdense around the galactic optical radius, thus not converging to the NFW profile even at these scales.

The overall picture offered by these dynamical evidences suggested me to investigate the interaction between the baryonic component and the dark matter during galaxy formation, and the consequent evolution of the halo. In order to do this, I firstly made a detailed analysis of the phase-space dynamical properties of dark matter halos as collisionless

systems of particles whose structure is governed by the evolution in a gravitational potential. I quantified the connection between the mass density profile and the velocity dispersion tensor, and showed how a perturbation in the velocity structure, triggered by angular momentum injection, causes the cuspy halos predicted by the CDM N-body simulations to evolve into cored configurations. I then proposed a physical mechanism to account for such a halo evolution, that describes the dynamical coupling between the dark and luminous components; dynamical friction of the dark matter on the collapsing baryonic component at the time of protogalaxy formation is powerful enough to alter the halo inner motions and transform the halo profile, thus making it possible to reconcile theory and observations.

In the first part of this Thesis I studied the structure of dark matter halos as inferred from observations of galaxy rotation curves. I built a series of scaling relations that link the mass distribution and geometry of the luminous components in the disk to the dynamical parameters of the host dark matter halo, i.e. mass and angular momentum. The results are at odds with the predictions of numerical simulations. In detail:

• the spin distribution function of galactic halos inferred from observations peaks at significantly lower values than predicted by numerical simulations, indicating a mass accretion history devoid of major mergers since $z \sim 3$;

• the shape and amplitude of the dark matter mass distribution depend strongly and non-linearly on the baryonic mass;

• in single halos, the mass distribution not only is not cuspy in the central regions, but also it does not converge to the NFW even outside the halo core. Rather, it features an excess of mass at the optical radius not attributable to numerical artefacts or exotic DM behaviour.

I conclude that there is no evidence of a universal, self-similar halo hosting spiral galaxies, in contrast with the prediction by hierarchical clustering. The dependence of the halo density profile and angular momentum on the baryonic mass and geometry suggests a dynamical coupling between the dark matter and the baryons, originating at the epoch of galaxy formation.

In order to understand the evolution of dark matter halos under external perturbations, such as the assembly and evolution of the baryonic component, I modeled the dynamical properties of halos in phase-space, and studied the effects of perturbations on their equilibrium structure.

Specifically, I assumed a "pristine" pure dark matter halo to be well described by the NFW, and modeled its evolution during galaxy formation into a cored configuration. The results I obtained can be summarized as follows:

• the phase-space dynamical structure of dark matter halos, including the NFW and the Burkert (cored) halos, is well represented by the same family of solutions of the Jeans equation, *i.e.* a distribution function depending on the binding energy and total random angular momentum of the halo;

• the halo mass distribution is governed by the inner dynamics; the symmetry of the distribution function determines the shape of the velocity dispersion tensor, which in turns determines the density profile. The halo mass distribution is very sensitive to the balance between the tangential and radial motions. In particular, I found the following relation between the anisotropy parameter and the slope of the inner density profile:

$$\rho(r) \propto r^{-2\,(1+2\beta)/(2+\beta)} \;; \tag{7.1}$$

• a perturbation in the anisotropy profile triggers a rearrangement of the halo mass into a new equilibrium configuration; in particular, angular momentum transfer to the halo induces an increase of the tangential motions in the inner halo, leading to the formation of a corelike feature;

• the baryonic collapse inside the halo leading to the formation of the protogalaxy represents a perturbation of the phase-space halo structure that enhances the dark matter tangential motions; the self-bound clouds infalling into the halo potential well are subject to dynamical friction by the background dark matter, and exchange angular momentum locally with the halo, with the result of unbalancing the halo anisotropy profile. The amplitude and distribution of the angular momentum exchanged are compatible with triggering the halo evolution into an equilibrium configuration compatible with the observations.

Galactic dark matter halos, grown from primordial perturbations through hierarchical clustering, and having acquired a characteristic structure through processes like violent relaxation and entropy stratification, are then perturbed by galaxy formation, when a non-negligible amount of baryonic mass and angular momentum are transferred to the center of the halo. The dark matter halo does not behave as a static entity during this process; as the baryonic component is shaped depending on the halo dynamics, conversely the halo reacts to the formation of the galaxy by rearranging its structure and adjusting to the changed equilibrium conditions. The dark and luminous component are dynamically coupled, and jointly evolve into new equilibrium states.

Bibliography

[1] Ahn, K. & Shapiro, P.R. 2005, MNRAS, 363, 1092

[2] An, J.H. & Evans, N.W. 2006, AJ, 131, 782

[3] Athanassoula, E. 2002, ApJ, 569, L83

[4] Baldry, I.K., et al. 2004, ApJ, 600, 681

[5] Bardeen, J.M., Bond, J.R., Kaiser, N., & Szalay, A.S. 1986, ApJ, 304, 15B

[6] Barnes, E.I., Sellwood, J.A., Kosowsky, A. 2004, AJ, 128, 2724

[7] Bell, E.F., McIntosh, D.H., Katz, N., & Weinberg, M.D. 2003, ApJS, 149, 289

[8] Benson, A.J. 2005, MNRAS, 358, 551B

[9] Bertschinger, E. 1985, ApJS, 58, 39

[10] Binney, J. & Tremaine, S., *Galactic dynamics* (1987 Princeton: Princeton University Press)

[11] Blais-Ouellette, S., Amram, P., Carignan, C. 2001, AJ, 1952, 1964

[12] Blais-Ouellette, S., Amram, P., Carignan, C., Swaters, R. 2004, A&A, 420, 147

[13] Blumenthal, G. R., Faber, S. M., Primack, J. R., & Rees, M.J. 1984, Nature, 311, 517

[14] Blumenthal, G. R., Faber, S. M., Flores, R., & Primack, J. R. 1986, ApJ, 301, 27

[15] Boily, C. M., Kroupa, P., & Peñarrubia-Garrido, J. 2001, NA, 6, 27B

[16] Borriello, A., Salucci, P. 2001, MNRAS, 323, 285

[17] Bottema, R. 1999, A&A, 348, 77

[18] Bosma, A. 1981, AJ, 86, 1791

[19] Bosma, A., Byun, Y., Freeman, K. C., Athanassoula, E. 1992, ApJ, 400, L21

[20] Brainerd, T. G. 2004a, preprint (astro-ph/0409381)

[21] Brainerd, T. G. 2004b, AIP Conf. Proc. 743: The New Cosmology: Conference on Strings and Cosmology, 743, 129

[22] Broeils, A.H. 1992a, A&A, 256, 19

[23] Broeils, A.H. 1992b, Ph.D. thesis, Groningen University

[24] Bryan, G.-L., Norman, M.-L. 1998, ApJ, 495, 80

[25] Bullock, J.S., et al. 2001, MNRAS, 321, 559B

[26] Burkert, A. 1995, ApJ, 447, L25

[27] Burkert, A.M. & D'Onghia, E. 2005, in *Penetrating Bars Through Masks of Cosmic Dust*, ed. Block et al. (Dordrecht: Kluwer)

[28] Cardone, V.F., Piedipalumbo, E. & Tortora C. 2005, MNRAS, 358, 1325

[29] Carignan, C., Charbonneau, P., Boulanger, F., Viallefond, F. 1990, A&A, 234, 43

[30] Catinella, B., Giovanelli R., Haynes, M.P., 2006, ApJ. 640, 751

[31] Chiappini, C., Matteucci, F. & Gratton, R. 1997, ApJ, 477, 765

[32] Cole, S. & Lacey, C. 1996, MNRAS, 281, 716

[33] Colin, P., Klypin, A.A. & Kravtsov, A. V. 2000, ApJ, 539, 561

[34] Colless, M. et al. 2003, 2dFGRS data release, astro-ph/0306581

[35] Colpi, M., Mayer, L., & Governato, F. 1999, ApJ, 525, 720

[36] Corbelli, E. & Salucci, P. 2000, MNRAS 311, 411

[37] Courteau S., 1998, AJ, 114, 2402

[38] Courteau, S., et al. 2003, ApJ, 594, 208

[39] Cudderford, P. 1991, MNRAS, 253, 414

[40] Dalcanton, J.J., Spergel, D.N. & Summers, F.J. 1997, ApJ, 482, 659

[41] Dalcanton, J.J. & Hogan, C.J. 2001, ApJ, 561, 35

[42] Dale, D.A., et al. 1999, AJ, 118, 1489

[43] Dame, T.M. 1993, AIPC 278, 267

[44] Davis, M., Efstathiou, G., Frenk, C.S., & White, S.D.M. 1985, ApJ, 292, 371

[45] Debattista, V. P., & Sellwood, J. A. 2000, ApJ, 543, 704

[46] de Blok, W. J. G. & Bosma, A. 2002, A&A, 385, 816

[47] de Blok, W. J. G., Bosma, A. &McGaugh, S. 2003, MNRAS, 340, 657D

[48] de Blok, W. J. G. 2005, ApJ, 634, 227D

[49] Dehnen, W. 1993, MNRAS, 265, 250

[50] Dehnen, W. 2005, MNRAS, 360, 892D

[51] Dekel, A. & Birnboim, Y. 2006, MNRAS, 368, 2

[52] Donato, F., Gentile, G. &Salucci, P. 2004, MNRAS, 353, 17

[53] D'Onghia, E. & Burkert, A.M. 2004, ApJ, 612, L13

[54] D'Onghia, E. & Lake, G. 2004, ApJ, 612, 628

[55] D'Onghia, E., Maccio', A., Lake, G., Stadel, J. & Moore, B. 2007, astro-ph/0704.2604v1

[56] Dominguez-Tenreiro, R., Oñorbe, J., Saiz, A., Artal, H. & Serna, A. 2006, ApJL, 636L, 77

[57] Donato, F., Gentile, G. & Salucci, P. 2004, MNRAS, 353, L17

[58] Dutton, A. A., van den Bosch, F. C., Dekel, A. & Courteau, S. 2006, ApJ, 654, 27

[59] Eke, V.R., Cole, S., & Frenk, C.S., 1996, MNRAS 282,263

[60] El-Zant, A., Shlosman, I. & Hoffman, Y. 2001, ApJ, 560, 636

[61] El-Zant, A., Hoffman, Y., Primack, J., Combes, F. & Shlosman, I. 2004, ApJ, 607, L75

[62] Evans, N. W. 1993, MNRAS, 260, 191

[63] Evans, N.W. & An, J.H. 2005, A&A, 444, 45

[64] Evans, N. W. & Collett, J. L. 1997, ApJL, 480, L103

[65] Fall, S.M. & Efstathiou, G. 1980, MNRAS 193, 189

[66] Font, A. S., Navarro, J. F., Stadel, J., & Quinn, T. 2001, ApJ, 563, L1

[67] Freeman, K. C. 1970, ApJ, 160, 811F

[68] Fukugita, M., Shimasaku, K., & Ichikawa, T. 1995, PASP, 107, 945

[69] Fukushige, T. & Makino, J. 1997, ApJL, 477, L9

[70] Fukushige, T. & Makino, J. 2001, ApJ, 557, 533

[71] Gardner, J.P. 2001, ApJ, 557, 616

[72] Gentile G., Salucci P., Klein U., Vergani D., Kalberla P., 2004, MNRAS, 351, 903

[73] Gentile, G., Burkert, A., Salucci, P., Klein, U., Walter, F. 2005, ApJ, 634, L145

[74] Gentile G., Salucci P., Klein U., Granato G.L., 2007, MNRAS, 375, 199

[75] Gentile G., Tonini, C. & Salucci P. 2007, A&A, 467, 925

[76] Gerhard, O., Kronawitter, A., Saglia, R. P., & Bender, R. 2001, AJ, 121, 1936

[77] Ghigna, S., Moore, B., Governato, F., Lake, G., Quinn, T. & Stadel, J. 2000, ApJ, 544, 616

[78] Giovanelli, R., et al. 1997, ApJ, 477, L1

[79] Gnedin, O. Y., Kravtsov, A. V., Klypin, A. A., & Nagai, D. 2004, ApJ, 616, 16

[80] Hayashi, E., Navarro, J. F., Taylor, J. E., Stadel, J., & Quinn, T. 2003, ApJ, 584, 541

[81] Hayashi, E., Navarro, J. F. 2006, MNRAS, 373, 1117

[82] Hernquist, L. 1990, ApJ, 356, 359

[83] Hernquist, L. 1993, ApJS, 86, 389

[84] Huss, A., Jain, B. & Steinmetz, M. 1999, ApJ, 517, 64

[85] Jaffe, W. 1983, MNRAS, 202, 995

[86] Jing, Y. P. & Suto, Y. 2000, ApJL, 529, L69

[87] Kazantzidis, S., Magorrian, J. & Moore, B. 2004, ApJ, 601, 37

[88] Kent, S.M. & Gunn, J.E. 1982, AJ, 87, 945

[89] King, I. R. 1966, AJ, 71, 64

[90] Kleinheinrich M., et al., 2006, A&A, 455,441

[91] Kleyna, J.T., Wilkinson, M.I., Evans, N.W. & Gilmore, G. 2005, ApJL, 630, L141

[92] Klypin, A.A., Kravtsov, A.V., Valenzuela, O. & Prada, F. 1999, ApJ, 522, 82

[93] Koopmans, L.V.E., Treu, T., Bolton, A.S., Burles, S. & Moustakas, L.A. 2006, ApJ, 649, 599

[94] Kravtsov A.V., Klypin A.A., Bullock J.S. & Primack J.R.,1998, ApJ, 502, 48

[95] Kuijken, K., & Dubinski, J. 1994, MNRAS, 269, 13

[96] Lacey, C. & Cole, S. 1993, MNRAS, 262, 627

[97] Łokas, E. L. & Hoffman, Y. 2000, ApJL, 542, L139

[98] Łokas, E.L. & Mamon, G.A. 2001, MNRAS, 321, 155

[99] Louis, P.D. 1993, MNRAS, 261, 283

[100] Lynden-Bell, D. 1967, MNRAS, 136, 101

[101] Ma C.-P. & Boylan-Kolchin M. 2004, PhRvL 93b 1301M

[102] Mather, J.C. et al. 1991, Adv.Sp.Res., 11, 193

[103] Mayer, L., Moore, B., Quinn, T., Governato, F., & Stadel, J. 2002, MNRAS, 336, 119

[104] McGaugh, S. S., de Blok, W. J. G., Schombert, J. M., Kuzio de Naray, R., & Kim, J. H. 2006, ApJ, 659, 149M

[105] Merritt, D. 1985, AJ, 90, 6

[106] Mihos, J. C., McGaugh, S. S., & de Blok, W. J. G. 1997, ApJ, 477, L79

[107] Mo, H.J., Mao, S. & White, S.D.M. 1998, MNRAS 295, 319

[108] Mo, H.J. & Mao, S. 2004, MNRAS, 353, 829

[109] Moore, B., Katz, N., & Lake, G. 1996, ApJ, 457, 455

[110] Moore B., Governato F., Quinn T., Stadel J. & Lake G., 1998, ApJ, 499, L5

[111] Moore, B. et al. 1999, ApJL, 524, L19

[112] Navarro, J.F., Eke, V.R. & Frenk, C.S. 1996, MNRAS, 283, L72

[113] Navarro, J.F., Frenk, C.S., & White, S.D.M. 1996, ApJ, 462, 563

[114] Navarro, J.F., Frenk, C.S. & White, S.D.M. 1997, ApJ, 490, 493

[115] Navarro, J.F. & Steinmetz, M. 2000, ApJ 538, 477

[116] Nipoti, C., Treu, T., Ciotti, L. & Stiavelli, M. 2004, MNRAS 355, 1119-1124

[117] Noordermeer, E., van der Hulst, T., Swaters, R. 2004, Proceedings of "Baryons in Dark Matter Halos". Novigrad, Croatia, 5-9 Oct 2004. Eds: R. Dettmar, U. Klein, P. Salucci. Published by SISSA, Proceedings of Science, http://pos.sissa.it, p. 68.

[118] Noordermeer, E. et al. 2007, MNRAS, 376, 1513N

[119] Nusser, A. & Sheth, R. K. 1999, MNRAS, 303, 685

[120] Osipkov, L.P. 1979, Soviet Astron. Lett., 5, 42

[121] Padmanabhan, T., *Theoretical astrophysics* (2002, Cambridge University Press)

[122] Peacock, J.A. *Cosmological physics* (1999, Edinburgh university press)

[123] Peebles, P.J.E. & Dicke, R. 1968, ApJ, 154, 891

[124] Peebles, P.J.E. 1969, ApJ, 155, 393

[125] Peebles, P.J.E. 1970, AJ, 75, 13

[126] Peebles, P.J.E. 1973, PASJ, 25, 291

[127] Peebles, P.J.E. 1974, ApJ, 189, L51

[128] Peebles, P.J.E. 1978, A&A, 68, 345

[129] Peebles, P.J.E. *Physical cosmology* (1980 Princeton university press)

[130] Peebles, P.J.E. 1982, ApJL, 263, L1

[131] Peirani, S., Mohayaee, R., & de Freitas Pacheco, J.A. 2004, MNRAS, 348, 921

[132] Peñarrubia, J., Just, A. & Kroupa, P. 2004, MNRAS, 349, 747

[133] Persic, M., Salucci, P. 1988, MNRAS, 234, 131 (PS88)

[134] Persic M., Salucci P., 1990, MNRAS, 245, 577

[135] Persic, M., Salucci, P. 1990, MNRAS, 247, 349

[136] Persic, M., Salucci, P. 1991, ApJ, 368, 60 (PS91)

[137] Persic, M., Salucci, P. 1995, ApJS, 99, 501 (PS95)

[138] Persic, M., Salucci, P., Stel, F. 1996, MNRAS, 281, 27

[139] Persic, M. & Salucci, P. 1999, MNRAS 309, 923

[140] Plummer, H. C. 1911, MNRAS, 71, 460

[141] Power, C. et al. 2003, MNRAS, 338, 14

[142] Prada, F.,Vitvitska, M., Klypin, A., Holtzman, J. A., Schlegel, D. J., Grebel, E. K., Rix, H.-W., Brinkmann, J., McKay, T. A., Csabai, I. 2003, ApJ, 598, 260

[143] Press, W. H., Teukolsky, S. A., Vetterling, W. T., & Flannery, B. P., 1996, Numerical Recipes in Fortran 90 (2d ed.; Cambridge: Cambridge Univ. Press)

[144] Quinn, P. J., & Goodman, J. 1986, ApJ, 309, 472

[145] Rhee, M-H 1996, PhD Thesis, Groningen University.

[146] Roscoe, D. F. 1999, A&A **343**, 788

[147] Rubin, V.C., Ford, W.K., Jr., Thonnard, N. 1980, ApJ, 238, 471

[148] Rubin, V.C., Ford, W.K., Jr., Thonnard, N., Burstein, D., 1982, ApJ, 261, 439

[149] Rubin V. C., Burstein D., Ford W.K., Jr., Thonnard N., 1985, ApJ, 289, 81

[150] Salucci P., Persic M., 1997, ASPC, 117, 1

[151] Salucci P., Persic M., 1999, MNRAS, 309, 923

[152] Salucci,P., Burkert, A. 2000, ApJ, 537, L9

[153] Salucci, P., Walter, F., Borriello, A. 2003, A&A, 409, 53

[154] Salucci, P., Lapi, A., Tonini, C., Gentile, G., Yegorova, I. & Klein, U. 2007, MNRAS, 378, 41

[155] Sellwood, J. A., McGaugh, S. S. 2005, ApJ, 634, 70

[156] Seigar, M. S., Bullock, J. S., Barth, A. J., & Ho, L. C. 2006, ApJ, 645, 1012

[157] Shankar, F., Lapi, A., Salucci, P., De Zotti, G. & Danese, L. 2006, ApJ, 643, 14

[158] Simard, L., et al. 1999, ApJ, 519, 563

[159] Simon, J. D., Bolatto, A. D., Leroy, A., Blitz, L., Gates, E. L. 2005, ApJ, 621, 757

[160] Sofue, Y., Tutui, Y., Honma, M., Tomita, A., Takamiya, T., Koda, J., Takeda, Y. 1999, ApJ, 523, 136

[161] Spergel, D.N. & Steinhardt, P.J. 2000, PhRvL, 84, 3760

[162] Spergel, D.N. et al. 2003, ApJS, 148, 175

[163] Spergel, D.N. et al. 2007, ApJS, 170, 377S

[164] Springel, V., & White, S. D. M. 1999, MNRAS, 307, 162

[165] Springel V., Yoshida N., White S. D. M., 2001, NA, 6, 51

[166] Springel V. 2005, MNRAS, 364, 1105

[167] Stoehr F., PhD thesis, 2003, Ludwig Maximilian Univ. Mnchen

[168] Syer, D. & White, S. D. M. 1998, MNRAS, 293, 337

[169] Swaters, 1999, Ph.D. Thesis, Groningen University

[170] Swaters, R.A., Madore, B.F., van den Bosch, F.C., Balcells, M. 2003, ApJ, 583, 732

[171] Taffoni, G., Mayer, L., Colpi, M., & Governato, F. 2003, MNRAS, 341, 434

[172] Taylor, J. E., & Babul, A. 2001, ApJ, 559, 716

[173] Taylor, J. E. & Navarro, J. F. 2001, ApJ, 563, 483T

[174] Thomas, P.A. et al. 1998, MNRAS, 296, 1061

[175] Tonini, C. & Salucci, P. 2004, in *Baryons in Dark Matter Halos*, ed. R. Dettmar et al. (http://pos.sissa.it), 89

[176] Tonini, C., Lapi, A., Shankar, F. & Salucci, P. 2006, ApJL, 638, L13

[177] Tonini, C., Lapi, A., Salucci, P. 2006, ApJ, 649, 591

[178] Valenzuela, O., & Klypin, A. 2003, MNRAS, 345, 406

[179] Valenzuela, O., Rhee, G., Klypin, A., Governato, F., Stinson, G., Quinn, T., Wadsley, J. 2007, ApJ, 657, 773V

[180] van den Bosch, F.C., Lewis, G.F., Lake, G. & Stadel, J. 1999, ApJ, 515, 50

[181] van den Bosch, F.C., Swaters, R.A., 2001 MNRAS, 325, 1017

[182] van den Bosch, F., Burkert, A., & Swaters, R.A. 2001, MNRAS, 326, 1205

[183] van den Bosch, F.C., et al. 2002, ApJ, 576, 21

[184] van den Bosch, F.C., Tormen, G. & Giocoli, C. 2005, MNRAS, 359, 1029

[185] van Zee, L., Bryant, J. 1999, AJ, 118, 2172

[186] Velázquez, H., & White, S. D. M. 1995, MNRAS, 275, 23L

[187] Velázquez, H., & White, S. D. M. 1999, MNRAS, 304, 254

[188] Verheijen, M. 1997, Ph.D. Thesis, Groningen University

[189] Verheijen, M. A. W., Sancisi, R. 2001, A&A, 370, 765

[190] Verheijen, M. 2004, Astronomische Nachrichten, Volume 325, Number 2, pp.151-154

[191] Vikhlinin, A., Kravtsov, A., Forman, W., et al. 2006, ApJ, 640, 691

[192] Vitvitska, M., et al. 2002, ApJ, 581, 799

[193] Walsh, W., Staveley-Smith, L., Oosterloo, T. 1997, AJ, 113, 1591

[194] Wechsler,R.H., Bullock, J.S., Primack, J.R., Kravtsov, A.V., Dekel, A. 2002, ApJ, 568, 52

[195] Weiner, Benjamin J., Williams, T. B., van Gorkom, J. H., Sellwood, J. A. 2001, ApJ, 546, 916

[196] Weldrake, D.T.F., de Blok, W. J. G., Walter, F. 2003, MNRAS, 340, 12

[197] White, S.D.M. & Frenk, C.S. 1991, ApJ, 379, 52

[198] White, S.D.M. 1996, grdy, conf, 121W

[199] White, S.D.M. 1997, evun, work, 227W

[200] White, S.D.M. 1997, gsr, proc, 3W

[201] White, S.D.M. & Rees, M.J. 1978, MNRAS, 183, 341

[202] Widrow, L.M. 2000, ApJSS, 131, 39

[203] Willick J.A., 1999, ApJ, 516, 47

[204] Willman, B. et al. 2005, ApJ, 626, L85

[205] Wong, T., Blitz, L., Bosma, A. 2004, ApJ, 605, 183

[206] Yegorova, I. et al, 2007, MNRAS, 377, 507

[207] Zappacosta, L., Buote, D. A., Gastaldello, F., et al. 2006, ApJ, 650, 777

[208] Zwicky, F. 1933, AcHPh, 6, 110Z

[209] Zwicky, F. 1937, ApJ, 86, 217Z

Appendix A

The resolution of mass modelling from rotation curves

In this Appendix I present a method for the mass modelling from rotation curves (RCs) of spirals that, provided the curves are of high quality, ensures a unique decomposition of the luminous and dark matter components, for a general halo profile.

Consider a two-components system, made of an exponential disk of scale-length R_D embedded into a dark matter halo, of mass distribution taken as the pseudo-isothermal sphere (PI). The reason for this choice is the following: the PI model has two free parameters determining the mass distribution, a fact that increases the degeneracy of the mass modelling with respect to one-parameter profiles, like the NFW or the URC. For this reason, the conclusions in this Appendix safely apply to the NFW and the URC as well, less problematic from this point of view.

The total rotation curve is given by

$$V^2(r) = V_d^2(r) + V_h^2(r) \ , \tag{A.1}$$

where r is the radial distance normalised to R_D; in these units, the disk component is $V_D^2(r) = GM_D/R_D \ \nu(r)$, with $\nu(r)r/2 \ (I_0K_0 - I_1K_1)|_{r/2}$ [67] and the halo one is $V_H^2(r) = GM_H/(r \ R_D)$.

In the most general case, the contribution of the luminous matter to the total rotational velocity is determined by two parameters: the disk scale-length R_D and the total

disk mass M_D. The dark component is determined by other two parameters, usually taken as the central halo density ρ_0 and the halo characteristic scale length R_C.

A.1 The mass modelling for PI halos

The DM density profile of the PI sphere is given by

$$\rho(r) = \frac{\rho_0}{1 + (r/R_C)^2} \ ; \tag{A.2}$$

for convenience I define $r \equiv r/R_D$ and $R_C \equiv R_C/R_D$. The mass profile of the halo is

$$M_H(r) = 4\pi G\rho_0 \ R_C^3 R_D^3 \left[\frac{r}{R_C} - tan^{-1}\left(\frac{r}{R_C}\right)\right] \ ; \tag{A.3}$$

after setting

$$\lambda(r) \equiv \frac{R_C^3}{r} \ \left[\frac{r}{R_C} - tan^{-1}\left(\frac{r}{R_C}\right)\right] \ , \tag{A.4}$$

the total velocity is written as

$$V^2(r) = V_D^2(r) + \frac{G4\pi\rho_0 \ R_D^3}{R_D} \ \lambda(r) \ . \tag{A.5}$$

Now consider the following transformation:

$$\alpha \equiv \frac{GM_D}{R_D \ V_1^2}, \qquad \beta \equiv \frac{4\pi G\rho_0 \ R_D^3}{R_D \ V_1^2}, \qquad \lambda_1 \equiv R_C^3 \ \left[\frac{1}{R_C} - tan^{-1}\left(\frac{1}{R_C}\right)\right]$$

where $V_1^2 \equiv V^2(r = 1))$, and the parameters α and β are directly proportional to the fraction of the luminous and dark mass respectively, evaluated at R_D. The normalized rotation curve is then

$$\frac{V^2(r)}{V_1^2} = \alpha \ \nu(r) + \beta \ \lambda(r) \ ; \tag{A.6}$$

α, β and λ determine the shape of the curve, while V_1^2 determines its amplitude, as a normalisation parameter. Notice that

$$\alpha \ \nu_1 + \beta \ \lambda_1 = 1 \ , \tag{A.7}$$

where $\nu_1 = \nu(r = 1)$; the quantities $\alpha\nu_1$ and $\beta\lambda_1$ represent the fractional contributions to the total velocity at R_D due to the luminous and dark matter respectively; I define $f_{DM} \equiv \beta\lambda_1$.

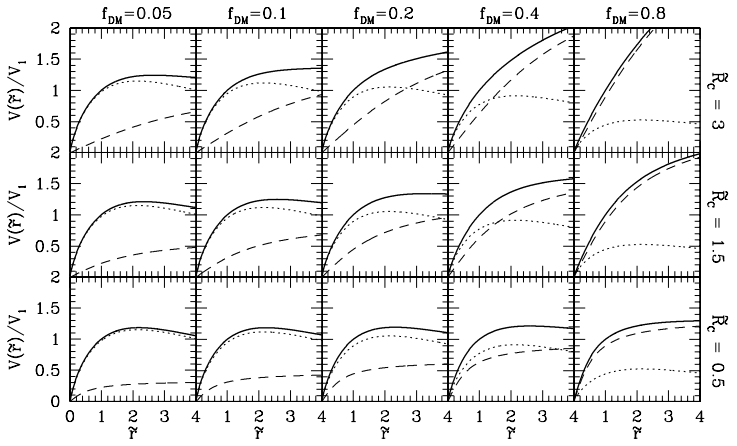

Figure A.1 PI rotation curves, for different f_{DM} and R_C. *Solid lines*: total rotational velocity; *dashed lines*: dark matter component; *dotted lines*: baryonic component.

Finally, the rotation curve can be written as

$$\frac{V^2(r)}{V_1^2} = (1 - f_{DM})\ \frac{\nu(r)}{\nu_1} + f_{DM}\ \frac{\lambda(r)}{\lambda_1}\ , \tag{A.8}$$

with the transformed free parameters governing the shape of the curve defined in the ranges

$$0 \leq f_{DM} \leq 1 \qquad 0 \leq R_C \leq 3\ .$$

The range for R_C is conservative; high-quality rotation curves described in Chapter 3 and 4 reach out to several disk scale-lengths. The last parameter V_1 is a normalisation that can be neglected in the present argument, since it does not affect the precision of the curve determination.

In Fig. (A.1) I show some examples of rotation curves obtained for different values of the parameters, to illustrate the visual degeneracy of the problem. Apparently, very simular curves can be obtained with different combinations of the parameters (*dashed lines* represent the halo component, *dotted lines* the baryonic one), when the curves are smooth like in the majority of the observations. In Fig. (A.2) I show some easy examples instead, of curves where the baryonic component produces a visible feature in the velocity profile, thus facilitating the mass-modelling process.

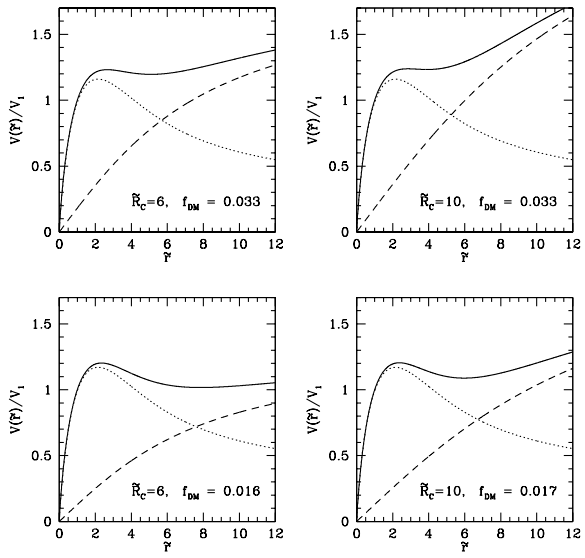

Figure A.2 PI rotation curves with a second-order anomaly, indicating a sharp transition between a disk-dominated to a halo dominated region.

A.2 Disentangling a high-quality RC

From a smooth, featureless rotation curve, it is possible to obtain the correct mass modelling and uniquely disentangle the luminous and dark components of the mass distribution, provided that the quality of the curve is acceptable, that is, that the observational errors at each point of the curve are not too large.

Here I illustrate a virtual experiment: I simulate the obervation of a number of reference curves, and apply the mass modelling described above to recover the parameters characterising the luminous and dark components.

In detail, consider 25 reference curves, each one consisting of 25 data points between $0 \leq r \leq 4$ in units of R_D; the error in the value of the velocity is on average $\epsilon_V = 0.02$ and that in the slope of the curve is $\epsilon_D = 0.05$ ([137]; these errors are of the order of those in high-quality RCs measured today). The parameter space is defined as $f_{DM} = \{0.1, 0.3, 0.5, 0.7, 0.9\} \otimes R_C = \{0.1, 1.0, 2.0, 3.0, 4.0\}$. A semplification coming from the observational technique is that V_1 can be set direclty from the data:

$$V_1 \equiv V(1) \pm \mathcal{O}(10^{-2}) \ , \tag{A.9}$$

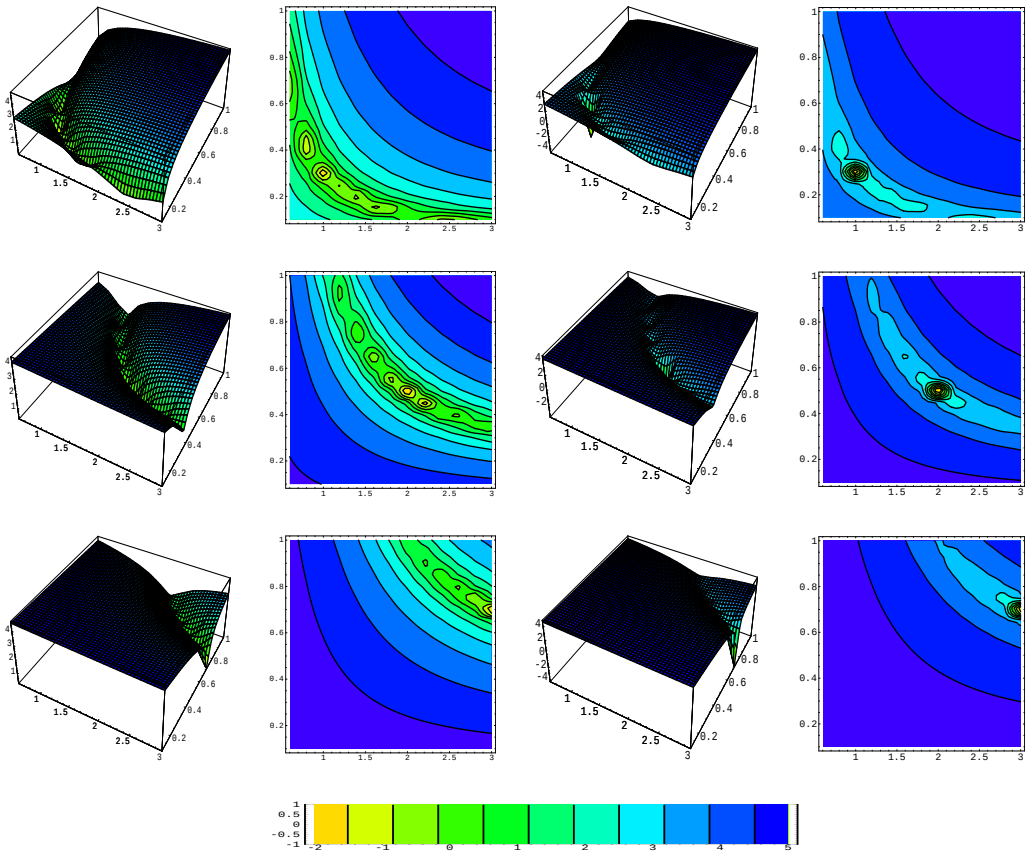

Figure A.3 $\chi^2(V)$ (*left*) compared to χ^2_{TOT} (*right*) for 3 reference curves, as a function of the model parameters: $R_C \in [0.2, 4]$ (*x-axis*) and $f_{DM} \in [0.05, 1]$ (*y-axis*). The "true" parameters are: $(R_C = 1.0, f_{DM} = 0.3)$ *top panels*, $(R_C = 2, f_{DM} = 0.5)$ *middle panels*, $(R_C = 3, f_{DM} = 0.7)$ *bottom panels*. The colour scale is in $log(\chi^2)$.

if and only if the curve is accurate enough. Actually, I would define a high-quality RC as a curve allowing for this measurement.

The distance in parameter space between a model curve V_{mod} (reconstructued thorugh mass modelling) and a reference curve V_{obs} can be defined by a likelihood-type parameter, taken as the sum of the χ^2 computed on the velocity and on the RC slope:

$$\chi^2_{TOT} = \chi^2_V + \chi^2_D \ . \tag{A.10}$$

The two contributions are given by:

$$\chi^2_V([f_{DM}, R_C]_{mod}) = \frac{1}{\epsilon^2_V} \sum_{n=1}^{25} \left(V_{mod}(r_n; [f_{DM}, R_C)]_{mod}) - V_{obs}(\tilde{r}_n)\right)^2 \ , \tag{A.11}$$

$$\chi^2_D([f_{DM}, R_C]_{mod}) = \frac{1}{\epsilon^2_D} \sum_{n=1}^{25} \left(\frac{r_n}{V_{mod}} \frac{dV_{mod}(r_n; [f_{DM}, R_C)]_{mod})}{dr} - \frac{r_n}{V_{obs}} \frac{dV_{obs}(r_n)}{dr} \right)^2 . \tag{A.12}$$

The novelty of the approach is in considering the slope of the curve as an aid in minimising the smallest volume in parameter space that is resolved by the mass modelling. In Fig. (A.3) I illustrate the difference in the mass-modelling resolution, if the χ^2_V is considered alone (*left panels*), and if the χ^2_{TOT} is considered instead (*right panels*). It is clear that in the second case the resolution increases dramatically. In fact, the χ^2_{TOT} rises sharply to a value of $\sim 10^2$ in an interval of $\Delta f_{DM} \sim 0.05$ and of $\Delta R_C < 0.25$; these values set the resolution scale of the mass modelling.

Fig. (A.4) illustrate te behaviour of χ^2_{TOT}, for an ensemble of 400 model curves used to fit the 25 reference curves: each of the 10.000 points in the plot represents the χ^2_{TOT} for a couple $V_{obs} - V_{mod}$, mapped as a function of their actual distance in parameter space, defines as

$$D \equiv (\Delta^2(R_C/4) + \Delta^2(f_{DM}))^{1/2} \ , \tag{A.13}$$

with $\Delta(x) = x_{mod} - x_{obs}$; since the range of variation of R_C is four times that of f_{DM}, the former is normalised by a factor 4 to make the two contributions to D comparable. The result is shown in the *upper panel*; the *red circles* represent cases in which the distance is dominated by variations of the core radius ($\Delta^2(R_C/4) > \Delta^2(f_{DM})$), the *blue triangles* are cases in which the distance is mainly due a different amplitude of the dark matter contribution. The straight lines represent the values of χ^2_{TOT} corresponding to the 3σ and 1σ limits, thus selecting out the couples $V_{obs} - V_{mod}$ unresolved by the model. Notice that most of the points lay over the 3σ limit, showing that the model can uniquely resolve the mass distribution parameters.

In addition, the vertical line defines a distance in the parameter space of $D = 0.25$; couples lying in this range are characterised by parameters so similar that the offset between them is quite negligible for the purpose of determining the mass distribution of

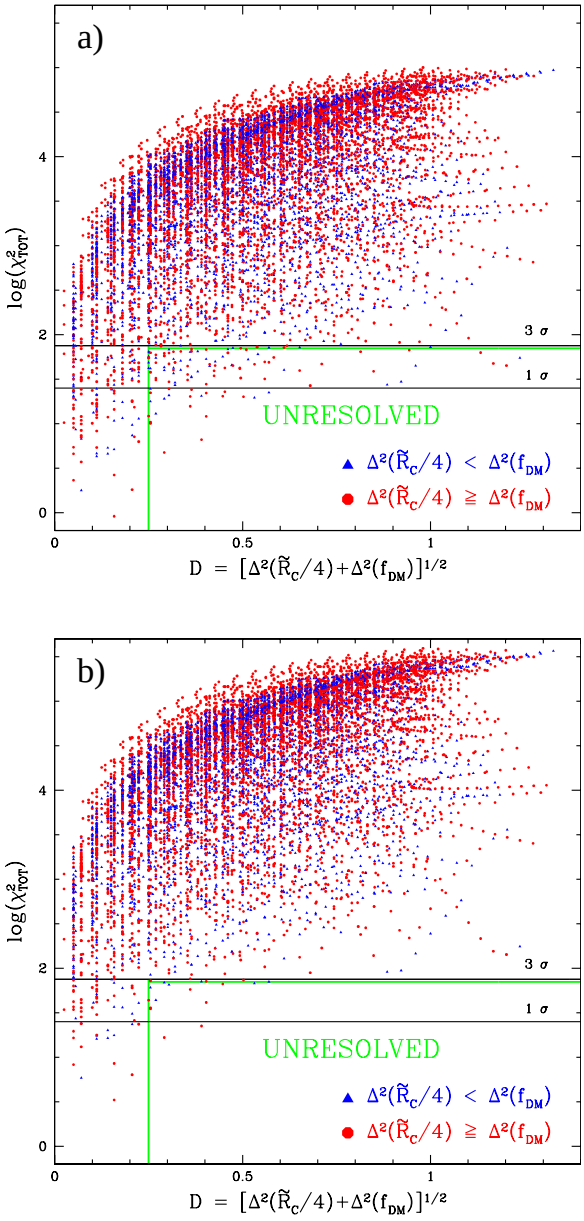

Figure A.4 χ^2_{TOT} of the 25 reference "observed" curves mapped with 400 model curves, as a function of the distance in the parameter space. Red points (circles) are for distances dominated by the variation of $\tilde{R}_C$, blue points (triangles) are for distances dominated by the variation of f_{DM}. The straight lines represent the 1σ and 3σ limits. Panel *a)* $\epsilon_V = 0.02$ and $\epsilon_D = 0.05$. Panel *b)* $\epsilon = 0.01$ and $\epsilon_D = 0.03$.

the components. Hence, the points in the range $D \leq 0.25$ and laying below the 3σ limit are not to be considered as system's failures. Summing up, the mass modelling described above is successfull in the $\sim 99\%$ of cases, while about $\sim 1\%$ of the couples $V_{obs} - V_{mod}$ are unresolved.

The observational errors adopted are typical of about the top 50% of the observed RCs available today. There are cases however, where the errors on the RC are even smaller; if one considers errors of $\epsilon_V = 0.01$ and $\epsilon_D = 0.03$ (curves with these errors are available today, in increasing number), the same analysis leads to the *bottom panel* of Fig. (A.4). In this case, about 0.17% of the couples are unresolved; if the lower limit of the resolution was set by the worst performance, the uncertainty in the mass modelling would still be reasonable: $(\Delta(f_{DM}))_{MAX} = 0.25$ and $(\Delta R_C)_{MAX} = 1.2R_D$. However, considering the negligible amount of failures however, I can safely state that the average resolution of this mass-modelling procedure is set by the density of points in the parameter space, *i.e.* $(\Delta(f_{DM})) = 0.05$ and $(\Delta R_C) = 0.2R_D$.